Analytical and Computational Modeling of Mechanical Waves in Microscale Granular Crystals: Nonlinearity and Rotational Dynamics

Samuel P. Wallen

A dissertation
submitted in partial fulfillment of the
requirements for the degree of

Doctor of Philosophy

University of Washington

2017

Supervisory Committee:

Nicholas Boechler, Chair

Bernard Deconinck, GSR

Ashley Emery, Reading Committee Member

I. Y. (Steve) Shen

Duane Storti, Reading Committee Member

Program Authorized to Offer Degree:
Mechanical Engineering

©Copyright 2017
Samuel P. Wallen

University of Washington

Abstract

Analytical and Computational Modeling of Mechanical Waves in Microscale Granular Crystals: Nonlinearity and Rotational Dynamics

Samuel P. Wallen

Chair of the Supervisory Committee:
Assistant Professor Nicholas Boechler
Mechanical Engineering

Granular media are one of the most common, yet least understood forms of matter on earth. The difficulties in understanding the physics of granular media stem from the fact that they are typically heterogeneous and highly disordered, and the grains interact via nonlinear contact forces. Historically, one approach to reducing these complexities and gaining new insight has been the study of granular crystals, which are ordered arrays of similarly-shaped particles (typically spheres) in Hertzian contact. Using this setting, past works explored the rich nonlinear dynamics stemming from contact forces, and proposed avenues where such granular crystals could form designer, dynamically responsive materials, which yield beneficial functionality in dynamic regimes. In recent years, the combination of self-assembly fabrication methods and laser ultrasonic experimental characterization have enabled the study of granular crystals at microscale. While our intuition may suggest that these microscale granular crystals are simply scaled-down versions of their macroscale counterparts, in fact, the relevant physics change drastically; for example, short-range adhesive forces between particles, which are negligible at macroscale, are several orders of magnitude stronger than gravity at microscale. In this thesis, we present recent advances in analytical and computational modeling of microscale granular crystals, in particular concerning the interplay of nonlinearity, shear interactions, and particle rotations, which have previously been either absent, or included separately at macroscale. Drawing inspiration from past works on phononic crystals and nonlinear lattices, we explore problems involving locally-resonant metamaterials, nonlinear localized modes, amplitude-dependent energy partition, and other rich dynamical phenomena. This work enhances our understanding of microscale granular media, which may find applicability in fields such as ultrasonic wave tailoring, signal processing, shock and vibration mitigation, and powder processing.

TABLE OF CONTENTS

LIST OF FIGURES

DEDICATION

To my family and friends

ACKNOWLEDGMENTS

I would like to thank and acknowledge my advisor, Nicholas Boechler. Over the last four years, you have taught me so much about the research process and the scientific method, and given me the opportunity to shape my own PhD research. I am truly greatful to have worked with an advisor who gave me freedom and listened to my inputs in both research and teaching, but pushed me when I needed it.

I would also like to acknowledge the other members of my supervisory committee: Steve Shen, Ashley Emery, Bernard Deconinck, and Duane Storti. Professor Shen, you taught my first mechanical engineering course when I was a sophomore undergrad, and I knew I had chosen the right major! I cannot thank you enough for your mentorship in classes and research.

To Mom, Dad, and the rest of the family, thank you so much for your unwavering love and support throughout this journey. I could not have done this without you. To my grandparents, your life stories have been a continuous source of inspiration and strength, and I would not be where I am today if not for the amazing families you built.

I would like to send a big hug, high-five, and fist-bump to all my friends who have helped me have fun! To Joel, Ryan, and Tony, thank you for making my undergrad experience great, and for sticking with me as our lives have taken off (Go Huskies!). To Will, Brian, and Matt, I cannot express enough gratitude for sharing an awesomely ridicululous apartment, and keeping me sane in the most stressful of times.

Last but not least, I thank my labmates and the other students who have walked along side me through my graduate studies. To Amey Khanolkar, Morgan Hiraiwa, Maroun Abi Ghanem, Ariana Mendible, and all the undergrads who have worked in our lab, it has been a pleasure working and growing with you. Stay awesome!

Chapter 1

INTRODUCTION

1.1 Motivation

Granular media are one of the most common forms of matter on earth, and can be found naturally in the forms of sand, soil, and snow, as well as in man-made applications, such as foods, pigments, and explosives. Yet, despite the abundance of granular media in the world around us, we still lack a satisfactory understanding of the physics that govern their properties. For example, while it has been long known that a sand bag can stop a bullet, it can also easily be penetrated by a slowly-moving pencil; this seemingly simple example illustrates a complex, rate-dependent energy dissipation phenomenon, and is still an area of active study.

The difficulties in modeling granular media stem from the fact that they are typically highly disordered and heterogeneous, with particles interacting via highly nonlinear contact forces [1, 2]. These particles may be of uniform or varying size and shape ("mono-" and "poly-" disperse, respectively). In addition, the particles can interact via normal and tangential forces, translate and rotate in three dimensions, and undergo their own deformations. Furthermore, the relevant physics change when considering different length scales; for example, while gravity plays a significant role at macroscale (particle lengths on the order of millimeters or larger), adhesion is dominant at microscale (by several orders of magnitude, in fact) [3]. By considering these variables alone, one can get a feeling for the vastness of the parameter space accessible in the study of granular media, and conclude that there are many open problems yet to be solved.

One of the ways in which this complexity has been addressed is to study ordered systems

[4]. These ordered systems, often referred to as granular crystals, have proven interesting because they offer a simplified context from which to draw conclusions, and also form a type of phononic crystal or metamaterial, which can be used to manipulate and control mechanical waves [5]. Furthermore, they provide a model system for the study of nonlinear dynamical systems, and offer the opportunity to answer open questions concerning, for example, the interplay between rotation and nonlinearity, and energy partition in nonlinear lattices, within an applied context. These topics are further complicated by the type of nonlinearity involved (i.e. contact nonlinearity relating the force applied to the spheres to their distance of approach), which is usually modeled as a power law, and is also tensionless.

In addition to macroscale granular crystals, which have been widely studied, microscale granular crystals have recently become more accessible to experiment via a combination of self-assembly fabrication techniques [6, 7] and laser-ultrasonic photoacoustic characterization methods [8, 9, 10]. These media are composed of ordered arrays of monodisperse spheres, which have diameters on the order of 1- to 100 μm. In this dissertation, we present recent progress in theoretical and computational modeling of wave dynamics in microscale granular crystals. The frequencies of the waves considered are well below the intrinsic spheroidal vibrational modes of the spheres, such that they may be treated as rigid bodies interacting via discrete springs that model normal and shear contact forces. The contact forces are modeled using Hertz-Mindlin theory [11, 12, 13]. In contrast to previous works on microscale GCs, this work considers nonlinear dynamics, which have been well-studied in macroscale GCs [5], as well as particle rotations, which have been studied in linear theoretical models and macroscale experiments (see Sec. 1.3). Particular attention is given to the interplay between nonlinearity and rotation. The remaining sections of this introduction contain a historical review of the works that enabled the study of microscale GCs, as well as an outline of the dissertation.

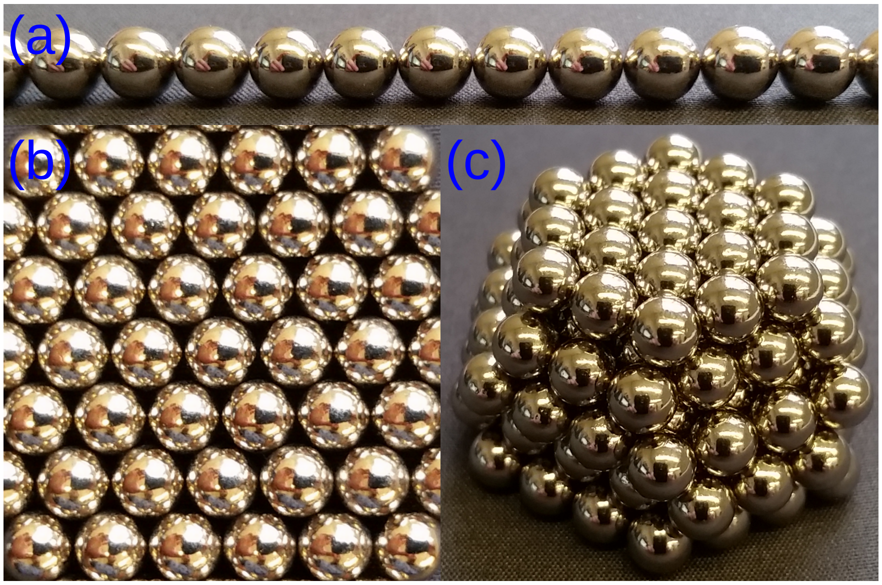

Figure 1.1: Images of example macroscale granular crystals. (a) One-dimensional. (b) Two-dimensional, hexagonal-close-packing. (c) Three-dimensional, hexagonal-close-packing.

1.2 Macroscale Granular Crystals

Mechanical waves in granular media have been studied extensively in ordered arrays of contacting particles (usually spheres), as shown in Fig. 1.1. These systems, called granular crystals (GCs), have been shown to exhibit linear to strongly nonlinear dynamics stemming from the contacts between neighboring particles [4, 5]. Granular crystals provide a means to conduct experiments on granular media in highly ordered and/or reduced dimensional settings, which facilitate comparison between models and experimental systems. Granular crystals have also been proposed for applications such as acoustic diodes [14], lenses [15], and impact absorbers [16].

1.2.1 Hertzian Contact

The interparticle contacts, which are typically assumed to be Hertzian [11, 13], have a nonlinear force-displacement relationship because the contact area increases with increasing compressive force. In the Hertz contact model, the contact force vs. displacement relationship is given by [11, 13]

$$F(\delta) = A\left[\delta_0 - \delta\right]_{+}^{3/2}, \tag{1.1}$$

where the contact force F is taken to be positive in compression, δ is the relative separation between the centers of the contacting particles, the static overlap δ_0 is the interpenetration distance between particles at equilibrium (determined by an applied static load, for instance), A is a stiffness parameter that depends on material and geometric properties, and the subscript $+$ sign indicates that the term $[\cdot]_+$ vanishes if the quantity inside the brackets is negative (indicating loss of contact). Note that the static overlap is much smaller than the particle size.

As seen in Eq. 1.1, the static overlap δ_0 acts as a characteristic length for the contact force, and the ratio $\max|\delta|/\delta_0$ (where $\max|\delta|$ is the maximum dynamic overlap of the GC) determines the relative strength of nonlinearity [4, 5]. If the maximum dynamic overlap is much smaller than the static overlap (i.e. $\max|\delta|/\delta_0 << 1$), the resulting dynamics are near-linear, and the contact force can be described by a first-order Taylor expansion of Eq. 1.1. In the case where the dynamic overlap is close to (but still less than) the static overlap (i.e. $\max|\delta|/\delta_0 < 1$), the dynamics are "weakly-nonlinear," i.e. the nonlinearity can be accounted for by including terms up to second or third order in the Taylor expansion of Eq. 1.1. Finally, if $\max|\delta|/\delta_0 >> 1$, the dynamics are considered "strongly-nonlinear," and the full nonlinear contact force law must be considered.

An important distinction must be made between contact nonlinearity, which is a direct consequence of nonlinear force-displacement relationships, and geometric nonlinearity stemming from large deformations of the lattice (i.e. when small angle approximations are no longer valid): contact nonlinearities are significant when the interparticle separation is on the order of the static overlap, while geometric nonlinearities become significant when deformations are on the order of the particle size (i.e. a few orders of magnitude larger). Thus, contact nonlinearities can enable strongly nonlinear behavior without displacements on

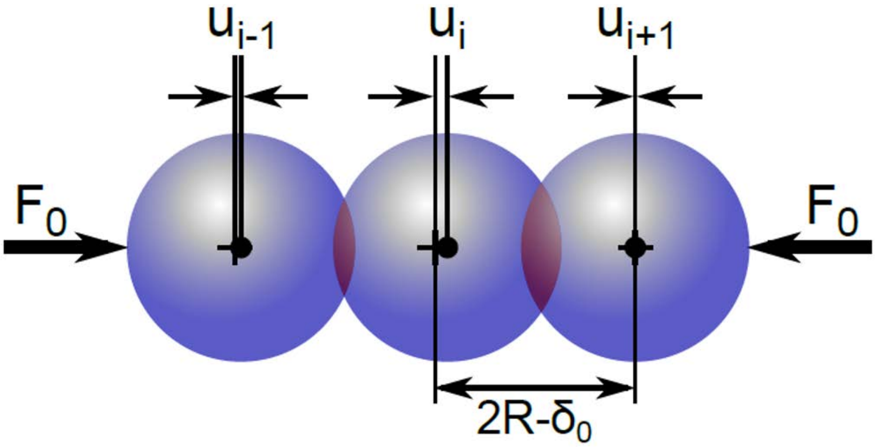

Figure 1.2: Schematic of a 1D granular crystal. Crosses denote the equilibrium positions of the sphere centers, and dots denote the current positions. The deformed contact regions are highlighted in red.

the order of the particle size. It should be noted that the contact nonlinearity is, in itself, a type of geometric nonlinearity, where the shape of the contact results in a nonlinear-force displacement relationship, while the particles can be considered to behave linearly elastic. However, we use "contact nonlinearity" to distinguish from geometric nonlinearity describing displacements on the order of the particle size.

1.2.2 One-Dimensional Granular Crystals

One-dimensional (1D) GCs are composed of chains of particles in contact. A schematic of a 1D GC is shown in Fig. 1.2, and the corresponding equations of motion are given by Eq. 1.2.

$$m\ddot{u}_i = A\left[\delta_0 + u_{i-1} - u_i\right]_+^{3/2} - A\left[\delta_0 + u_i - u_{i+1}\right]_+^{3/2} \tag{1.2}$$

Wave dynamics in 1D GCs have been studied extensively in near-linear, weakly-nonlinear, and strongly-nonlinear regimes [4, 5]. For a precompressed chain (i.e. $F_0 > 0$, resulting in $\delta_0 > 0$), the near-linear regime behaves as a 1D lattice of discrete masses connected by linear springs. Such lattices have been studied since the eighteenth century, when Newton attempted to derive a formula for the propagation of sound [17]. The primary difference between wave propagation in the discrete lattice and a similar continuous medium (longitudinal waves in a thin rod, for example) is that the former is dispersive, while the latter is not. That is, the group velocity of waves in the lattice (or equivalently the phase velocity and frequency) depends on wavelength. This arises because the lattice has a characteristic length scale (in this case, the interparticle spacing), which has an increasing effect on wave propagation as the wavelength approaches this value. Dispersion causes a wave packet, which may be initially localized in space, to spread out; in the case of the 1D lattice, the components with long wavelengths and low frequencies travel fastest.

In the weakly nonlinear regime (i.e. $|u_{i-1} - u_i| < \delta_0$ in Eq. 1.2), the chain can be modeled using a 1D lattice with anharmonic springs, where the spring force-displacement relationship has linear and quadratic parts [4]. This nonlinear lattice model is a special case of the Fermi-Pasta-Ulam (FPU) lattice [18], which is a classical system in the study of nonlinear waves. It has long been known that for wavelengths well above the lattice spacing, waves in the FPU chain may be described by the Korteweg de Vries (KdV) equation, which is a nonlinear, dispersive partial differential equation that has been integral to the study of nonlinear wave propagation, and has a wide body of associated literature [19]. One of the most well-known features of the KdV equation is that it supports the propagation of solitary waves, which are packets of wave energy that are localized in space and propagate without changing shape (despite the presence of dispersion), with amplitude-dependent wave speeds and spatial widths. This unchanging shape is the result of a perfect balance between dispersion and nonlinearity; while dispersion would tend to spread out the wave packet, nonlinearity causes a localizing effect, and the balance between these phenomena enables the solitary wave.

In the strongly-nonlinear regime (i.e. $|u_{i-1} - u_i| >> \delta_0$ in Eq. 1.2), the nonlinear contact forces cannot be well-described using a Taylor series with a few nonlinear terms. Thus, the complete power law nonlinearity of the Hertz model must be used. While the problem is significantly more complicated than the weakly-nonlinear case, solitary waves have been modeled analytically and observed in many experiments [4, 5, 20, 21]. In contrast to the KdV-type solitary waves of the weakly-nonlinear regime, which decay exponentially to zero intensity and have variable width, these strongly nonlinear analogues decay more rapidly in space have a fixed spatial width (on the order of five particle lengths) [4]. However, theoretical descriptions of the decay profile have been (and continue to be) debated. In the earliest theoretical analyses, a continuum approximation of the strongly nonlinear chain yielded *compactly supported* solitary wave solutions; that is, they decay from the peak intensity to zero in finite distance [4]. In later works, use of the fully discrete model, combined with an iterative numerical scheme, resulted in solitary waves with double exponential decay profiles [20, 21].

Examples of the dynamics in the near-linear, weakly-nonlinear, and strongly-nonlinear regimes are illustrated by results from simulations of a 1D GC composed of 80 spheres, as shown in Fig. 1.3(a-c) for near-linear, weakly-nonlinear, and strongly-nonlinear cases, respectively. In each simulation, the first particle in the chain is given an initial velocity, the magnitude of which determines the dynamical regime. Time histories of the velocity of the 30th sphere are shown in Fig. 1.3(d-f), corresponding to the cases in 1.3(a-c).

For an uncompressed chain (i.e. $F_0 = 0$), wherein the individual particles are barely touching at equilibrium, there is no resistance to tension, and therefore no linear sound speed; thus, uncompressed chains exhibit strongly nonlinear dynamics, even at vanishing amplitudes. This property is known as a "sonic vacuum" [4]. The speed of wave propagation in a sonic vacuum depends on amplitude, and goes to zero as the amplitude vanishes. A connection can be made between the sonic vacuum and the strongly-nonlinear regime of a precompressed chain: the two systems are equivalent at very high amplitudes, for which the static compression is insignificant to the dynamic behavior.

1.2.3 Two- and Three-Dimensional Granular Crystals

Granular crystals have also been studied in 2D and 3D. Past works have included computational [22, 23] and experimental [24, 25] studies of nonlinear waves in uncompressed GCs, as well as experiments on compressed GCs in the linear regime [26, 27].

Analytical models have been developed in the linear regime for GCs with shear interactions

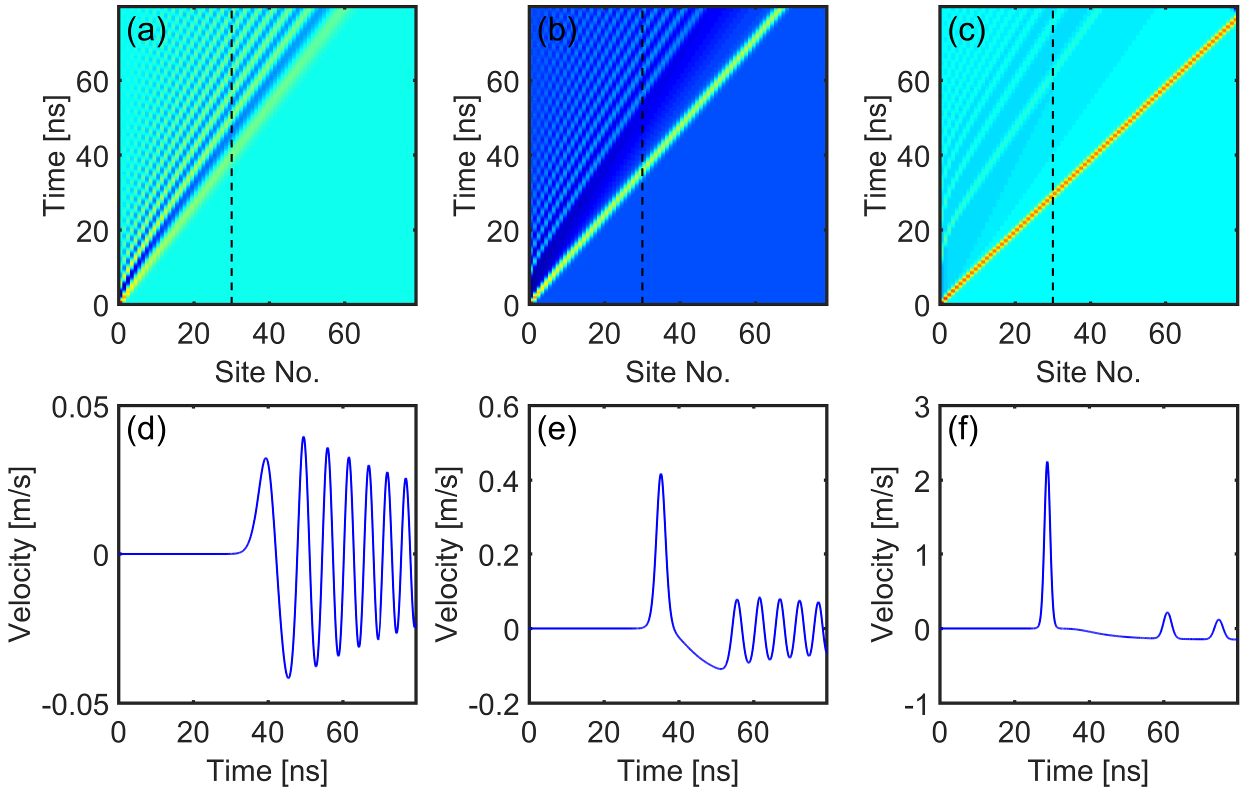

Figure 1.3: (a-c): Spatiotemporal plots of particle velocity for a simulated chain of 80 microscale spheres, for (a) near-linear, (b) weakly-nonlinear, and (c) strongly-nonlinear cases. (d-f): Time histories of velocity of the 30th sphere corresponding to (a-c). Dashed black lines in (a-c) indicated the lattice site whose time history is shown in (d-f).

and rotations, focusing especially on the dispersion of bulk modes for various packings in 2D [28, 29] and 3D [30]. Very recently, this theory has been extended to membrane modes [31], as well as to surface and edge states [32, 33]. The effects of shear contact forces and rotations are discussed in more detail in the following section.

While these past works have studied both linear and nonlinear GCs in 2D and 3D, sometimes including shear and rotation, the interplay between nonlinearity and rotation remains an open problem, and will be addressed in this thesis.

1.3 Influence of Shear Interactions and Particle Rotations

Intuitively, one should realize that Hertzian normal forces alone do not fully describe the interactions between particles in a granular medium; shear forces and rotations must be accounted for in general. In the case of a 1D GC that is uncompressed or undergoes exclusively longitudinal motion, the contributions from shear interactions and rotations should be minimal (due to vanishing contact surface area and symmetry considerations, respectively). However, for a precompressed GC in 2D or 3D, or a 1D GC attached to a substrate (or some other boundary), the effects of shear and rotation can dramatically influence wave propagation. This section contains a brief review of the phenomena that can arise due to these effects.

1.3.1 Shear Contact Interactions

Resistance to shearing deformation between two particles in contact can be modeled by Hertz-Mindlin theory [12, 13], which provides a relationship between the relative transverse displacement between the particles (i.e. in a direction parallel to the contact plane) and the elastic restoring force. This restoring force is derived from linear elasticity and neglects friction and sliding at the contact interface. The effective shear stiffness depends on the compression normal to the contact surface, which is assumed to obey Hertz theory. The shear force, as a function of both transverse and normal displacements, is given by

$$F_t(\delta_t, \delta_n) = B\delta_t \left[\delta_n\right]_+^{1/2}, \tag{1.3}$$

where δ_t and δ_n are the transverse and normal relative displacements, respectively, and B is a constant that depends on material and geometric properties of the particles. As shown by Eq. 1.3, the shear force varies linearly with the transverse displacement δ_t, and varies nonlinearly with the normal displacement.

While the shear force-displacement relationship given by Eq. (1.3) is relatively simple, which makes it amenable for use in theoretical and computational models, it possesses an important limitation that should be kept in mind; namely, that linear elasticity predicts singularities in the stress at the edges of the contact interface [13]. This causes microslip that initiates at the edge of the contact, and propagates inward if transverse loading is increased. This microslip has been accounted for in more complex models, and causes a softening nonlinearity for large transverse loading [12, 13, 35]. Despite this, the simplified model given by Eq. (1.3) is a good approximation for small transverse displacements.

1.3.2 Rotational Waves in the Linear Regime

The presence of particle rotations causes changes in wave propagation, and must be considered when the characteristic size of the particles is on the order of the interparticle separation distance [36]. This is in contrast to a standard elastic solid, in which it is typically assumed that the particle size is negligibly small compared to the spacing. In the theory of 2D and 3D GCs, rotations have been shown to create additional dispersion of waves, as well as to give rise to additional plane wave modes, which may have purely rotational motion, or have a combination of rotational and translational displacements [28, 29, 30, 31, 34]. Note that, for plane waves traveling in high-symmetry directions of the GC, the longitudinal motion is often decoupled from the transverse and rotational motions. Rotational waves have also been observed in macroscale experiments [27].

Recently, rotational modes have been modeled and observed experimentally in chains of magnetically precompressed spheres on a substrate [37, 38]. This system differs from the precompressed, 1D GC studied previously in that the rotational and transverse translational degrees of freedom give rise to more modes and the presence of the substrate creates an on-site potential, which gives rise to a low-frequency band gap (that is, waves cannot propagate at frequencies below a certain threshold).

1.3.3 Theory of Generalized Continua

While granular media are composed of discrete particles, it is often desirable to model them as continuous media. This way, the medium can be modeled using a few partial differential equations, as opposed to the theoretically infinite number of ordinary differential equations that are needed in discrete element models (DEMs). However, the process of obtaining an accurate continuum model (so-called "homogenization") of a GC is far from trivial, as the effects of particle size and rotation (not present in classical linear elastic solids) must be taken into account. To achieve such a model, past works have relied on the theory of "generalized continua," which pertains to a broad area of continuum mechanics in which some of the constraints of classical elasticity are relaxed [39].

One of the more well-known examples of a generalized continuum, which is often chosen to model granular media, is the "Cosserat medium." The Cosserat medium was first studied in the early 1900s [40], and treats the material points of a deformable solid as rigid bodies, instead of infinitesimal points (as in classical elasticity). The use of rigid bodies permits micro-rotations (i.e. rotations of individual material points, unlike so-called "macro-rotations," which exist in classical elasticity as the curl of the displacement field). An important consequence of micro-rotation is that the stress tensor becomes asymmetric, and additional restoring moments (known as "couple stresses") must exist to maintain the conservation of angular momentum. The assumption of rigid bodies also imposes a characteristic length scale (the particle size), which manifests itself in wave propagation as dispersion, and causes a static state of stress to deviate from that of a classical elastic solid if the size of the structure is on the order of the particle size [41].

It should be noted that, while the Cosserat medium has historically been accepted as a model for granular media, it is not without its shortcomings: in a recent work, it was observed that the dispersion of rotational waves in macroscale GCs did not agree with the predictions of Cosserat theory [27]. To address this issue, an enhanced micropolar continuum model, which includes additional dispersive terms to account for the periodicity of GCs, has recently been developed [42]. These higher-order dispersive terms may have important ramifications for nonlinear dynamics as well, as the formation of solitary waves is reliant upon a balance between dispersion and nonlinearity. Thus, continuum modeling of granular media remains a developing problem, even in the linear regime.

1.4 Microscale Granular Crystals

While the macroscale GCs that have been well-studied thus far have provided an excellent platform to study nonlinear dynamics, their potential for future applications may be limited by their large size (on the order of meters). In the years leading up to the work in this thesis, microscale granular crystals have emerged as an intriguing research field. Using spheres with diameters on the order of microns, one can create a GC containing millions of particles, that fits on the surface of a small glass slide, as shown in Fig. 1.4. Using conventional, "top-down" microfabrication methods, the time of assembly scales linearly with the number of particles needed; this results in an impracticably large fabrication time for a structure with millions of particles. To solve this problem, past studies have turned to self-assembly techniques, which use a "bottom-up" approach [6, 7, 43, 44, 45, 46]. Using this approach, large numbers of particles can be assembled simultaneously, resulting in much more rapid fabrication. A scanning electron microscope image of a typical microscale GC is shown in Fig. 1.5.

Waves propagating in microscale GCs have contact-based modes with characteristic frequencies up to hundreds of megahertz [8]. Thus, they have potential applications for signal processing or ultrasonic wave tailoring. Additionally, their small overall system size makes them candidates for shock or vibration mitigation in these regimes, and have potential for use in smaller devices than their macroscale counterparts. While it would be convenient if the dynamics of microscale GCs were simply time re-scaled analogues of the well-known macroscale dynamics, this is not the case: the relevant physics are different at microscale. For example, microscale granular crystals are affected by interparticle adhesion, which is several orders of magnitude

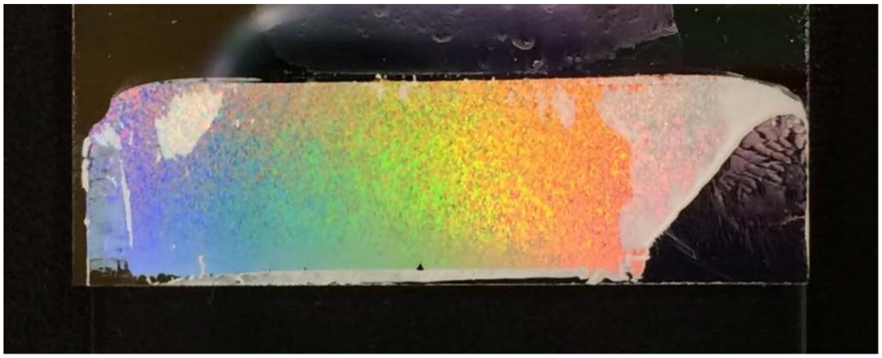

Figure 1.4: Macroscopic view of a microscale GC, fabricated using a convective self-assembly technique.

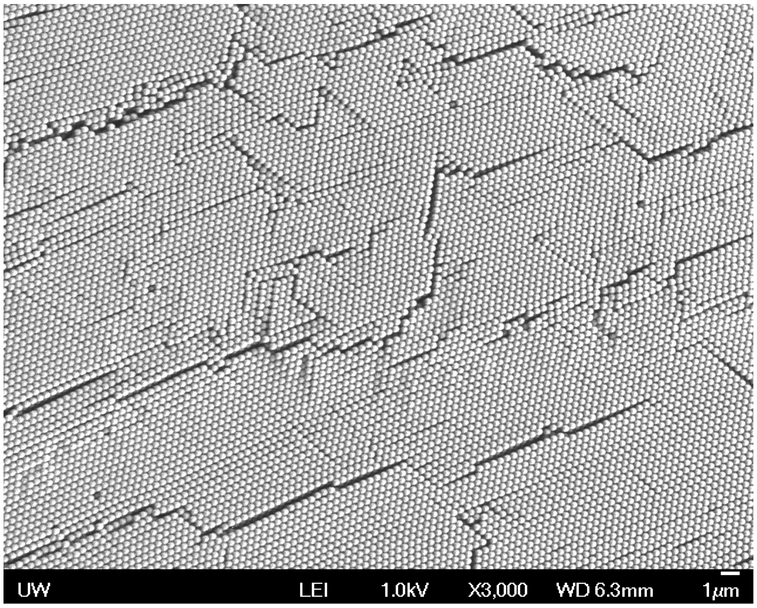

Figure 1.5: Scanning electron microscope image of a microscale granular crystal. Photo courtesy of Amey Khanolkar.

stronger than the force exerted by gravity on particles at that length scale [3]. In the works presented here, the Derjaguin-Muller-Toporov (DMT) adhesion model [47, 48] is used. In the DMT model, which is valid for small, stiff particles, the adhesive force is assumed to be a static, short range, attractive force, which induces a static precompression of the GC. If the spheres were more compliant, it may be necessary to instead use a different adhesion model; for example, the Johnson-Kendall-Roberts model accounts for hysteresis due to necking near the contact interface during unloading, and is valid for large, soft spheres [49]. Other characteristics of adhesion can be included via more complex models, such as the Maugis-Dugdale model [50], which is parameterized by the dimensionless Tabor parameter [51] and has the DMT and JKR models as its extremes, or various elasto-plastic models [52, 53, 54]. Note that precompression induced by adhesion differs from the external precompression used in the macroscale case: here, the GC is compressed by internal forces, so contacts may be broken and reformed elsewhere, which can result in widespread structural rearrangement without collapse, and lower density structures. This compression also linearizes the dynamics at low amplitudes, and the uncompressed, sonic vacuum system does not exist.

To examine the dynamical behavior of microscale GCs in experiments, recent works [8, 55, 56, 57] have utilized photoacoustic characterization techniques, typically involving laser ultrasonic pump-probe methods. These include transient grating spectroscopy [9, 10], in which a single wavelength can be excited and selectively probed using the interference fringe pattern of two intersecting laser beams; knife-edge photodeflectometry [58], which is sensitive to changes in the slope of a probed surface; and grating interferometry [59], which is sensitive to displacements perpendicular to the probe beam.

The recent (and continuing) experimental realization of microscale GCs, along with the complexities brought on by changing physics at microscale, call for concurrent advances in modeling from the near-linear to strongly-nonlinear regimes. In particular, the inclusion of shear interactions and rotation, which are necessitated by the powerful compression induced by adhesive forces, as well as their interplay with nonlinearity, should reveal rich dynamical behavior.

1.5 Organization of this Thesis

The work in this thesis extends the body of knowledge concerning the dynamics of microscale granular media by examining the following topics:

- In Chapter 2: "A Self-Assembled Metamaterial for Lamb Waves," we extend the work of Ref. [8] by modeling a locally-resonant metamaterial composed of a microscale GC adhered to an elastic membrane. Since the substrate used in this model has finite thickness, the contact-based modes of the GC couple to Lamb waves (as opposed to the Rayleigh waves as in Ref. [8]).

- In Chapter 3: "Discrete Breathers in a Mass-in-mass chain with Hertzian Local Resonators," we examine the dynamics of locally-resonant metamaterials composed of microscale GCs adhered to substrates when the microsphere vibration amplitude is large enough to engage nonlinearity of the Hertzian contact between the spheres and the substrate. The substrate is modeled as a discrete chain of lumped masses connected by linear springs, and the microspheres are modeled as local resonators attached with nonlinear springs. We examine the specific phenomena of nonlinear intrinsic localized modes or "discrete breathers."

- In Chapter 4: "Dynamics of a Monolayer of Microspheres on an Elastic Substrate," we develop an improved linear monolayer model (compared to the models of Ch. 1 and Ref. [8]) by including the effects of interparticle interactions, shear contact forces, and rotational dynamics. The contact-based modes of the monolayer involve 2D translations and rotations in the sagittal plane.

- In Chapter 5: "Nonlinear Dynamics of a 1D Granular Crystal Adhered to a Substrate," we extend the improved monolayer model presented in Ch. 4 into the weakly nonlinear regime. The Nonlinear Schrodinger equation is derived and used to model slow, nonlinear modulations of the contact-based modes developed in the previous chapter.

- In Chapter 6: "Shear to Longitudinal Mode Conversion via Second Harmonic Generation in a 2D Microscale Granular Crystal," we model weakly-nonlinear plane waves in a 2D microscale GC with shear interactions and rotation. In this model, the spheres undergo 2D translations in the plane of the monolayer and rotations about an axis out of plane.

- Finally, in Chapter 7: "Energy Partition in a 2D Microscale Granular Crystal Subject to an Impulsive Point Load: Multibody Dynamics Simulation," we simulate the response of a halfspace composed of microspheres to an impulsive point source and examine the characteristics of bulk and surface waves as a function of amplitude.

Acknowledgments of collaborators and funding sources are found in Appendix A. Details of the computational methods used, as well as commentaries on the effectiveness of these techniques as applied to the study of microscales GCs, are found in Appendix B.

Chapter 2

A SELF-ASSEMBLED METAMATERIAL FOR LAMB WAVES[1]

2.1 Introduction

Locally resonant acoustic metamaterials are a type of composite material that have been the subject of intense study over the past fifteen years [60] due to their ability to exhibit extreme [61], anisotropic [62], negative [63, 64, 65], strongly absorbing [66], and locally-tailorable [67] effective properties. These unique properties stem from the interaction of propagating acoustic waves with subwavelength resonant elements forming the composite [68, 69]. This can present fabrication challenges as wavelengths are reduced, including challenges involved with constructing the resonators themselves, and in making large areas of composite containing such complex microstructure. In this respect, as described in Ch. 1, colloidal self-assembly is a promising solution, as it has been shown to enable the simple, inexpensive, and fast fabrication of complex, ordered structures composed of nano- or microscale elements in one to three dimensions [43, 44, 45]. These advantages have driven the use of self-assembly strategies in multiple areas, particularly in the design of phononic crystals [70, 71], photonic crystals [70, 72, 73], plasmonic sensors and nanostructures [74, 75, 76], and surfaces with tailored wettability [77]. Despite this wide use, there are few examples of locally resonant acoustic metamaterials fabricated using self-assembly techniques [8, 78, 79, 80, 81].

Lamb waves are a type of acoustic waveguide mode that occur in thin elastic plates and membranes [82] that play an important role in nanomechanical resonator [83] and sensing applications [84]. They have also been utilized in studies of sub-THz phonon transport with implications for the understanding of nanoscale thermal phenomena [85]. Recently, several examples of locally resonant metamaterials for Lamb waves have been explored

---

[1] The work in this chapter is adapted from Ref. [55].

in both theoretical [86, 87, 88] and experimental [89, 90, 91, 92] settings. However, in each of the experimentally realized cases, the resonant elements forming the metamaterial had frequencies ranging from the audible regime to a few megahertz and were made using conventional machining or microfabrication techniques.

In this work, we present a theoretical model of a self-assembled, locally resonant metamaterial for Lamb waves. This work extends the work of Ref. [8], which described a locally-resonant metamaterial for Rayleigh SAWs, composed of a microsphere array (microscale granular crystal) on a thick substrate. The metamaterial herein is composed of a self-assembled monolayer of microspheres, forming a microscale granular crystal, adhered to the surface of a thin silicon membrane. As a result of the adhesion, the microspheres have a contact resonance where the microsphere oscillates like a rigid body, with a localized region of elastic deformation around the point of contact with the substrate. In our system, the contact resonance plays the role of the metamaterial locally resonant element and has a frequency of 200 MHz. This type of metamaterial may have potential advantages for acoustic wave tailoring applications, as arrays of macroscale spherical particles have been shown to support unique nonlinear dynamical phenomena due to the Hertzian relationship [11] between spherical elastic particles in contact [4, 5].

2.2 Theoretical Model

To study Lamb wave propagation in our metamaterial, we adopt a similar approach as the one used previously to describe the interaction of a contact resonance of microspheres with Rayleigh SAWs [8]. We note that the spheroidal resonance may similarly couple to SAWs in the substrate, however we do not consider this in our current model. We model the microspheres as an array of linear surface oscillators (without interparticle coupling) that move in the Z direction, with mass m and linearized normal contact stiffness K attached to the top surface of the thin silicon membrane with thickness $2H = 1.3$ μm, as illustrated in Fig. 2.1. The thickness of the membrane was measured with ellipsometry in Ref. [55]. The microsphere mass m is calculated from the polystyrene density $\rho_s = 1.06$ g/cm^3 [55]. Because the frequency of the lowest frequency spheroidal mode is much higher than the

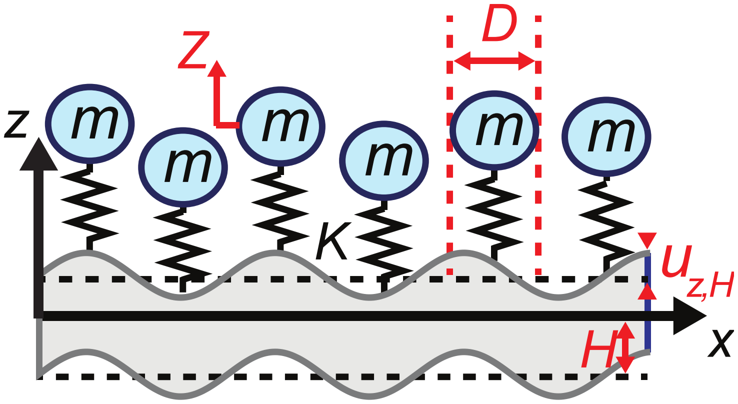

Figure 2.1: Schematic of the membrane metamaterial.

contact resonance frequency and the elastic deformation highly localized, we describe the entire mass of the microsphere moving in a rigid-body-like motion at frequencies near the contact resonance. Since the acoustic wavelength is much larger than the sphere size, we use an effective medium approach and approximate the average normal stress at the surface as the force exerted by the microsphere divided by the area of a unit cell [8].

2.3 Derivation of the Lamb Wave Dispersion Relation

Elastic waves in the membrane are described by wave equations $\nabla^2\phi = \frac{1}{c_L^2}\frac{\partial^2\phi}{\partial t^2}$ and $\nabla^2\psi = \frac{1}{c_T^2}\frac{\partial^2\psi}{\partial t^2}$, where t is time, and ϕ and ψ are dilational and transverse potentials, respectively, which are related to the displacement components u_x and u_z as follows: $u_x = \frac{\partial\phi}{\partial x} - \frac{\partial\psi}{\partial z}$ and $u_z = \frac{\partial\phi}{\partial z} + \frac{\partial\psi}{\partial x}$. Assuming a traveling wave solution of the form $\phi = f(z)e^{i(\omega t-kx)}$ and $\psi = g(z)e^{i(\omega t-kx)}$, we obtain solutions to the wave equations of the form [93]:

$$\begin{aligned}\phi(x,z,t) &= [C_1\sinh(q_L kH) + C_2\cosh(q_L kH)]e^{i(\omega t-kx)}\\ \psi(x,z,t) &= [C_3\sinh(q_T kH) + C_4\cosh(q_T kH)]e^{i(\omega t-kx)},\end{aligned} \tag{2.1}$$

where $q_L = \sqrt{1-\frac{\omega^2}{k^2c_L^2}}$, $q_T = \sqrt{1-\frac{\omega^2}{k^2c_T^2}}$, and H is the membrane half-thickness. The stress boundary conditions at the upper and lower membrane surfaces are:

$$
\begin{aligned}
\sigma_{zz}(x,+H,t) &= \frac{K}{A}(Z-u_{z,H})\\
\sigma_{zz}(x,-H,t) &= 0\\
\sigma_{xz}(x,+H,t) &= 0\\
\sigma_{xz}(x,-H,t) &= 0,
\end{aligned}
\tag{2.2}
$$

where $A=\sqrt{3}D^2/2$ is the area of a primitive unit cell in the hexagonally packed monolayer. The equation of motion for the surface oscillator can be written as:

$$m\ddot{Z}+K(Z-u_{z,H})=0. \tag{2.3}$$

We assume a traveling wave solution for the oscillator motion of the form

$$Z=Fe^{i(\omega t-kx)}. \tag{2.4}$$

By substituting Eq. 2.1 and Eq. 2.4 into Eq. 2.2 and using isotropic linear elastic stress-strain relations [93], we obtain (after algebraic manipulation) the dispersion relation in the form

$$
\begin{vmatrix}
0 & 0 & \beta_1\cosh(q_LkH) & \beta_4\cosh(q_TkH) & \frac{-m\omega^2}{2\rho_m Ak^2c_T^2}\\
0 & 0 & \beta_3\sinh(q_LkH) & \beta_2\sinh(q_TkH) & 0\\
\beta_1\sinh(q_LkH) & \beta_4\sinh(q_TkH) & \beta_1\cosh(q_LkH) & \beta_4\cosh(q_TkH) & 0\\
\beta_3\cosh(q_LkH) & \beta_2\cosh(q_TkH) & \beta_3\sinh(q_LkH) & \beta_2\sinh(q_TkH) & 0\\
-kq_L\cosh(q_LkH) & ki\cosh(q_TkH) & kq_L\sinh(q_LkH) & -ki\sinh(q_TkH) & \frac{\omega^2}{\omega_c^2}-1
\end{vmatrix}=0,
\tag{2.5}
$$

where the contact resonance frequency $\omega_c=\sqrt{K/m}$, $\beta_1=1+q_T^2$, $\beta_2=-(1+q_T^2)$, $\beta_3=-2iq_L$, and $\beta_4=-2iq_T$. After expanding and simplifying the determinant in Eq. 2.5, we express the dispersion relation in the reduced form[2]

---

[2] See Appendix B for comments on algebraic manipulation of determinants.

$$\left(\frac{\omega^2}{\omega_c^2} - 1\right) D_1 D_2 = \frac{-m\omega^4 q_L}{2\rho_m A k^3 c_T^4} \left[\sinh\left(q_L k H\right) \sinh\left(q_T k H\right) D_1 + \cosh\left(q_L k H\right) \cosh\left(q_T k H\right) D_2\right], \tag{2.6}$$

where $D_{1,2}$ are determinants whose zeros comprise the dispersion relations of uncoupled, purely flexural and dilatational modes (respectively) in a membrane with stress-free boundary conditions [93], and can be written as:

$$\begin{aligned} D_1 &= \begin{vmatrix} \beta_1 \sinh\left(q_L k H\right) & \beta_4 \sinh\left(q_T k H\right) \\ \beta_3 \cosh\left(q_L k H\right) & \beta_2 \cosh\left(q_T k H\right) \end{vmatrix} \\ D_2 &= \begin{vmatrix} \beta_1 \cosh\left(q_L k H\right) & \beta_4 \cosh\left(q_T k H\right) \\ \beta_3 \sinh\left(q_L k H\right) & \beta_2 \sinh\left(q_T k H\right) \end{vmatrix}. \end{aligned} \tag{2.7}$$

The term in parentheses on the left-hand side of Eq. 2.6 describes the contact resonance of the oscillators. The right-hand side is responsible for the coupling between the oscillators, and flexural and dilatational Lamb waves.

2.4 Discussion

In Ref. [55], the contact resonance frequency was determined from experimental data to be $f_c = 200$ MHz. We plot the theoretical dispersion curves calculated[3] using this fitted contact resonance frequency in Fig. 2.2, which is reproduced from Ref. [55]. The theoretical dispersion curves show coupling between the flexural and dilatational modes due to the presence of the spheres adhered to one side of the membrane. In contrast to the coupling between Rayleigh SAWs and the microsphere contact resonance [8], the middle branch (as denoted in Fig. 2.2) does not stop at the line corresponding to transverse polarized bulk waves, and remains non-leaky due to the confinement of the membrane. This results in a second

---

[3] See Appendix B for details about numerical solution of dispersion equations.

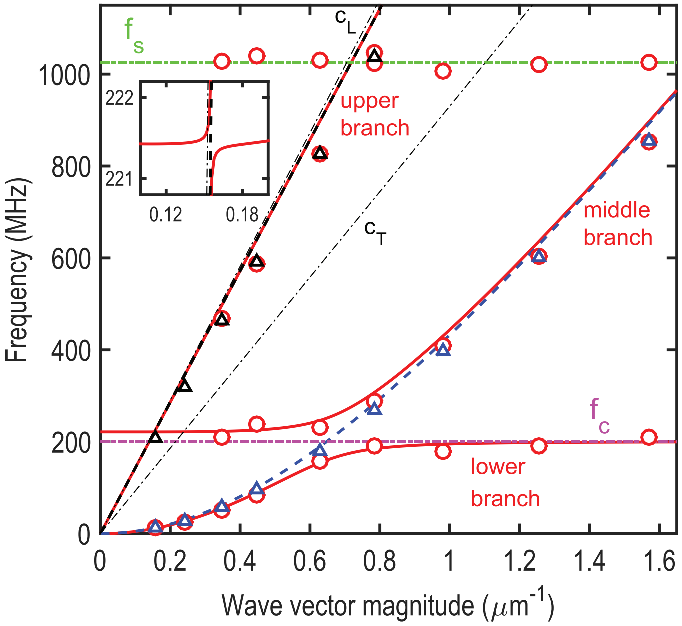

Figure 2.2: Dispersion relations. The circle and triangle markers are the measured frequency peaks for membranes with and without spheres, respectively. The solid red line is the dispersion calculated using our model. The dashed black line corresponds to the calculated S_0 modes and the dashed blue line to A_0 modes in the without-spheres case. The black dash-dot lines correspond to bulk waves in silicon. The horizontal lines denote the frequencies of the fitted microsphere contact resonance and identified spheroidal resonance. The inset shows a closer view of the predicted avoided crossing with the S_0 branch.

hybridization between the middle and the S_0 branch. The inset in Fig. 2.2 shows a closer view of this intersection, which is smaller than the avoided crossing near the A_0 branch. The larger avoided crossing with the A_0 branch demonstrates stronger coupling between flexural motion and the contact resonance than with dilatational motion. This stronger coupling is a result of flexural modes having large out-of-plane displacement that couples with the vertical motion of the surface oscillators, in contrast to dilatational modes, which have predominantly in-plane displacements.

2.5 Conclusion

We have presented a theoretical model of a self-assembled, locally resonant metamaterial for Lamb waves, which is formed from a 2D microscale granular crystal adhered to thin substrate. The model describes an array of uncoupled oscillators as in Ref. [8], but in contrast, considers the particles to be adhered to a thin, instead of thick, substrate. With high characteristic frequencies and small length scales, this metamaterial holds promise for the development of new types of devices involving Lamb waves. Since the response is sensitive to the state of the contact, these metamaterials may have potential applications as sensors for humidity, temperature, and micro/nanoscale material properties, and serve as a platform for the exploration of microscale contact mechanics. Because of the scalability enabled by self-assembly, this type of metamaterial may enable future studies that explore the interaction of local mechanical resonances with even higher-frequency phonon transport. Finally, the use of self-assembly approaches may offer significant advantages for producing acoustic metamaterials inexpensively and on a large scale.

Chapter 3

DISCRETE BREATHERS IN A MASS-IN-MASS CHAIN WITH HERTZIAN LOCAL RESONATORS[1]

In this chapter, we report on the existence of discrete breathers in a one-dimensional, mass-in-mass chain with linear intersite coupling and nonlinear, precompressed Hertzian local resonators, which is motivated by studies of the dynamics of microscale granular crystals adhered to elastic substrates (such as the linear models of Ref. [8] and Ch. 2). This chapter builds upon the previous chapter, and the model presented in [8], by considering dynamic phenomena stemming from nonlinearity and damping in the particle-substrate contact. We analyze the frequency-amplitude dependence of the breathers by performing numerical continuation on a linear eigenmode (vanishing amplitude) solution of the system near the upper band gap edge. Finally, we use direct numerical integration of the equations of motion to demonstrate the formation and evolution of the identified localized modes in energy-conserving and dissipative scenarios, including within settings that may be relevant to future experimental studies.

3.1 Introduction

Materials containing local resonators, such as the adhered microscale granular crystals of Ref. [8] and Ch. 2, are known to support unique dynamic phenomena, such as negative, highly anisotropic, and extreme effective properties [60, 95]. One well-known model for locally-resonant materials is a chain of “mass-in-mass” unit cells, which consists of a lattice of interconnected lumped masses, each with coupled local resonators [96]. By incorporating nonlinearity into locally resonant metamaterials, their dynamics become more complex.

---

[1] The work in this chapter is adapted from Ref. [94]. Copyright 2017 by the American Physical Society.

For example, metamaterials for both acoustic [60, 97] and electromagnetic [97] waves have demonstrated numerous nonlinear phenomena, including tunability, harmonic generation, and the existence of nonlinear localized modes.

A promising means to create nonlinear acoustic metamaterials is provided by granular media, which have been used to demonstrate numerous nonlinear effects, including solitary waves, shocks, discrete breathers, tunable band gaps, frequency conversion, and non-reciprocal wave propagation [4, 5, 98, 99]. Recent theoretical and experimental works have combined the concepts of locally resonant metamaterials with granular media. Relevant contexts include, but are not limited to, frequency shifting, harmonic generation, and localized band gap modes [100], traveling waves, including ones with non-vanishing tails [101, 102], wave interaction [103], and localized and extended modes [104], as well as temporally periodic breathing states [105, 106] (to which we will return in what follows). In each of these examples, the granular media provided a nonlinear intersite coupling, while the local resonators were linear. Less attention has been paid to cases in which granular particles play the role of nonlinear local resonators.

In this work, we consider a one-dimensional, mass-in-mass system with linear intersite coupling and nonlinear local resonators that follow the Hertzian contact model with precompression. One motivation for considering this model is its relevance in describing a granular metamaterial consisting of a monolayer of microscale spheres adhered to a substrate, wherein surface localized elastic waves, such as Rayleigh surface acoustic waves (SAWs) and Lamb modes, have been shown to hybridize with the contact resonances of adhered microsphere arrays (microscale granular crystals) in thick [8, 56] and thin (Ch. 2 and[55]) substrates, respectively. Within this context, we imagine the portion of the substrate through which the localized elastic wave is traveling to be a linearly coupled chain that is locally coupled to an array of nonlinear resonators representing the microspheres.

Systems similar to the one-dimensional, linearly coupled chain with nonlinear local resonators considered here have been previously explored. For example, amplitude-dependent band-gaps have been studied in a one-dimensional linear chain with local resonators containing a cubic nonlinearity [107]. Other relevant works have also considered linear chains with nonlinear coupling to a rigid foundation [108], or a nonlinear local attachment [109], demonstrating heavily enriched dynamics caused by small nonlinear perturbations.

The structure of interest in the present work is the discrete breather (DB). Discrete breathers are solutions that are periodically oscillating in time and exponentially localized in space [110, 111] that have been studied theoretically and experimentally in many settings, involving a wide array of physical mechanisms [112, 113]. More recently, DBs have been demonstrated in theoretical [114, 115] and experimental [116, 117, 118] studies of ordered granular chains without local resonators, and theoretically in the presence of linear local resonators [105, 106], as well as in nonlinear, locally resonant magnetic metamaterials [119, 120, 121] and systems of electromechanical resonators [122].

We use our model to describe a locally resonant granular metamaterial for Rayleigh SAWs, consisting of a monolayer of microspheres adhered to a thick elastic substrate. The two independent model parameters are fit to an experimental system used in past work [8], so as to provide realistic parameter values to the model wherever possible. Beginning with the Hamiltonian version of our model, we examine the frequency-energy dependence of the DBs along a numerically computed branch of solutions. We then study the formation and evolution of the DBs via direct numerical simulations, considering both energy-conserving and dissipative cases, including within contexts that may be relevant to future experimental studies. While these results are presented in the context of a specific microscale system, we note that our model is given in dimensionless form, such that the results presented herein can be applied and extended to related systems via a suitable choice of parameters (for example, one could create a model macroscale, locally-resonant chain similar to the one studied in Ref. [100], but instead use linear springs to connect the main chain and Hertzian contacts in the internal resonators).

3.2 Model

3.2.1 Motivating Physical Scenario

Our chosen motivating physical scenario is shown in the schematic of Fig. 3.1(a), which describes sagittally-polarized, plane SAWs traveling along the surface of a thick substrate. Rayleigh SAWs are surface localized elastic waves that travel along a solid surface (represented as an elastic half space in theoretical descriptions), and have both in- and out-of-plane (with respect to the sample surface plane) displacement components [93]. Previous studies on monolayers of microspheres adhered to thick substrates have shown that Rayleigh SAWs in the substrate hybridize with, and excite, microsphere contact resonances having translational out-of-plane [8], and coupled, in-plane, translational and rotational motion [56, 137] (as will be described in further depth in Ch. 4). The hybridization with each of these resonances leads to classic "avoided crossing" phenomena [155] characteristic of locally resonant metamaterials and mass-in-mass chains. For the analysis herein, we focus on the avoided crossing with the contact resonance having solely out-of-plane motion [8, 56, 137]. Because a plane SAW is confined to the surface of the medium, it can be considered as traveling in one dimension, and as such, we represent the portion of the substrate through which the SAW is traveling as an infinite lattice of lumped masses m_1 connected by springs with linear stiffness k_1. Because the contact-based modes of the microspheres [8, 56, 123, 156] have frequencies much lower than the intrinsic spheroidal vibrational frequencies of the isolated spheres [124] (e.g. for the microspheres studied in Ref. [8], the out-of-plane contact resonance was measured to be 215 MHz, while the spheroidal resonance was predicted to be 2.9 GHz), we model the microspheres as point masses (of mass m_2) connected to the main chain by nonlinear springs modeling Hertzian contact with a static adhesive load. The resulting discrete model of our locally resonant granular metamaterial is shown in Fig. 3.1(b). As can be seen in Fig. 3.1(b), the chain elements are both drawn such that their motion is in the horizontal direction. We note that this depiction simply represents the coupling between a substrate (or chain) and a resonator, each having a single degree of freedom with the same, albeit arbitrary, direction of motion. Within the context of the previously described physical scenario, this degree of freedom represents out-of-plane motion of the substrate and the microsphere, as the SAWs propagate along the sample surface indexed by j.

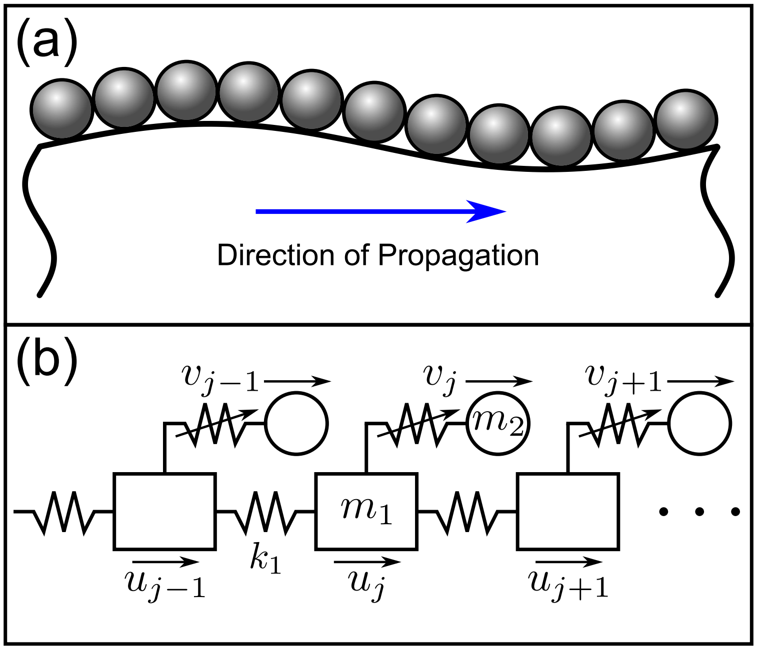

Figure 3.1: (a) Granular metamaterial composed of a monolayer of microspheres on an elastic halfspace. (b) Schematic of the 1D, discrete granular metamaterial model.

3.2.2 Hamiltonian 1D Discrete Model

In dimensionless form, the associated Hamiltonian equations of motion of the system shown in Fig. 3.1(b) read

$$\begin{aligned} M\ddot{u}_j + K\left(-u_{j+1} + 2u_j - u_{j-1}\right) & \\ + \frac{2}{3}\left([u_j - v_j + 1]_+^{3/2} - 1\right) &= 0 \qquad (3.1) \\ \ddot{v}_j - \frac{2}{3}\left([u_j - v_j + 1]_+^{3/2} - 1\right) &= 0, \qquad (3.2) \end{aligned}$$

where u_j and v_j are, respectively, the displacements from equilibrium of the main chain and resonators; $M = \frac{m_1}{m_2}$; $K = \frac{k_1}{(3/2)A\sqrt{\delta_0}}$ characterizes the relative strength of the elastic and

Hertzian terms, where the Hertzian coefficient A depends on the geometry and material properties of the particles in contact [11]; and δ_0 is the static overlap induced by the adhesive force at equilibrium. The dimensionless time variable τ is defined in terms of the physical time t by $\tau = \omega_0^{hs} t$, where $\omega_0^{hs} = \sqrt{(3/2)A\sqrt{\delta_0}/m_2}$ is the resonant frequency of the local oscillator on the elastic halfspace (measured as 215 MHz for the system in Ref. [8]), and the displacements u_j and v_j are normalized to δ_0. The subscript $[\ \ ]_+$ indicates that the contact force vanishes for resonators that lose contact with the main chain, i.e. when the relative displacement $v_j - u_j$ exceeds the static overlap. The Hamiltonian (energy) corresponding to Eqs. (3.1) and (3.2) is

$$\begin{aligned} H = \quad & \sum_j \left[M\frac{\dot{u_j}^2}{2} + \frac{\dot{v_j}^2}{2} + \frac{K}{2}(u_{j+1}^2 - 2u_{j+1}u_j + u_j^2) + \right. \\ & \left. \frac{2}{3}\left(\frac{2}{5}[u_j - v_j + 1]_+^{5/2} - (u_j - v_j)\right) - \frac{4}{15}\right]. \end{aligned} \tag{3.3}$$

Upon linearization, this system is identical to the one-dimensional mass-in-mass chain discussed in [96]. Its dispersion relation is given by

$$\begin{aligned} M\left(\frac{\omega}{\omega_0^{hs}}\right)^4 \quad & -[2K(1-\cos(kD)) + M + 1]\left(\frac{\omega}{\omega_0^{hs}}\right)^2 \\ & +2K(1-\cos(kD)) = 0, \end{aligned} \tag{3.4}$$

where k is the Bloch wave number, ω is the angular frequency, and D is the unit cell width, defined as the width of the granular particles.

3.2.3 Parameter Fitting

The resulting model, Eqs. (3.1)-(3.2), possesses two effective lumped parameters, namely M and K. We now attempt to fit these discrete model parameters to describe the microgranular metamaterial of Ref. [8], using the material and geometric properties specified therein. We intend for the discrete model to provide an adequate representation of dynamical evolution for wavelengths significantly larger than the sphere diameter, such that the dispersion relations for our discrete model and the model with a continuous substrate from Ref. [8] are in close agreement at long wavelengths, and effects found at the Brillouin zone boundary [17] are avoided [96]. The dispersion relations for a continuous substrate (from Eq. (2) of Ref. [8]) and the discrete model of Eqs. (3.1) and (3.2) are superimposed in Fig. 3.2. We first choose the ratio K/M such that the long-wavelength sound speed of the discrete lattice, given by $D\sqrt{K/M}$ [17], matches the speed of Rayleigh waves in the substrate for the model from Ref. [8]. This can be seen graphically in Fig. 3.2, as the lower branches of the two dispersion relations have equal slopes at the origin. Second, making use of the analytical expression for the dispersion relation of the continuous system in Ref. [8], we select K, such that the dispersion relations coincide at the intersection with the line of slope c_T, where c_T is the transverse sound speed of the substrate material. Using these two criteria, we find the approximate fitted values $M = 30$ and $K = 160$.

The physical significance of these parameter values, M and K, is as follows. For large mass ratios ($M >> 1$), waves in the main chain (corresponding to Rayleigh SAWs in the substrate) are only perturbed at frequencies very close to the local resonance; this is confirmed in Fig. 3.2, by the relatively narrow band gap encompassing $\omega/\omega_0^{hs} = 1$. The large stiffness ratio ($K >> 1$) indicates strong coupling between lattice sites, compared to the coupling between the main chain and the resonators. Intuitively, parameters much greater than unity are indeed expected for this system. This is because the spheres are much smaller and less massive than the region of the substrate beneath them that is influenced by Rayleigh waves, which have displacements decaying exponentially from the surface with a characteristic decay length on the order of one wavelength [93]. Similarly, the effective stiffness for the region of bulk material of the substrate influenced by the Rayleigh wave can be thought to have a significantly greater effective stiffness than the relatively soft microsphere-substrate Hertzian contact. While the fitted constants depend on material and geometric properties, a simple estimate can be used to show that M and K are generally larger than unity when considering long waves in realistic materials, as described in Appendices A and B of Ref. [94].

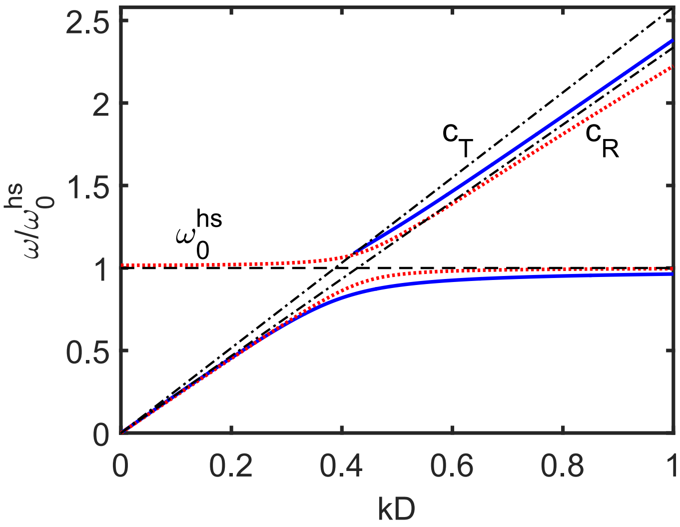

Figure 3.2: Blue solid and red dotted curves denote the dispersion relations for the model with a continuous substrate from Ref. [8] and our discrete granular metamaterial model, respectively. Black dash-dotted lines have slopes equal to the transverse (c_T) and Rayleigh (c_R) wave sound speeds of the substrate. The black dashed line denotes the linear natural frequency of the Hertzian local resonators. The discrete model uses the fitted parameters $M = 30$ and $K = 160$.

Both of the dispersion relations shown in Fig. 3.2 are split, as a result of the hybridization with the local resonance, into two branches: the lower ("acoustic") branch, in which the vertical motions of the substrate surface and the spheres are in phase, and the upper ("optical") branch, in which the motions are out of phase. The two branches of the discrete model are separated by a band gap of width $\Delta\omega$, given by

$$\begin{aligned}\Delta\omega &= \omega_0^{hs}\left(\sqrt{\frac{1+M}{M}}\right.\\ &\left.-\sqrt{\frac{4K+M+1-\sqrt{(4K+M+1)^2-16KM}}{2M}}\right).\end{aligned} \tag{3.5}$$

For the parameters values M and K used herein, this band gap results in an upper cutoff frequency of the acoustic branch 0.08% below ω_0^{hs} and a lower cutoff frequency of the optical branch 1.65% above ω_0^{hs}. In the continuous model, for phase velocities greater than the sound speed of transverse bulk waves (c_T) in the substrate, the optical branch terminates; this is because the modes above that phase velocity are so-called “leaky modes.” Such leaky modes have complex frequency, which represents the radiation of energy into the bulk [8, 125, 126], and are a major source of dissipation in this system. Despite the presence of leaky modes, the one-dimensional, discrete model used in this work was chosen over continuous and/or higher-dimensional models because it captures many of the important features of the dispersion relation (linear dispersion at long wavelengths and a band gap created by a local resonance), facilitates theoretical prediction and numerical computation of discrete breathers, and can easily be adapted to account for dissipation in a chosen experimental system (as will be demonstrated in Sec. 3.4).

3.3 Numerical Investigation of Breathers

Using the fitted parameter values $M = 30$ and $K = 160$, we compute exact breather profiles[2] of a chain with 201 unit cells, and vary the breather frequency $\tilde{\omega}_b$ using a pseudo-arclength continuation procedure [129, 130]. This allows us to visualize the frequency-energy dependence of the breathers, as may be studied in an experiment with varied excitation amplitude. As a seed for the continuation, we use the eigenmode of the linearized system nearest the lowest optical band edge, which is a time-periodic solution of the full nonlinear equations of motion under conditions of vanishing amplitude. We have included a check in our computations to detect a loss of contact between the main chain and resonators, and continue the solution branch until this point.

As shown in Fig. 3.3, the continuation reveals a family of DBs that extends from the linear eigenmode at vanishing amplitude and traverses the band gap (and into the passband). In Fig. 3.4(a), we show the maximum magnitudes of the Floquet multipliers of the branch. This family of DBs exhibits behavior similar to that found in previous studies of diatomic granular chains [114], where the DBs are linearly stable for frequencies very close to the lower cutoff frequency of the optical branch. As the frequency decreases, the breather profiles become progressively more localized in space, as can be seen in Fig. 3.3(b-d). The Floquet multipliers corresponding to the modes shown in Fig. 3.3(b-d) are shown in Fig. 3.4(b-d), with small deviations from the unit circle emphasized in the latter panel. For breather frequencies below the band gap, interactions with the acoustic band generate oscillating tails, as is shown in Fig. 3.3(e), and Floquet multipliers depart from the unit circle along the real axis, as shown in Fig. 3.4(e). We note that boundary effects are significant in the presence of oscillating tails, so the finite-length DBs do not accurately approximate the case of an infinite lattice. As an aside, we also point out that contrary, e.g., to what is the case in the work of [114, 116] for a granular crystal, here the dependence of the energy (Hamiltonian) on the frequency is monotonic, hence in accordance with the recent criterion of [131], no instability arises from changes of monotonicity in this dependence.

---

[2] See also Ref. [94], in which we predict the existence of DBs in the extreme limits of vanishing and strong intersite coupling, and numerically compute a family of DBs connecting the two regimes.

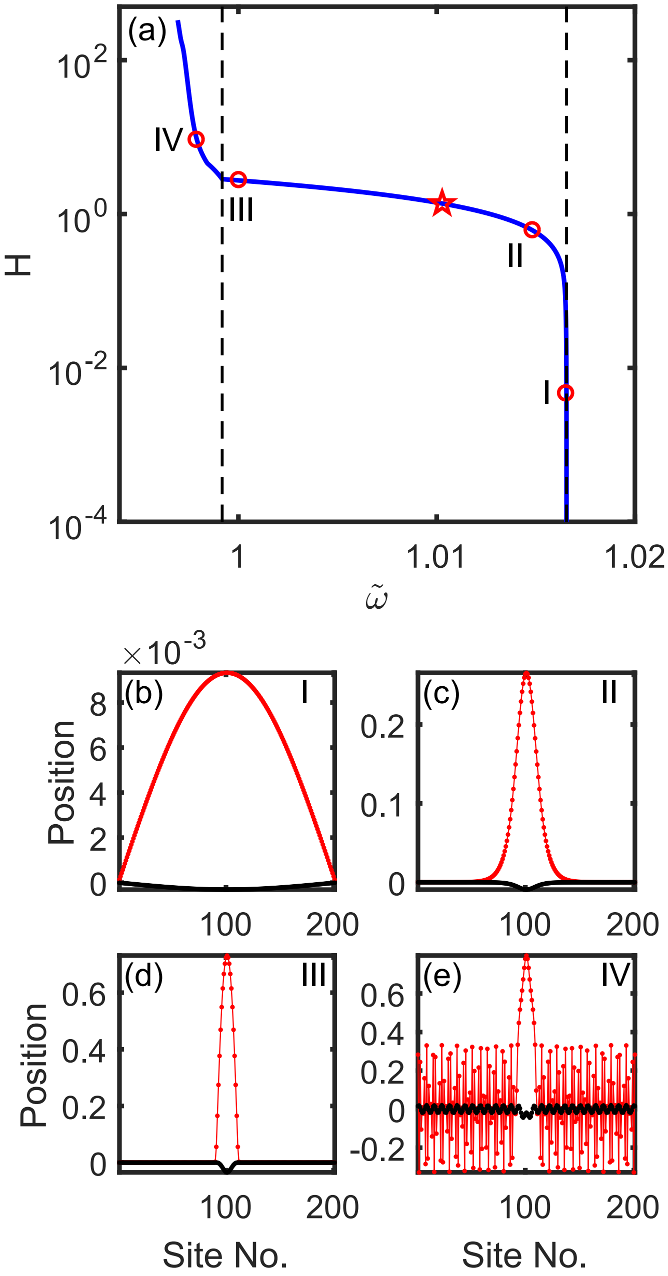

Figure 3.3: (a) Hamiltonian energy-frequency plot of the family of breather solutions bifurcating from the lowest eigenmode of the optical band. Black dashed lines indicate the edges of the linear phonon band gap. Red star corresponds to a breather shown in Fig. 3(b) of Ref. [94], which was computed during a continuation in coupling stiffness, K. (b) - (e) Breather displacement profiles corresponding to the points labeled I - IV, respectively, in (a). The main chain displacements u_j are shown as black points, and those of the local resonators v_j are shown in red.

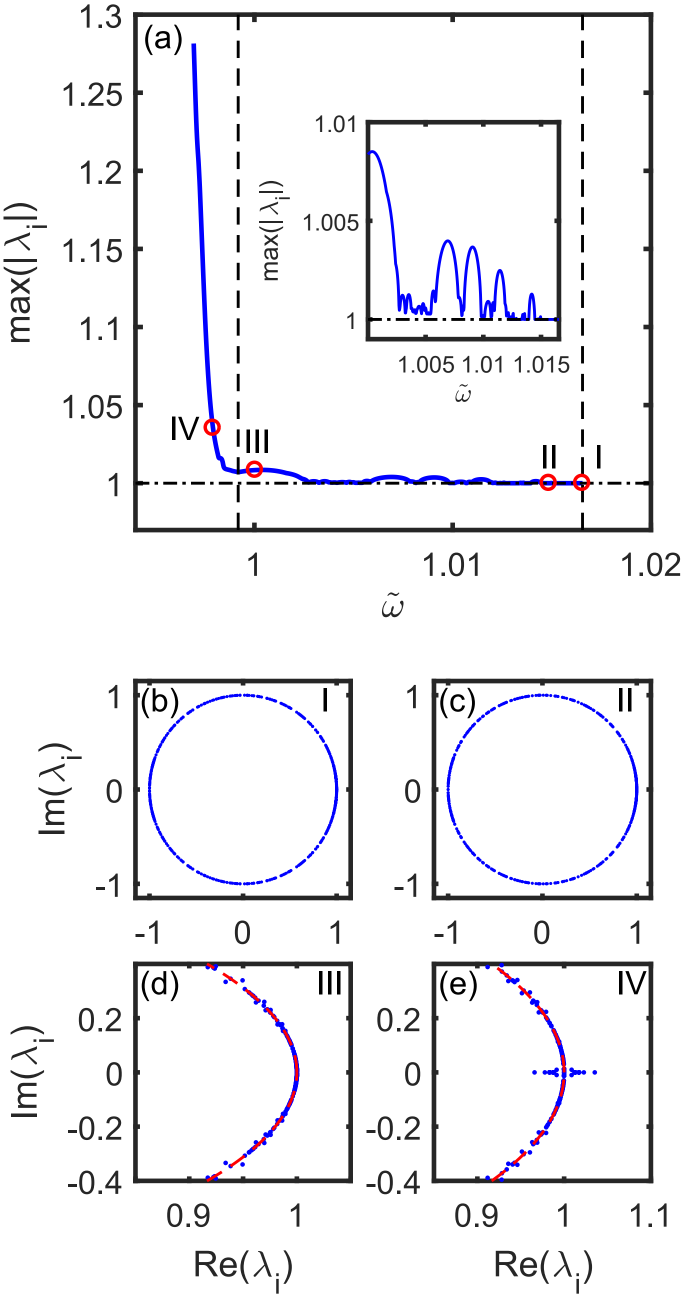

Figure 3.4: (a) The blue solid curve shows the maximum magnitude of the breather Floquet multipliers. Black dashed lines indicate the edges of the linear phonon band gap, and the inset shows a magnified view of the data in this range. (b)-(e) Floquet multipliers (blue dots) of the solutions labeled *I* - *IV*, respectively, in (a), corresponding to the same points in Fig. 3.3. In (d) and (e), axes limits are chosen to emphasize the deviation from the unit circle, which is shown as a visual aid (red dashed lines).

3.4 Numerical Simulations

3.4.1 Hamiltonian Case

To explore the dynamics of DBs in our model, we simulate a lattice with 201 unit cells via direct numerical integration of the equations of motion[3] given by Eqs. (3.1) and (3.2). We consider initial conditions in two shapes: the profile of the DB with frequency $\tilde{\omega}_b = 1.01$ and maximum Floquet multiplier magnitude $\max(|\lambda_i|) = 1.001$ (as is denoted by the star in Fig. 3.3(a)), as well as the profile of the seeding eigenmode used in Sec. 3.3. B.

For each of these shapes, we scale the amplitude in two ways. In the case of the DB shape, we consider the exact breather shape computed via continuation (high), and then consider a rescaled DB shape, such that the initial displacement v_{101} of the local resonator at the central lattice site is equal to one-hundredth of that of the exact solution (low). Similarly, we consider the shape of the seeding eigenmode scaled such that the initial displacement v_{101} of the local resonator at the central lattice site is matched to the low-amplitude, rescaled DB shape (low), and then finally consider a rescaled eigenmode shape, such that the initial displacement v_{101} of the local resonator at the central lattice site is equal to that of the exact DB solution (high). Thus, there are four sets of initial conditions: the DB shape with high amplitude (Fig. 3.5(d)), which results in an exact periodic solution of Eqs. (3.1) and (3.2); the eigenmode shape with low amplitude (Fig. 3.5(a)), which closely approximates a periodic solution; the DB shape rescaled to low amplitude (Fig. 3.5(b)), which is not a true periodic solution; and the eigenmode shape rescaled to high amplitude (Fig. 3.5(c)), which also is not a periodic solution. The duration of all simulations is $200T_b$, where $T_b = 2\pi/\tilde{\omega}_b$ is the period of the exact DB solution.

Spatiotemporal plots of the relative displacements $v_j - u_j$ of the simulated lattice, using the low and high amplitude DB profiles as initial conditions (i.e. the rescaled DB and exact solution) are shown in Fig. 3.5(b) and Fig. 3.5(d), respectively, and the corresponding cases using the eigenmode shape (i.e. the approximate periodic solution and corresponding rescaled profile) are shown in Fig. 3.5(a) and Fig. 3.5(c).

---

[3] 4th-order Runge-Kutta method. See Appendix B for details.

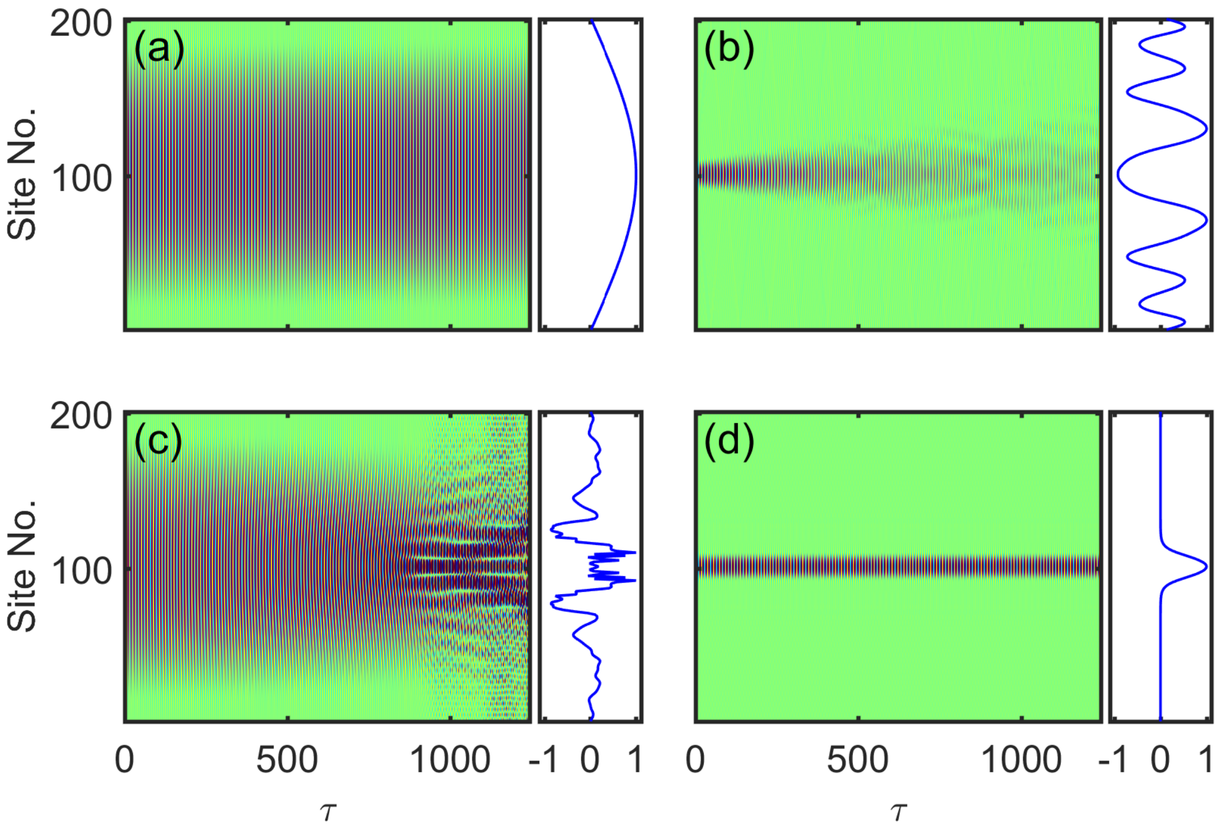

Figure 3.5: Spatiotemporal plots of the relative displacements $v_j - u_j$ of the simulated lattice for high and low amplitude excitations, using eigenmode and DB profiles as initial shapes. Side panels contain spatial profiles of $v_j - u_j$ at the final time step, normalized to the maximum value. (a) Eigenmode shape with low amplitude (approximate periodic solution). (b) DB shape rescaled to low amplitude. (c) Eigenmode shape rescaled to high amplitude. (d) DB shape with high amplitude (exact periodic solution).

As shown in the right column of Fig. 3.5, the breather shape spreads out from the central lattice sites at low amplitude, but remains highly localized when initiated with the energy of the exact solution. Conversely, as shown in the left column of Fig. 3.5, the eigenmode shape shows no noticeable distortion at low amplitude, but self-localizes and eventually breaks up at high amplitude. In this break-up, many smaller DBs are formed, a process arguably reminiscent of multiple filamentation in nonlinear optics [132], which also move in space. Thus, in future experiments on this system (e.g. using photoacoustic techniques, as in [8]), DBs could be detected by impulsively exciting a large spot on the substrate surface, and observing the formation of smaller, highly localized wave packets.

3.4.2 Effects of Energy Leakage

While we have considered a Hamiltonian model in this work as a foundation, energy losses may play an important role in the dynamics. The effects of losses have previously been examined in macroscopic granular systems [5, 14, 117, 133, 134], and also in the study of the attenuation of Rayleigh waves by randomly distributed surface resonators [57, 126]. In this section, we conduct a preliminary study of energy losses on the DB dynamics, focusing on losses caused by radiation of energy into the bulk of the material, which is incurred by the long wavelength "leaky modes" satisfying $\omega > kc_T$ considered in previous sections. We first estimate the strength of dissipation by considering the rate of energy leakage into the substrate in the system studied in Ref. [8], in the long wavelength limit. For a plane wave with real wave number k and complex frequency $\omega + i\eta$, the amplitude decays in time proportionally to $e^{-\eta t}$; thus, the rate of decay is found by solving the dispersion relation for this complex frequency, with wavenumber $k = 0$. The dispersion relation (reproduced from Ref. [8] and substituting our own variable names) is given by

$$\left(\frac{\omega^2}{{\omega_0^{hs}}^2}-1\right)\left[\left(2-\frac{\omega^2}{k^2c_T^2}\right)^2-4\left(1-\frac{\omega^2}{k^2c_L^2}\right)^{1/2}\left(1-\frac{\omega^2}{k^2c_T^2}\right)^{1/2}\right]=\frac{m_2}{A_c\rho_1}\frac{\omega^4\left(1-\frac{\omega^2}{k^2c_L^2}\right)^{1/2}}{k^3c_T^4}, \tag{3.6}$$

where m_2 and ω_0^{hs} are the mass and undamped natural frequency of the local resonator, respectively; $A_c = \sqrt{3}/2D^2$ is the area of a unit cell containing a single microsphere of diameter D; ρ_1 is the density of the substrate; and c_L and c_T are the longitudinal and transverse bulk sound speeds of the substrate, respectively. We find a decay rate at $k = 0$ of $\eta_0 = m_2{\omega_0^{hs}}^2/(2A_c\rho_1 c_L)$. To facilitate comparison of the decay rate with other systems, we define the normalized decay rate $\tilde{\eta} = 2\pi\eta/\omega$, where $1/\tilde{\eta}$ can be interpreted as the number of oscillation cycles needed to reduce the amplitude by a factor of e (at some characteristic frequency ω). For the material and geometric properties considered in this work, we estimate the normalized decay rate to be $\tilde{\eta}_0 = 2\pi\eta_0/\omega_0^{hs} \approx 0.4$.

Effects related to disorder, which have been discussed [8] and studied [57, 126] in prior works on interactions between Rayleigh waves and surface oscillators, are also a major potential source of loss; however, in this study, we consider a highly ordered system. In addition to radiative and disorder-related sources of loss, other types of dissipation will be present, but we expect them to be relatively small. For example, acoustic absorption in glass is about 0.5 dB/cm at frequencies near 200 MHz and room temperature [135]; assuming a Rayleigh wave with frequency ω_0^{hs} and velocity of 3409 m/s [8], this results in $\tilde{\eta} = 9^{*}10^{-5}$. Aerodynamic drag in air (modeled by Stokes' Law, assuming 1 μm diameter spheres [136]) results in $\tilde{\eta} = 3^{*}10^{-4}$. Finally, plastic deformation due to contact forces, if present (e.g. from fabrication or high-amplitude vibrations, etc.), will not cause significant hysteresis because subsequent loading-unloading cycles will be elastic.

To account for energy losses, in a way that is consistent with radiation into the bulk in the continuous granular metamaterial model, we modify our conservative system of Eqs. (3.1)-(3.2) by placing a linear damper in each local resonator (as is shown in Fig. 3.6) with a damping coefficient defined as $\Gamma = \tilde{\eta}/\pi$, such that the exponential decay in time is proportional to $e^{-\tilde{\eta}/(2\pi)\tau}$ and $\Gamma_0 = \tilde{\eta}_0/\pi$. With the damping included, the equations of motion become

$$\begin{aligned} M\ddot{u}_j &+ K\left(-u_{j+1} + 2u_j - u_{j-1}\right) \\ &\quad + \frac{2}{3}\left([u_j - v_j + 1]_+^{3/2} - 1\right) + \Gamma(\dot{u}_j - \dot{v}_j) = 0 \end{aligned} \tag{3.7}$$

$$\ddot{v}_j - \frac{2}{3}\left([u_j - v_j + 1]_+^{3/2} - 1\right) - \Gamma(\dot{u}_j - \dot{v}_j) = 0. \tag{3.8}$$

Using Eqs. (3.7)-(3.8), we repeat simulations of the 201-cell mass-in-mass chain, using the high-amplitude eigenmode and exact DB shapes (as in Fig. 3.5(c, d)) as initial conditions. The case $\Gamma = \Gamma_0$ is shown in Fig. 3.7(a, b), where it can be seen that the oscillations die out after only a few oscillation cycles; this estimate indicates that the leakage of energy into the substrate may prohibit the observation of a standing localized mode in experiments on the particular system of Ref. [8], without adding additional energy into the system to support the DB structure. However, this does not necessarily prohibit localized structures stemming from non-leaky modes. In this system, this corresponds to wavenumber-frequency pairs below the line with slope c_T in Fig. 3.2. Such solutions would be traveling breathers, and can be easily obtained from the theoretical analysis performed in Ref. [94][4]. A detailed investigation of such solutions would be a topic for future study.

---

[4] Specifically, by choosing a non-zero wavenumber in Eq. (16) of Sec. III B.

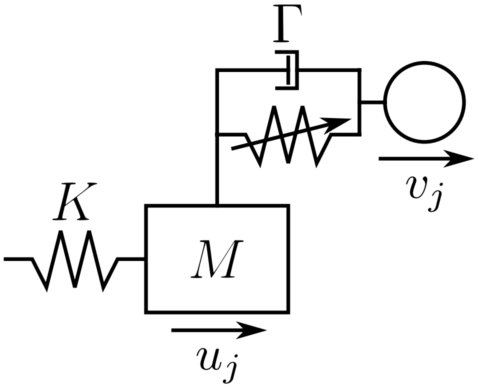

Figure 3.6: Schematic of a single unit cell of the damped mass-in-mass lattice, with dimensionless parameters.

In addition, while the attenuation due to energy leakage is significant for the monolayer of Ref. [8], it is straightforward to modify the system to reduce these losses by orders of magnitude; for example, if the spheres were instead placed with a spacing of $10D$, the unit cell area A_c would increase by a factor of 100, causing a proportional reduction in the damping coefficient Γ. As shown in Fig. 3.7(g, h), for the case $\Gamma = \Gamma_0/100$, the dynamics of the Hamiltonian model are retained for roughly half the simulation time (on the order of one hundred oscillations), and localization around the central lattice site persists. Two intermediate cases are shown in Fig. 3.7(c, d) and Fig. 3.7(e, f), corresponding to damping coefficients $\Gamma = \Gamma_0/4$ (sphere spacing $2D$) and $\Gamma = \Gamma_0/16$ (sphere spacing $4D$), respectively. Very light damping could also be achieved in systems with different geometries, such as a thin substrate (e.g. the locally-resonant membrane of Ref. [55]) without altering the unit cell spacing, because energy would not be able to radiate. Additionally, we note that light damping (specifically, attenuation rates one order of magnitude smaller than Ref. [8]) has already been achieved experimentally in macroscale granular crystals. For example, both Ref. [14] and Ref. [117] characterized dissipation in experiments and found time constants on the order of a few milliseconds, at frequencies near 5 kHz, resulting in $\tilde{\eta} \approx 0.08$ and $\tilde{\eta} \approx 0.04$, respectively, which suggests possible future realizations of our model at the macroscale.

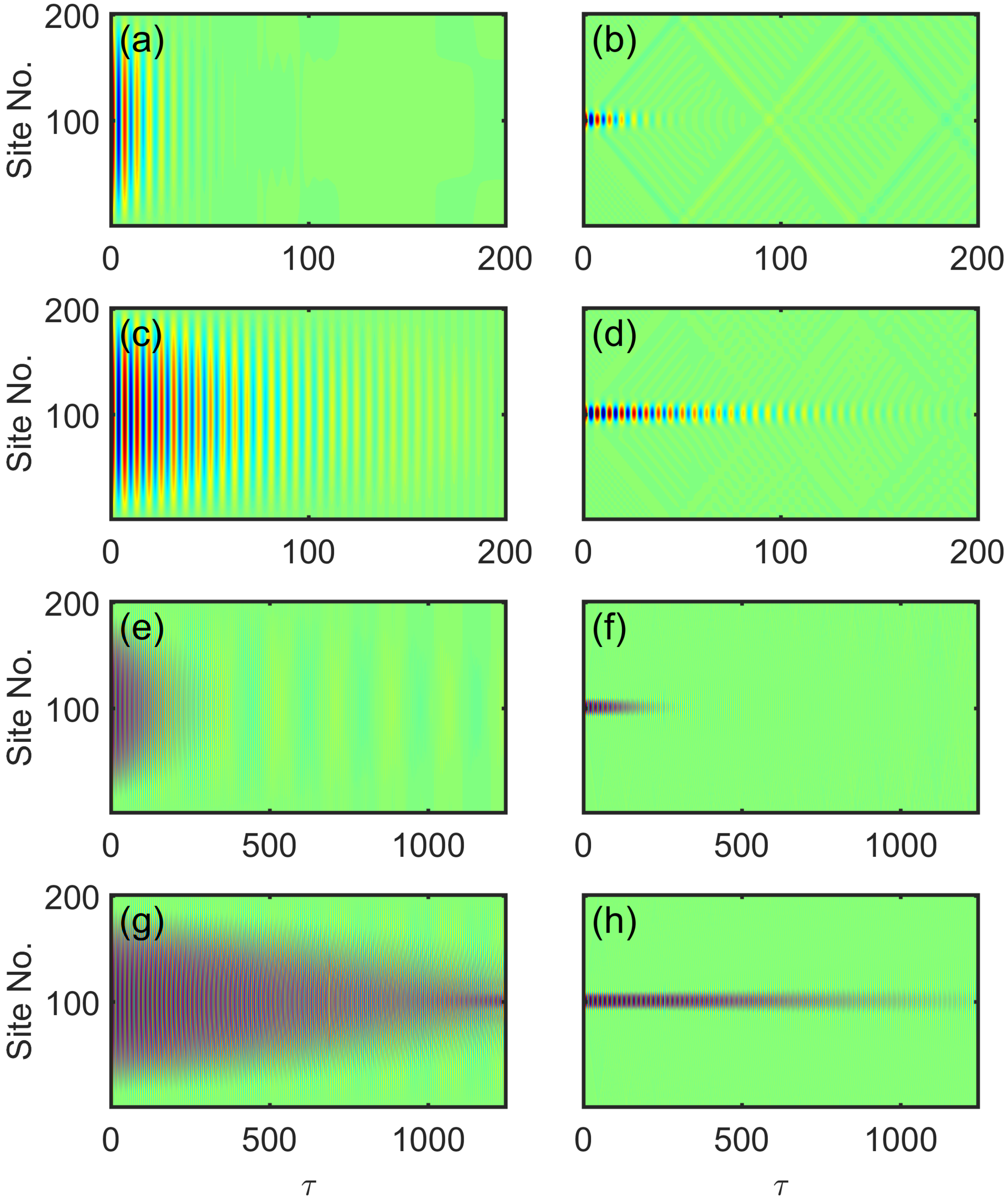

Figure 3.7: Spatiotemporal plots of the relative displacements $v_j - u_j$ of the simulated lattice for several damping coefficients: (a, b) $\Gamma = \Gamma_0$, (c, d) $\Gamma = \Gamma_0/4$, (e, f) $\Gamma = \Gamma_0/16$, and (g, h) $\Gamma = \Gamma_0/100$. Left and right panels correspond to the eigenmode (rescaled to high amplitude) and DB excitations used in Fig. 3.5(c, d).

3.5 Conclusion

In this chapter, we have demonstrated the existence of discrete breathers in a mass-in-mass chain that models a locally resonant, granular metamaterial composed of microsphere arrays adhered to a substrate. This work built upon previous models of microsphere arrays adhered to substrates (as described in Ch. 2 and Refs. [8, 55]), but includes nonlinear and damping effects in the particle-substrate contact. This model consists of a linearly-coupled main chain (representing the substrate) with nonlinear local resonators that follow the Hertzian contact law (representing the spheres). After fitting the two independent model parameters to a microscale system studied in previous works, we numerically analyze the resulting energy trapping in the Hamiltonian version of our model, in the form of discrete breathers, by using the oscillation frequency as a continuation parameter. Finally, we simulate the formation and filamentation–in the form of discrete breathers–of single-humped wavepackets using direct numerical integration of the equations of motion. The simulations suggest that discrete breathers may be observed in experiments on granular metamaterials by generating a long-wavelength excitation at high amplitude, and detecting its breakup into many small discrete breathers. Simulations including energy losses suggest that the dynamics of the Hamiltonian model are mostly preserved in cases with light damping. However, in cases where the substrate is very thick, energy losses due to radiation into the bulk may inhibit the experimental observation of discrete breathers, though the leakage may be mitigated significantly by choosing suitable system parameters (e.g. the unit cell spacing, in the specific system discussed above). We expect this work to aid in future studies of nonlinear granular systems, as well as to the more general class of media composed of a linear material with local nonlinear resonant attachments. Indeed, the dynamics and interactions of discrete breathers (as well as their potential filamentation and dispersion) in one- to three-dimensional analogs of such systems, may yield numerous topics that could be both theoretically intriguing, as well as experimentally accessible for further study. Also, it should be borne in mind that here we only explored the focusing variants of the relevant models and their bright solitons. Yet, in line with recent explorations in granular crystals [117] and in systems with resonators [105], the self-defocusing case may also be interesting and equally accessible in different parametric regimes.

Chapter 4

DYNAMICS OF A MONOLAYER OF MICROSPHERES ON AN ELASTIC SUBSTRATE[1]

We present a model for wave propagation in a monolayer of spheres on an elastic substrate, which builds upon the work of Ref. [8] and Ch. 2. The model, which considers sagittally polarized waves, includes: horizontal, vertical, and rotational degrees of freedom; normal and shear coupling between the spheres and substrate, as well as between adjacent spheres; and the effects of wave propagation in the elastic substrate. For a monolayer of interacting spheres, we find three contact resonances whose frequencies are given by simple closed-form expressions. For a monolayer of isolated spheres, only two resonances are present. The contact resonances couple to surface acoustic waves in the substrate, leading to mode hybridization and "avoided crossing" phenomena. We present dispersion curves for a monolayer of silica microspheres on a silica substrate, assuming adhesive Hertzian interactions, and compare calculations using an effective medium approximation (including elasticity of the substrate) to a discrete model of a monolayer on a rigid substrate. While the effective medium model does not describe discrete lattice effects occurring at short wavelengths, we find that it is well suited for describing the interaction between the monolayer and substrate in the long wavelength limit. We suggest that a complete picture of the dynamics of a monolayer adhered to an elastic substrate can be found by combining the dispersion curves generated from the effective medium model for the elastic substrate and the discrete model for the rigid substrate. This model is potentially scalable for use with nano- to macroscale systems, and offers the prospect of experimentally extracting contact stiffnesses from measurements of acoustic dispersion.

---

[1] The work in this chapter is adapted from Ref. [137]. Copyright 2015 by the American Physical Society.

4.1 Introduction

Experimental configurations used to study mechanical wave propagation in ordered granular media typically involve spherical particles confined by elastic media. This type of arrangement is particularly common in one- and two-dimensional configurations, and includes macro- to microscale particles. For example, at the macroscale, elastic rod structures, tracks, and tubes have been used to confine the particles in one-dimensional [138, 139, 140, 141, 142] and quasi-one-dimensional [143, 144, 145] configurations, and elastic plates have been used in two dimensions [146, 147]. More recently, the dynamics of two-dimensional monolayers of microscale spheres adhered to elastic substrates have been studied using laser ultrasonic techniques [8, 55, 57].

As shown in Ch. 2, analytical models used to describe the dynamics of these systems typically only include the interaction between the particles (often just the normal Hertzian contact interaction) and disregard the effect of the substrate. In reality, even for the simple case of a particle monolayer on a substrate, more complex dynamics involving interactions between the particles and elastic waves in the substrate should be expected.

A notable theoretical work [148] provided a model for the dynamics of crystals with adsorbed monolayers that accounted for both normal and horizontal motion and interaction between the particles, but did not take into account particle rotation. Several recent studies have demonstrated, in both theoretical [28, 29] and experimental [27] contexts, that the rotational degree of freedom has a profound effect on the dynamics of ordered granular media. In particular, the study of Ref. [28] focused on the dynamics of granular monolayers (whereas Refs. [27, 29] explored bulk granular structures), including cases involving interaction between the monolayer and a substrate. However, Ref. [28] only considered normal contact interactions between the particles and the substrate, and the substrate was modeled as rigid.

The aim of this chapter is to provide a theoretical model for the contact-based dynamics of a two-dimensional layer of spheres on a substrate, accounting for the elasticity of the substrate, translational and rotational motion of the spheres, and both normal and shear stiffnesses of sphere-to-sphere and sphere-substrate contacts. This extends prior work on systems with uncoupled oscillators as described in Chapters 2 and 3, and Refs. [8, 55]. We focus on a system with microscale particles that interact with each other and with the substrate via van der Waals adhesion forces. Rather than postulate the contact stiffness constants, we derive them from Hertzian contact models. This imposes certain constraints on the values of the constants: for example, the ratio of the normal and shear contact stiffness between the spheres is a constant only weakly dependent on Poissons ratio. We consider contact-based modes having frequencies significantly below the intrinsic spheroidal vibrational modes of the spheres, such that they can be described as spring-mass oscillators. Furthermore, we focus on dynamics involving particle and substrate displacements in the sagittal plane, as would be detectable in a laser-based experiment [8].

We start with the case of a rigid substrate, where we find three eigenmodes involving vertical, horizontal and rotational motion of the spheres. In the long-wavelength limit these modes yield three contact resonances, for which simple analytical expressions are obtained. One of the resonances involves motion of the spheres normal to the substrate surface, whereas the other two involve mixed horizontal-rotational motion. We then present our effective medium model, which describes the interaction between the spheres and the substrate, and show hybridization between the contact resonances and Rayleigh surface waves. We discuss cases involving both isolated (non-touching) and interacting spheres, and demonstrate the important role of rotations in both cases. We also examine the validity of the effective medium approximation, by comparing calculations using discrete and effective medium models. Finally, we discuss the implications of our findings for past and future studies of granular monolayer systems.

4.2 Model

We consider a monolayer of elastic spheres on a substrate, which can be either close-packed and in contact, or isolated, as shown in Fig. 4.1(a). In either case, the spheres are assumed to form a square lattice, with the wave propagation direction aligned with the lattice vector, as

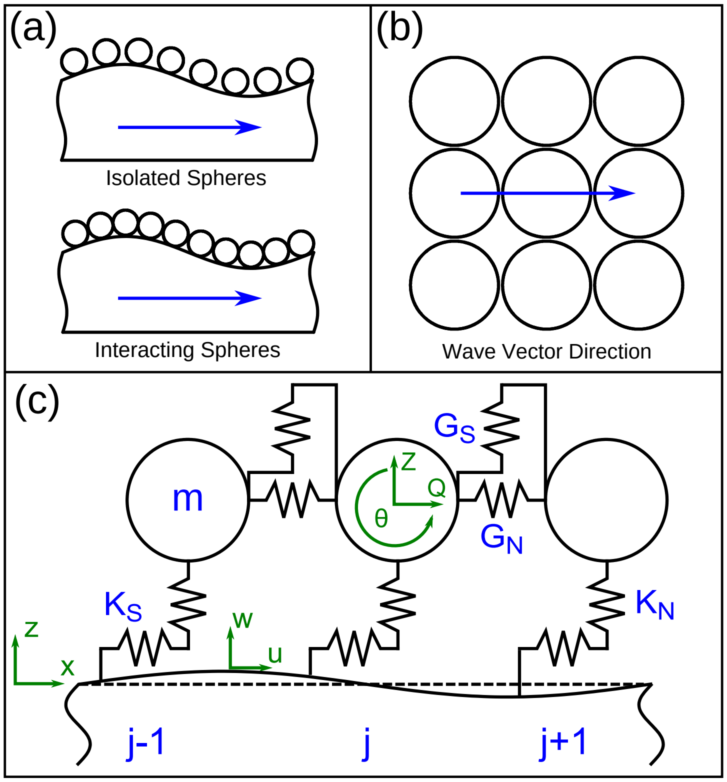

Figure 4.1: (a) Side-view schematic of an amplified wave profile for cases with isolated and interacting spheres. (b) Top-down view of the square-packed monolayer, with the arrow indicating the direction of wave propagation. (c) Schematic for the model of a monolayer of spheres coupled to an elastic halfspace.

shown in Fig. 4.1(b). We model the layer as an infinite lattice of rigid spheres with diameter $D = 2R$ and mass m, coupled to a semi-infinite, isotropic elastic substrate by normal and shear stiffnesses K_N and K_S, and to nearest-neighbor spheres by stiffnesses G_N and G_S, as schematically shown in Fig. 4.1(c). The subscript N corresponds to forces acting normal to the surface of the sphere, and S to forces acting transverse to the surface of the sphere. The shear springs generate an associated torque about the sphere center, while the normal springs do not. The absolute horizontal, vertical, and angular displacements of sphere j from its equilibrium state are given by Q_j, Z_j, and θ_j, respectively, and the displacements of the substrate are denoted by $u(x, z)$, corresponding to displacement in the x-direction, and $w(x, z)$, corresponding to displacements in the z-direction.

4.2.1 Contact Stiffness

We derive the stiffnesses K_N, K_S, G_N, and G_S using Derjaguin-Muller-Toporov (DMT) [3, 47] and Mindlin contact models [12]. The DMT theory is typically applicable in weakly-adhesive systems with small, stiff particles [149], and assumes that the deformation profile is Hertzian. The Mindlin model describes the shear stiffness of particles in contact, assuming an applied normal force [12]. At the microscale, adhesive contact mechanics has been studied using atomic force microscopy and nanoindentation approaches [150].

For contact between two spheres (or a sphere and a halfspace) having elastic moduli E_1 and E_2, and Poisson's ratios ν_1 and ν_2, the Hertzian restoring elastic force F_N corresponding to displacement δ_N of the particle center in the direction normal to the contact surface is given by

$$F_N = \frac{4}{3} E^* R_c^{1/2} \delta_N^{3/2}, \tag{4.1}$$

where R_c is the effective radius (equal to R for sphere-halfspace contacts and $R/2$ for sphere-sphere contacts), and $E^* = [(1-\nu_1^2)/E_1 + (1-\nu_2^2)/E_2]^{-1}$ is the effective modulus. Considering the DMT adhesive force $F_{DMT} = 2\pi w R_c$ acting normal to the contact surface [3, 47] (where

w is the work of adhesion between two surfaces), the net normal force is given by

$$F_{N,net} = F_N - F_{DMT}. \tag{4.2}$$

To describe the shear contact, we utilize the Mindlin model [12], which assumes small relative displacements and no slip at the contact surface. For two elastic bodies with shear moduli G_1 and G_2, the restoring elastic force F_S to displacement δ_S of the particle center in the direction transverse to the contact normal is given by

$$F_S = 8G^* R_c^{1/2} \delta_S \delta_N^{1/2}, \tag{4.3}$$

where $G^* = [(2-\nu_1)/G_1 + (2-\nu_2)/G_2]^{-1}$ is the effective shear modulus [12]. Here, the factor of $\delta_N^{1/2}$ arises from the Hertzian relation between the contact radius and F_N given by Eq. (4.1).

By substituting the relative displacements $\delta_N = Z - w_0$ and $\delta_S = Q - u_0 + R\theta$ (where $u_{0,j}$ and $w_{0,j}$ are horizontal and vertical displacements of the substrate surface at the point of contact, respectively) into Eqs. 4.2 and 4.3, and linearizing about the equilibrium configuration of $\delta_{N,0} = [3F_{DMT}/(4E^* R_c^{1/2})]^{2/3}$ and $\delta_{S,0} = 0$, we derive linearized normal and shear contact stiffnesses

$$\begin{aligned} K_N &= \left(6{E^*}^2 R_c F_{DMT}\right)^{1/3} \\ K_S &= 8\left(\frac{3}{4}\frac{{G^*}^3}{E^*} R_c F_{DMT}\right)^{1/3}. \end{aligned} \tag{4.4}$$

Stiffnesses G_N and G_S are given by equations of the same form as Eq. (4.4), but with E^*, G^*, R_c, and F_{DMT} adjusted for sphere-sphere contacts. In the special case where the spheres and substrate are composed of the same material, the relative magnitudes of the stiffness constants are determined exclusively by Poisson's ratio ν of the material,

$$\begin{aligned} G_N &= 2^{-2/3} K_N \\ K_S &= \nu^* K_N \\ G_S &= 2^{-2/3} \nu^* K_N, \end{aligned} \tag{4.5}$$

where $\nu^* = 2(1-\nu)/(2-\nu)$.

4.2.2 Equations of Motion of the Spheres

Assuming small displacements (i.e. Q_j, Z_j, and $R\theta_j$ are much less than D), the j^{th} sphere obeys the equations of motion

$$\begin{aligned} m\ddot{Q}_j &= -K_S(Q_j - u_{0,j} + R\theta_j) + G_N(Q_{j+1} - 2Q_j + Q_{j-1}) \\ m\ddot{Z}_j &= -K_N(Z_j - w_{0,j}) + G_S[Z_{j+1} - 2Z_j + Z_{j-1} - R(\theta_{j+1} - \theta_{j-1})] \\ I\ddot{\theta}_j &= -K_S R(Q_j - u_{0,j} + R\theta_j) - G_S R[R(\theta_{j+1} + 2\theta_j + \theta_{j-1}) - (Z_{j+1} - Z_{j-1})]. \end{aligned} \tag{4.6}$$

4.2.3 Effective Medium Approximation

Considering wavelengths much longer than the sphere diameter, we treat the monolayer as an effective continuous medium[2]. By substituting the center difference formulas $[(\cdot)_{j+1} - (\cdot)_{j-1}]/(2D) \approx \partial(\cdot)/\partial x$ and $[(\cdot)_{j+1} - 2(\cdot)_j + (\cdot)_{j-1}]/(D^2) \approx \partial^2(\cdot)/\partial x^2$ into Eq. (4.6), we arrive at the equations of motion of the monolayer in effective medium form:

$$\begin{aligned} m\frac{\partial^2 Q}{\partial t^2} &= -K_S(Q - u_0 + R\theta) + 4G_N R^2 \frac{\partial^2 Q}{\partial x^2} \\ m\frac{\partial^2 Z}{\partial t^2} &= -K_N(Z - w_0) + 4G_S R^2 \left(\frac{\partial^2 Z}{\partial x^2} - \frac{\partial \theta}{\partial x}\right) \\ I\frac{\partial^2 \theta}{\partial t^2} &= -K_S R(Q - u_0 + R\theta) - 4G_S R^2 \left(R^2 \frac{\partial^2 \theta}{\partial x^2} + \theta + \frac{\partial Z}{\partial x}\right). \end{aligned} \tag{4.7}$$

The coupling between the monolayer and substrate is defined by the following boundary conditions at the surface $z = 0$, which describe the average force acting on the surface due to the motion of the spheres:

$$\begin{aligned} \sigma_{zx} &= \frac{K_S}{A}(Q - u_0 + R\theta) \\ \sigma_{zz} &= \frac{K_N}{A}(Z - w_0), \end{aligned} \tag{4.8}$$

where σ_{zx} and σ_{zz} are components of the elastic stress tensor [93] and $A = D^2$ is the area of a primitive unit cell in our square-packed monolayer. The combination of Eq.

---

[2] See Sec. 4.4.2 (particularly Fig. 4.7) for a discussion of the range of validity of the effective medium.

(4.7) and the linear elastic wave equations describing waves in the substrate [93], coupled by the boundary conditions of Eq. (4.8), comprises the complete effective medium model.

4.3 Dispersion Relations

4.3.1 Rigid Substrate

Discrete Model

We calculate the dispersion relation for a monolayer on a rigid base using Eq. (4.6), by assuming spatially-discrete traveling wave solutions of the form $\hat{Q}e^{i(\omega t - kDj)}$ (with similar terms for the other displacements) and setting the displacements of the substrate surface $u_{0,j}$ and $w_{0,j}$ to zero. Here, $\hat{(\cdot)}$ is the amplitude of a plane wave in the displacement variable $(\cdot)$, ω is the angular frequency, and k is the wave number. After algebraic manipulation, Eq. (4.6) is reduced to a homogeneous system of three linear algebraic equations in terms of the amplitudes $\hat{(\cdot)}$. This system possesses non-trivial solutions only for pairs of k and ω that cause the determinant of the system to vanish. Enforcing this condition, we arrive at the following dispersion relation, where the three rows of the determinant correspond to the three equations of Eq. (4.6):

$$\begin{vmatrix} \frac{c_N^2}{2R^2}(1-\cos(kD)) + \phi_S\omega_S^2 & 0 & R\omega_S^2 \\ 0 & \frac{c_S^2}{2R^2}(1-\cos(kD)) + \phi_N\omega_N^2 & -\frac{c_S^2}{2R} i\sin(kD) \\ R\omega_S^2 & \frac{c_S^2}{2R} i\sin(kD) & \frac{I}{m}[\frac{c_\theta^2}{2R^2}(1-\cos(kD)) + \phi_\theta\omega_\theta^2] \end{vmatrix} = 0, \tag{4.9}$$

where $\phi_N = 1 - \omega^2/\omega_N^2$, $\phi_S = 1 - \omega^2/\omega_S^2$, $\phi_\theta = 1 - \omega^2/\omega_\theta^2$, $c_N = \sqrt{G_N/m}(2R)$ and $c_S = \sqrt{G_S/m}(2R)$ [151], $c_\theta^2 = -mR^2c_S^2/I$, $\omega_N^2 = K_N/m$, $\omega_S^2 = K_S/m$, and $\omega_\theta^2 = (K_S + 4G_S)R^2/I$.

Effective Medium

To obtain dispersion relations assuming an effective medium, we substitute spatially-continuous traveling wave solutions of the form $\hat{Q}e^{i(\omega t-kx)}$ (with similar terms for the other displacements) into Q, Z, and θ in Eq. (4.7) with $u_0 = w_0 = 0$. Following the same procedure used to obtain Eq. 4.9, we obtain

$$\begin{vmatrix} c_N^2k^2+\phi_S\omega_S^2 & 0 & R\omega_S^2 \\ 0 & c_S^2k^2+\phi_N\omega_N^2 & -ikc_S^2 \\ R\omega_S^2 & ikc_S^2 & \frac{I}{m}(c_\theta^2k^2+\phi_\theta\omega_\theta^2) \end{vmatrix} = 0. \tag{4.10}$$

It is particularly instructive to examine the behavior of the effective medium model in the long wavelength limit $k \to 0$. In this limit, the displacements vary slowly in space, and the spatial derivative terms of Eq. (4.7) may be neglected. For the case of a rigid base, Eq. (4.7) reduces to the form

$$\begin{aligned} m\frac{\partial^2 Q}{\partial t^2} &= -K_S(Q+R\theta) \\ m\frac{\partial^2 Z}{\partial t^2} &= -K_N Z \\ I\frac{\partial^2 \theta}{\partial t^2} &= -K_S R(Q+R\theta) - 4G_S R^2\theta. \end{aligned} \tag{4.11}$$

The equation for Z decouples from the other two equations and yields a vertical vibrational mode. The two other equations remain coupled, yielding two modes containing both horizontal and rotational motion. Using the moment of inertia of a solid sphere $I = (2/5)mR^2$, we find three resonance frequencies

$$\begin{aligned} \omega_N &= \left[\frac{K_N}{m}\right]^{1/2} \\ \omega_{RH} &= \left[\left(\frac{K_S}{4m}\right)\left(20\gamma+7+\sqrt{400\gamma^2+120\gamma+49}\right)\right]^{1/2} \\ \omega_{HR} &= \left[\left(\frac{K_S}{4m}\right)\left(20\gamma+7-\sqrt{400\gamma^2+120\gamma+49}\right)\right]^{1/2}. \end{aligned} \tag{4.12}$$

where $\gamma = G_S/K_S$. Here, ω_N corresponds to a mode with exclusively vertical motion. The other two modes ω_{RH} and ω_{HR} exhibit both rotational and horizontal (but not vertical) motion, with relative amplitudes determined by γ. The higher of the two horizontal-rotational modes is predominantly rotational and the lower is predominantly horizontal, hence we have used the notations ω_{RH} and ω_{HR}, where the first letter in the subscript denotes the dominant motion. If the spheres and substrate are made of the same material, then, by using Eq. (4.5), we can relate the horizontal-rotational frequencies of Eq. (4.12) to the vertical resonance frequency, with the expressions $\omega_{RH} = 3.018{\nu^*}^{1/2}\omega_N$ and $\omega_{HR} = 0.832{\nu^*}^{1/2}\omega_N$.

In the limiting case of isolated spheres ($\gamma = 0$), ω_{RH} and ω_{HR} of Eq. (4.12) become $\omega_{RH,Iso} = \sqrt{7/2}\omega_S$ and $\omega_{HR,Iso} = 0$, respectively. For identical materials, $\omega_{RH,Iso} = \sqrt{7\nu^*/2}\omega_N$. The dependence of ω_{RH} and ω_{HR} on γ is shown in Fig. 4.3.1 (a), where it can be seen that ω_{RH} originates at $\omega_{RH,Iso}$ for $\gamma = 0$ and grows unbounded, while ω_{HR} originates at $\omega_{HR,Iso} = 0$, and approaches ω_S asymptotically. In Fig. 4.3.1 (b), we plot the horizontal and rotational displacement amplitudes as functions of γ for these two modes. Different signs of the rotational amplitude indicate that the ω_{RH} and ω_{HR} modes have different motion patterns. In the former, a positive displacement is accompanied by a counterclockwise rotation, while in the latter, it is accompanied by a clockwise rotation.

We note that the zero-frequency mode, $\omega_{HR,Iso}$, corresponds to the rolling motion of an isolated sphere. With the inclusion of a bending rigidity, the sphere would not be allowed to freely roll, and instead would undergo rocking motion of a finite frequency. While non-zero bending rigidity exists in real systems (for instance, a microsphere adhered to a substrate does not freely roll), the frequency of resulting rocking vibrations has been shown [152, 153] to be over an order of magnitude lower than the other contact resonances discussed here. Bending rigidity would thus act as a small perturbation to the predictions of our model, and we do not include it in our analysis.

To illustrate the importance of particle rotations in the model, we note that in the limiting case of $I \to \infty$, when there is no rotation, Eq. (4.11) yields two resonances: a vertical resonance with frequency ω_N, and a horizontal resonance having frequency ω_S. For

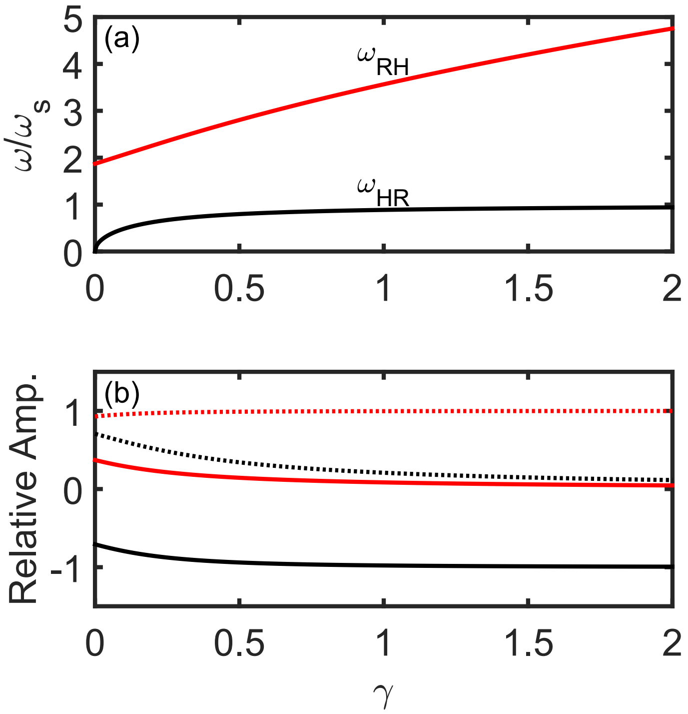

Figure 4.2: (a) Resonance frequencies ω_{RH} (red line) and ω_{HR} (black line) as functions of the stiffness ratio γ. (b) Displacement amplitudes of the resonant modes with frequencies ω_{RH} (red lines) and ω_{HR} (black lines), as functions of the stiffness ratio γ. Solid and dotted lines correspond to Q and $R\theta$, respectively. For each resonance, the amplitudes are normalized such that the sum of squares is unity. The positive sign of $R\theta$ corresponds to counterclockwise rotation.

isolated spheres, the effect of rotations can be thought of as a reduction of the "effective mass" of the sphere to $(2/7)m$, which increases the horizontal resonance frequency. On the other hand, for interacting spheres, rotations dramatically change the dynamics, yielding two horizontal-rotational modes whose frequencies depend on the relative strengths of the sphere-to-sphere and sphere-substrate interactions.

4.3.2 Elastic Substrate

As in the case of the effective medium approximation for a rigid substrate, we assume traveling wave solutions of the form $\hat{Q}e^{i(\omega t-kx)}$ (with similar terms for the other displacements) into Q, Z, and θ in Eq. (4.7). Likewise, we express the variables u_0, w_0, σ_{zx} σ_{zz} in terms of surface wave solutions for the elastic potentials [93] $\phi(x,z,t) = \hat{\phi}e^{k\alpha z+i(\omega t-kx)}$ and $\psi(x,z,t) = \hat{\psi}e^{k\beta z+i(\omega t-kx)}$, and then substitute these expressions into Eq. (4.7) and Eq. (4.8). Here, $(\hat{\cdot})$ is the amplitude of a plane wave in the displacement or potential variable $(\cdot)$, $\alpha = \sqrt{1-\omega^2/(c_L^2k^2)}$, $\beta = \sqrt{1-\omega^2/(c_T^2k^2)}$, and c_L and c_T are the longitudinal and transverse sound speeds of the substrate, respectively. After algebraic manipulation, Eq. (4.7) and Eq. (4.8) are reduced to a homogeneous system of five linear algebraic equations in the five plane wave amplitudes $(\hat{\cdot})$, with coefficients depending on k and ω. We obtain the dispersion relation by seeking nontrivial solutions of this system, which exist only for pairs of k and ω for which the determinant of the following coefficient matrix vanishes:

$$\begin{vmatrix} ik\omega_S^2 & k\beta\omega_S^2 & c_N^2k^2+\phi_S\omega_S^2 & 0 & R\omega_S^2 \\ -k\alpha\omega_N^2 & ik\omega_N^2 & 0 & c_S^2k^2+\phi_N\omega_N^2 & -ikc_S^2 \\ ikR\omega_S^2 & kR\beta\omega_S^2 & R\omega_S^2 & ikc_S^2 & \frac{I}{m}(c_\theta^2k^2+\phi_\theta\omega_\theta^2) \\ 1+\beta^2 & -2i\beta & 0 & \frac{m}{\rho A c_T^2k^2}(c_S^2k^2+\phi_N\omega_N^2-\omega_N^2) & \frac{-m}{\rho A c_T^2k^2}ikc_S^2 \\ -2i\alpha & -(1+\beta^2) & \frac{m}{\rho A c_T^2k^2}(c_N^2k^2+\phi_S\omega_S^2-\omega_S^2) & 0 & 0 \end{vmatrix} = 0, \tag{4.13}$$

where ρ is the density of the substrate, and $A = D^2$ is the area of a primitive unit cell in our square-packed monolayer. We note that the coupling between the spheres and the substrate is represented by elements $(4,4)$, $(4,5)$, and $(5,3)$ of the matrix in Eq. (4.13). Thus, the strength of the coupling can be quantified by the ratio $m/(\rho A)$; if this term is made to vanish (e.g. by making the mass of each sphere much less than that of the portion of the substrate below it, extending to the depth of material influenced by Rayleigh waves), then the substrate and monolayer will be effectively decoupled. We note that if rotations are disregarded (e.g. by letting $I \to \infty$), Eq. (4.13) reduces to the same form as that of the adsorbed monolayer of Ref. [148].

It is instructive to consider the long-wave limit when the spatial derivatives in Eq. (4.7) can be disregarded. In this case, we find the simplified dispersion relation

$$\begin{vmatrix} ik\omega_S^2 & k\beta\omega_S^2 & \phi_S\omega_S^2 & 0 & R\omega_S^2 \\ -k\alpha\omega_N^2 & ik\omega_N^2 & 0 & \phi_N\omega_N^2 & 0 \\ ikR\omega_S^2 & kR\beta\omega_S^2 & R\omega_S^2 & 0 & \frac{I}{m}\phi_\theta\omega_\theta^2 \\ 1+\beta^2 & -2i\beta & 0 & \frac{m}{\rho A c_T^2 k^2}(\phi_N\omega_N^2 - \omega_N^2) & 0 \\ -2i\alpha & -(1+\beta^2) & \frac{m}{\rho A c_T^2 k^2}(\phi_S\omega_S^2 - \omega_S^2) & 0 & 0 \end{vmatrix} = 0. \qquad (4.14)$$

For isolated spheres, there is no approximation in Eq. (4.14) with respect to Eq. (4.13), because, in this case, the terms generated by the spatial derivatives in Eq. (4.7) are identically zero. For interacting spheres, the accuracy of dispersion relations calculated with Eq. (4.14) will be assessed below by a comparison with results obtained with Eq. (4.13). We will see that Eq. (4.14) essentially describes the interaction of contact resonances given by Eq. (4.11) with Rayleigh surface waves.

4.4 Numerical Results and Discussion

In the following calculations, we consider silica spheres of 1.08 μm diameter on a silica substrate, and use the elastic constants (Ref. [154]) $E = 73$ GPa, $\nu = 0.17$, and work of adhesion (Ref. [3]) $w = 0.063$ J/m^2.

4.4.1 Rigid Substrate

We plot numerical solutions[3] of Eq. (4.9), to obtain the dispersion curves for the discrete model of interacting spheres on a rigid base, as shown in Fig. 4.3(a). In our description of a rigid substrate, we assume that no elastic waves propagate in the substrate, but allow local deformation at the points of contact for the purpose of the contact stiffness calculation; this preserves the same contact stiffnesses as in the elastic substrate analysis. We note that due to the periodicity of the system, all three branches have zero-group velocities at the edge of the first irreducible Brillouin zone [17] of the monolayer.

---

[3] See Appendix B for details about numerical solution of dispersion equations.

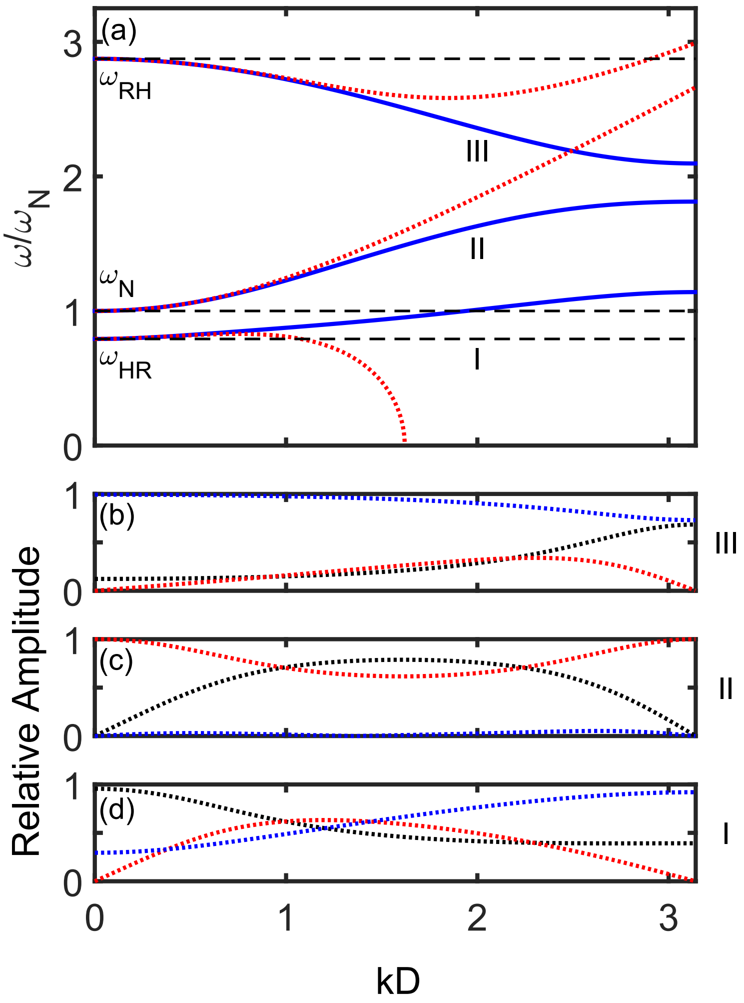

Figure 4.3: (a) Dispersion relation of a monolayer of microspheres adhered to a rigid base. Blue solid and red dotted lines denote, respectively, the discrete and effective medium monolayer descriptions. Black dashed lines denote the contact resonances. (b)-(d) relative amplitudes of the displacement variables Q (black dotted lines), Z (red dotted lines), and $R\theta$ (blue dotted lines), corresponding to the branches of the same numeral for the dispersion of the discrete monolayer adhered to the rigid base shown in (a). The amplitudes are normalized such that the sum of the squared amplitudes is unity.

By substituting the solutions shown in Fig. 4.3(a) into the coefficient matrix of the corresponding algebraic system, we numerically determine the amplitudes of the sphere displacements, which we plot in Fig. 4.3(b-d). By comparing the calculated displacements of with the dispersion curves, we see that each branch takes on the character of its respective contact resonance in the limit $k \to 0$. One can see that each of the three modes generally involves both vertical and horizontal, as well as rotational motion (albeit the rotational component of mode II is quite small). The existence of the three modes with mixed displacements is a consequence of the inclusion of the rotational degree of freedom: without rotations, there would be two modes, one vertical and one horizontal.

We note that, in the special case $K_S = 0$, the mode originating at ω_{HR} becomes purely horizontal and decouples from the other two modes. The remaining modes (characterized by vertical translation and rotation) are generally consistent with the results of Ref. [28], for the case of normal contact with a rigid surface and no bending rigidity. Since Ref. [28] considered hexagonal packing, the behavior is analogous at long wavelengths, but diverges at short wavelengths due to discrete lattice effects.

The dotted lines in Fig. 4.3(a) show dispersion curves calculated with the effective medium model as per Eq. (4.10). The effective medium approximation yields accurate results at long wavelengths but fails at shorter wavelengths with the unphysical behavior of the first mode, whose frequency goes to zero. At even shorter wavelengths, as shown in Fig. 4.4, the effective medium dispersion curves of modes II and III asymptotically approach straight lines with slopes given by c_N and c_S; such behavior has been described by Kosevich and Syrkin [148]. However, this asymptotic behavior is unphysical, because it arises as a short-wavelength asymptotic of a long-wavelength approximation. Indeed, as can be seen from the dispersion curves generated using the discrete model in Fig. 4.4, this asymptotic behavior does not occur in our system. Thus, the inclusion of the first- and second-order spatial derivative terms of Eq. (4.7), while improving the accuracy of the effective medium model at long wavelengths, does not yield much additional understanding of the dynamics of the system.

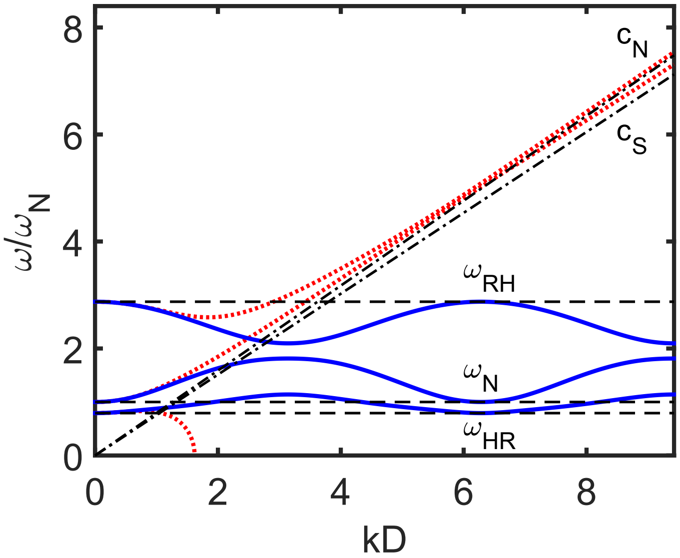

Figure 4.4: Dispersion relation of a monolayer of microspheres adhered to a rigid base, using an extended plotting range. Blue solid, red dotted, and black dashed lines are the same as in Fig. 4.3(a). Black dash-dotted lines denote the asymptotic slopes c_N and c_S.

4.4.2 Elastic Substrate

Isolated Spheres

We numerically solve Eq. (4.14) for the isolated spheres case using $G_S = 0$ and plot the resulting dispersion relation for the effective medium model, as shown in Fig. 4.5. This dispersion relation exhibits classic "avoided crossing" behavior [155] about the resonance frequencies ω_N and $\omega_{RH,Iso} = \sqrt{7/2}\,\omega_S$. In this model, surface acoustic waves (SAWs) in the substrate behave as classical Rayleigh waves at frequencies far from the contact resonances, and the dispersion curves follow the line corresponding to the substrate Rayleigh wave speed c_R [93]. Conversely, sphere motions dominate those of the substrate at frequencies close to the contact resonances. For phase velocities greater than c_T, which correspond to the region $\omega > c_T k$, the wave numbers that solve Eq. (4.13) are complex valued; these solutions are "leaky" modes for which energy leaves the surface of the substrate, and radiates into

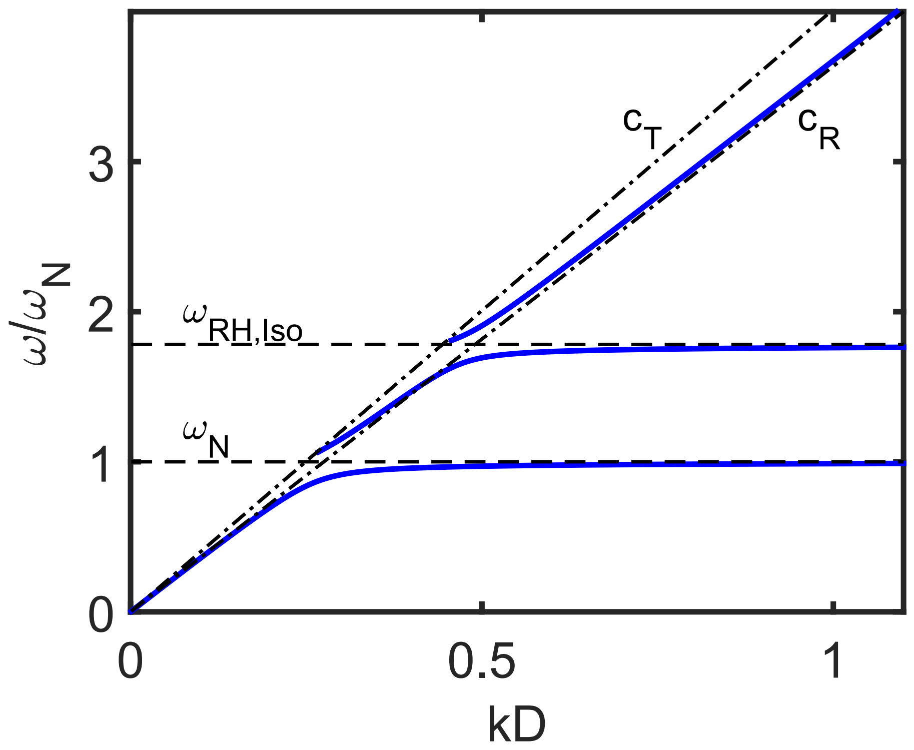

Figure 4.5: Dispersion relation of SAWs in an elastic half space coupled to a monolayer of isolated microspheres, denoted by the blue solid lines. Black dashed lines denote the contact resonances, and black dash-dotted lines denote the transverse and Rayleigh waves speeds of the substrate.

it. This isolated spheres case is particularly applicable in systems where adhesion between particles is negligible, e.g. for: macroscale particles without lateral compression where the dominant static compression is due to gravity and is between the particles and substrate; or for microscale particles, if the separation distance between particles is larger than the range of adhesion forces.

Interacting Spheres

In Fig. 4.6(a), we plot numerical solutions of Eq. (4.14). The amplitudes of the sphere and substrate displacements are calculated in the same manner as in Fig. 4.3, and are plotted

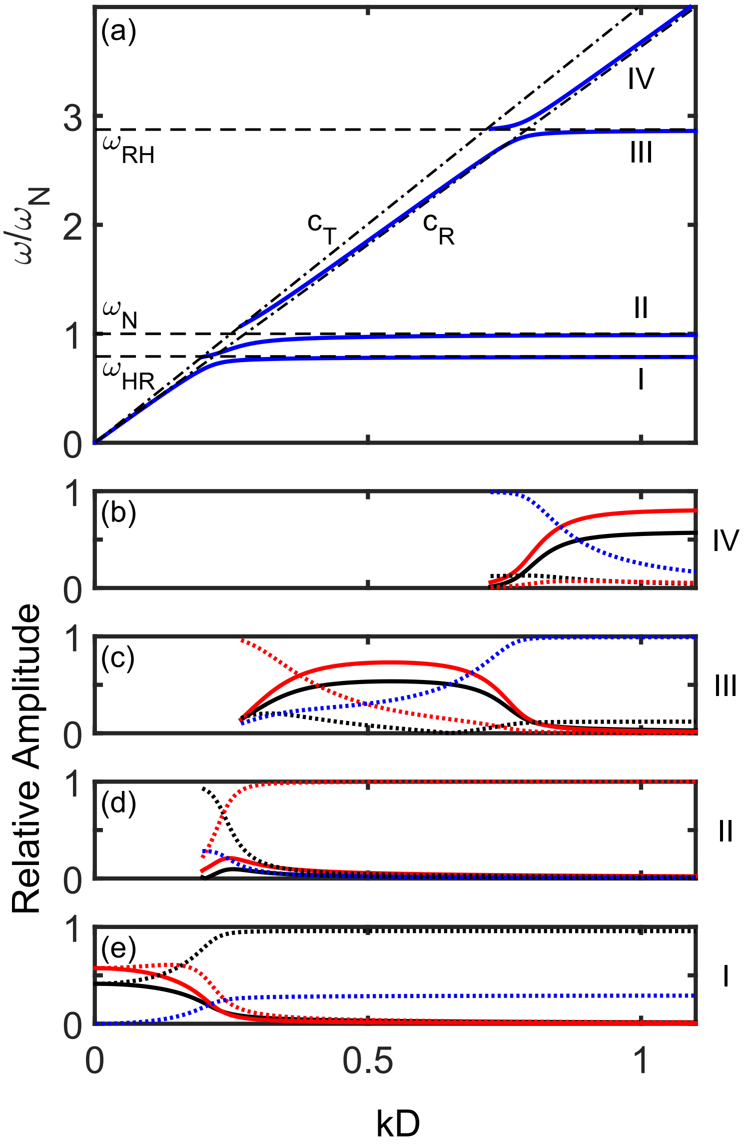

Figure 4.6: (a) Blue solid lines denote the dispersion relation of SAWs in an elastic halfspace coupled to a monolayer of interacting microspheres. Black dashed lines denote the contact resonances, and black dash-dotted lines denote wave speeds in the substrate. (b)-(e) relative amplitudes of the displacement variables u_0 (black solid lines), w_0 (red solid lines), Q (black dotted lines), Z (red dotted lines), and $R\theta$ (blue dotted lines), corresponding to the branch denoted by the same numeral in (a). The amplitudes are normalized such that the sum of the squared amplitudes is unity.

in Fig. 4.6(b-e). In Fig. 4.6(a), we observe features qualitatively similar to the dispersion relation for isolated spheres in Fig. 4.5, with the exception of a third avoided crossing at frequency ω_{HR}. The mode shapes reveal the ways in which each of the branches are influenced by the contact resonances, as well as long and short wavelength asymptotic behavior of our system. In the long wavelength limit, the substrate motions closely resemble Rayleigh SAWs. Since the frequencies of waves in this regime are well below the contact resonances, the effect of the spheres is negligible, and the monolayer moves in phase with the substrate surface. At short wavelengths, it can be seen that the first, second, and third lowest branches exhibit motions dominated by the displacements Q, Z, and θ, respectively (each corresponding to a resonant mode of the monolayer), while the highest branch tends toward the Rayleigh SAW. The effects of proximity to the contact resonances are well illustrated, for example, by branch III of Fig. 4.6(a), which exhibits large vertical sphere motions at its starting point near ω_N, resembles the Rayleigh SAW as it approaches and crosses the c_R line, and transitions into large rotational sphere motions after the avoided crossing with ω_{RH}.

In order to examine the behavior of our system throughout the entire Brillouin zone, we superimpose the dispersion curves for the effective medium model of interacting spheres on an elastic base including higher order spatial derivative terms (the full Eq. (4.13)) with the dispersion curves for the discrete monolayer on a rigid substrate (Eq. (4.9)), as shown in Fig. 4.7. At long wavelengths the discreteness of the monolayer is insignificant, and the dispersion is well described by the effective medium model. Furthermore, we note that at long wavelengths the dispersion curves calculated using the effective medium model including higher order terms shown in Fig. 4.7, only slightly deviate from the dispersion curves calculated using the effective medium model with the higher order terms neglected, which are shown in Fig. 4.6(a). The only noticeable effect is a downshift in frequency of the avoided crossing between the Rayleigh wave and the ω_{RH} resonance. Since the latter intersects at the highest wave vector of the three contact resonances, calculations with Eq. (4.14) are the least accurate. In Fig. 4.7, at short wavelengths (beyond the avoided crossings with the Rayleigh wave branch), the elasticity of the substrate has little effect on the dynamics, and the dispersion

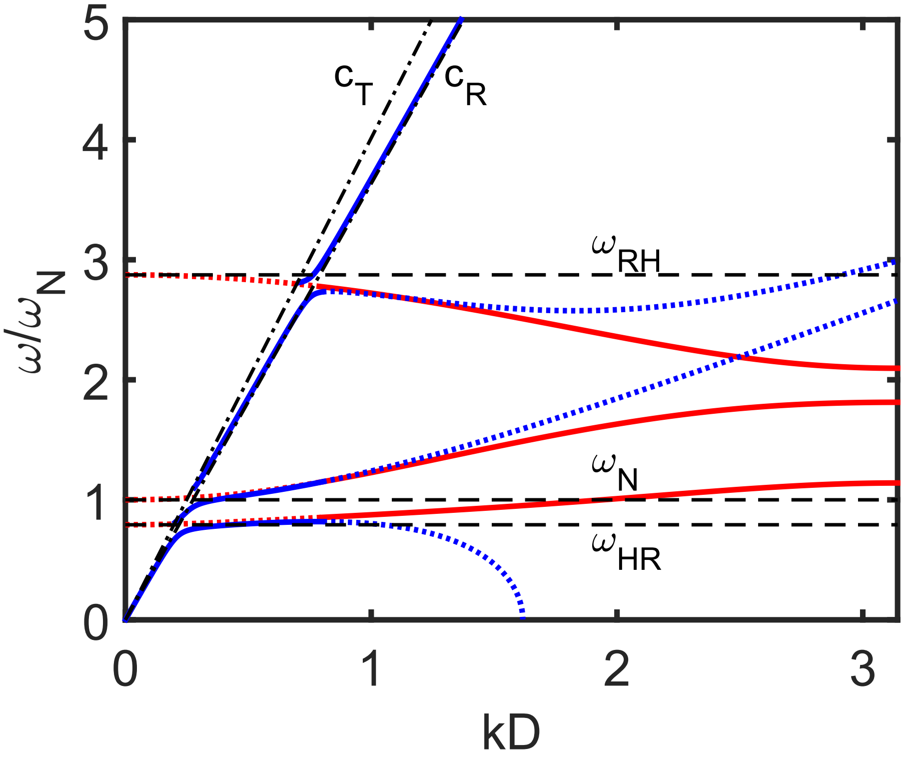

Figure 4.7: Blue lines denote the SAW dispersion relation with spatial derivative terms included and red lines denote the dispersion relation of a discrete monolayer adhered to a rigid base. Solid and dotted lines denote, respectively, valid and invalid ranges for the two models. Black dashed and dash-dotted lines are the same as in Fig. 4.3(a).

can be described using the discrete model for interacting spheres on a rigid substrate. We suggest that by “stitching together” the effective medium model for spheres on an elastic substrate with the discrete model for spheres on a rigid substrate, we can simultaneously capture the interaction of SAWs with the monolayer at long wavelengths and effects caused by the discreteness of the spheres at short wavelengths. Past the avoided crossings, the two sets of curves in Fig. 4.7 stitch together smoothly, resulting in a full picture of the monolayer dynamics on the elastic substrate.

4.5 Experimental Implications

We expect the presented results to be useful for predicting complex dynamic responses and extracting effective contact stiffnesses from measurements of acoustic dispersion in a manner similar to Boechler *et al.* [8]. The findings described above invite several questions, including whether our model of a square lattice is applicable to results on hexagonally packed monolayers, and why horizontal-rotational resonances were not observed in the experiment [8].

We believe that the assumption of the square lattice is not essential. For isolated spheres, Eqs. (4.7) and (4.8) with G_N and G_S set to zero are applicable for any arrangement of the spheres, periodic or random, with the only parameter depending on the arrangement being the surface area per sphere A. For interacting spheres, the results generally do depend on the lattice structure and the propagation direction. However, the contact resonances given by Eq. (4.12) correspond to the $k = 0$ limit and, consequently, do not depend on the propagation direction. The relative positions of the three contact resonances may be different in the long wavelength limit between a hexagonal and square packed lattice, but their presence should still be expected in both cases.

We suggest that the reasons why horizontal-rotational resonances were not observed in Ref. [8] may be the following. Since the measurements were not sensitive to horizontal motion, the ω_{RH} and ω_{HR} resonances could only be detected when they hybridized with SAWs near avoided crossings, and since the avoided crossings with ω_{RH} and ω_{HR} resonances are more narrow than the one with the ω_N resonance, they could have been missed. Furthermore, our model assumes that all spheres are either connected by identical springs or are isolated. If the contact stiffness between spheres were to vary widely (some neighboring spheres being in contact and others not, for example), then distinct resonances may be absent. In addition, the upper (ω_{RH}) resonance may have been outside the range of the measurements in Ref. [8]. Further experimental studies of monolayer dynamics in conjunction with exploration of ways to control sphere-to-sphere contacts should help resolve the discrepancy between the theory and experiment.

While the main focus of this work has been on microgranular monolayers, our theory is equally valid for nano- to macroscale systems. Contact resonances of isolated nanoparticles have been previously demonstrated for spheres as small as 120 nm in diameter, and their frequencies have been shown to scale in agreement with adhesive contact models based on Hertzian mechanics [156]. Conversely, at the macroscale, contact springs would be determined by gravity and, possibly, applied lateral static compression [140, 141, 142], rather than by adhesion forces. We note that several past experimental works on macroscale granular systems [140, 141, 142] have observed systematic upshifts in frequency relative to theoretical predictions, and have suggested uncertainties in material parameters and experimental setups, as well as deviations from Hertzian contact behavior as possible causes. As per the results from our model, the presence of additional degrees of freedom and interactions between spheres and substrate may also be possible causes. In the absence of the external lateral compression, highly nonlinear "sonic vacua" [4] should also be expected. Generally, as amplitudes are increased, interesting nonlinear dynamics are expected for granular monolayers due to nonlinearity of Hertzian contacts between the particles [4, 5] and between the particles and the substrate [157].

4.6 Conclusion

We have developed a model for wave propagation in granular systems composed of a monolayer of spheres on an elastic substrate. Our model expands on those used in previous works, and Chapters 2 and 3, by including the elasticity of the substrate, horizontal and rotational sphere motions, shear coupling between the spheres and substrate, and interactions between adjacent spheres. We have shown that a monolayer of interacting spheres on a rigid substrate supports three modes involving vertical, horizontal, and rotational motion. In the long-wavelength limit, these modes yield three contact resonances, one purely vertical and two of mixed horizontal-rotational character. On an elastic substrate, these resonances hybridize with the Rayleigh surface wave yielding three avoided crossings. For isolated spheres, the frequency of the lower horizontal-rotational resonance, in the absence of bending rigidity, tends to zero and only two contact resonances with two respective avoided crossings remain.

By comparing the effective medium (valid for long wavelengths) to the discrete formulation of our model, we have demonstrated that for the presented microsphere monolayer example, the effective medium model can be used to describe the interaction of the contact resonances with the Rayleigh waves in the substrate, but loses accuracy at shorter wavelengths. In that case, the substrate can be considered rigid, and the discrete model is more appropriate. This model is scalable in that it can be adapted for use with nano- to macroscale systems, and provides a means to experimentally extract contact stiffnesses from dynamic measurements. Opportunities for future studies include exploration of analogous models for granular monolayers in the nonlinear regime, as well as analysis of the transverse modes of a granular monolayer or granular chain on a substrate. Further experiments on nano- to macroscale granular monolayers will help guide the modeling effort.

4.7 Related Experimental Work[4]

In this section, we highlight experimental works that have been supported by the analytical model in this chapter. The three contact resonances were observed in recent experiments on a monolayer of silica microspheres adhered to a substrate [56], wherein the horizontal-rotational resonance frequencies were selectively increased via the deposition of a thin layer of aluminum, which stiffened the interparticle contacts without affecting the sphere-substrate contacts. The resonances were measured using a knife-edge photodeflection detection technique [58]. To match the resonance peaks identified in the frequency domain experimental data to the correct motion (vertical or horizontal-rotational), the experiments were repeated using a grating interferometer [59] in place of the knife-edge technique. While the knife-edge method is sensitive to the motion of all three resonances, the grating interferometer is only sensitive to the vertical resonance, which allows the unique identification of the vertical resonance. In an additional experimental study [158], as well as an accompanying theoretical work [159], this model is adapted to examine a hexagonally-packed monolayer. In contrast to previous

---

[4] This content is not adapted from Ref. [137]

works on microgranular monolayers [8, 56, 55, 57], the monolayer studied therein is very well-ordered, which allows the measurement of contact-based vibration modes well into the Brillouin zone, outside the regime where a long-wavelength approximations are valid.

Chapter 5

NONLINEAR DYNAMICS OF A 1D GRANULAR CRYSTAL ADHERED TO A SUBSTRATE

5.1 Introduction

In Ch. 4, it was shown that a monolayer of microspheres adhered to a substrate possesses three sagittally-polarized modes. The analysis in Ch. 4 was restricted to the linear regime. In this chapter, we study an extension of the linear model that includes contact nonlinearity, for the case of a rigid substrate. We focus on the weakly-nonlinear regime, where the relative displacements are not small compared to the static overlap (but not large enough to cause loss of contact). Using a quasi-discreteness approximation, we derive a Nonlinear Schrodinger (NLS) equation [128] that describes the slow modulation of a single, high-amplitude carrier wave in any of the three linear modes. Previous works have used the NLS equation to describe nonlinear diatomic lattices [160] and analogous behavior in macroscale, diatomic GCs [114], as well as an asymptotic limit of the 1D, mass-in-mass chain presented in Ch. 3 [94]. Closely related discrete variants of the NLS equation have also been used to describe diatomic chains [161] and monatomic chains with on-site potentials [162]. The NLS equation derived in this work may be of either focusing or defocusing type, depending on the frequency and wave number of the carrier wave. Finally, we simulate a nonlinear monolayer chain via direct numerical integration, and find that nonlinear, localized modes of the chain are well approximated by both bright and dark breather solutions of the derived nonlinear Schrodinger equation. This work extends the prior models of 1D, precompressed GCs, which lack either shear and rotation [5] or nonlinearity [38, 137], and is applicable to recent experimental setups involving self-assembled microsphere monolayers [8, 56] and macroscale granular chains with magnetic precompression [37].

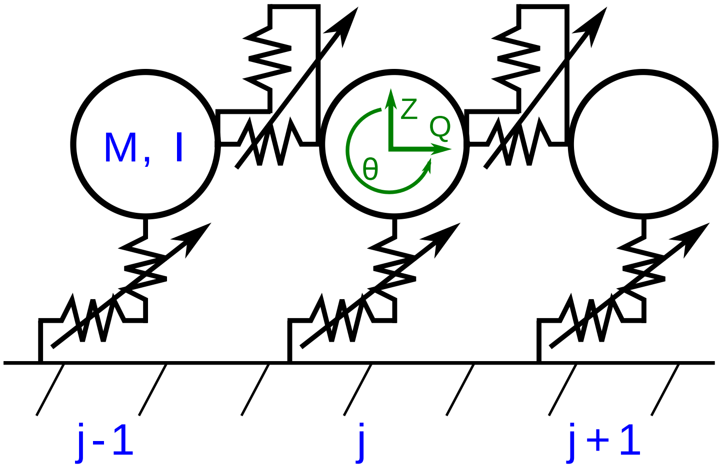

Figure 5.1: Schematic of the nonlinear monolayer model.

5.2 Model

A schematic of the monolayer model is shown in Fig. 5.1. The model consists of a chain of spheres with mass M and moment of inertia I, which are connected to each other and to a rigid substrate by nonlinear normal and shear springs. The spheres have diameter $D = 2R$, and the horizontal, vertical, and angular displacements of the sphere with index j are given by q_j, z_j, and θ_j, respectively. The spacing between adjacent sphere centers is considered to be D. For ease of notation in the following equations, we define $\vec{\delta} = (\delta_N, \delta_S)$ as a vector whose components are the normal and transverse components (respectively) of a change in displacement between the centers of two spheres. The "normal" and "transverse" directions are defined relative to the contact plane; they are not fixed in the inertial reference frame. For example, the normal component is in the (vertical/horizontal) direction for sphere-(substrate/sphere) contacts.

5.2.1 Normal contact: Hertz/DMT model

The contact force in the normal direction is given by the Hertz contact law [13]:

$$F_N^{(\cdot)}(\vec{\delta}) = A^{(\cdot)} \left[\delta_0^{(\cdot)} - \delta_N\right]_+^{3/2}, \tag{5.1}$$

where $(\cdot)$ is a placeholder for superscript g or i (denoting sphere-ground and intersphere contacts, respectively), $A^{(\cdot)}$ is a stiffness constant that depends on geometric and material properties, and $\delta_0^{(\cdot)}$ is the static overlap induced by precompression (e.g. via adhesive or magnetic attraction or a static external load). The subscript + indicates that the contact is tensionless (that is, the bracketed term vanishes if its argument becomes negative).

5.2.2 Shear contact: Mindlin Model

The contact force in the transverse direction is given by the Hertz-Mindlin model with the assumption of no slip [13]:

$$F_S^{(\cdot)}(\vec{\delta}) = B^{(\cdot)}\delta_S \left[\delta_0^{(\cdot)} - \delta_N\right]_+^{1/2}, \tag{5.2}$$

where $B^{(\cdot)}$ is another stiffness constant that depends on geometric and material properties.

5.3 Equations of Motion

Force and moment balances about sphere j give the equations of motion:

$$\begin{aligned} m\ddot{q}_j &= -F_S^g(\vec{\delta}^g) + F_N^i(\vec{\delta}_-^i) - F_N^i(\vec{\delta}_+^i) && (5.3)\\ m\ddot{z}_j &= F_N^g(\vec{\delta}^g) - F_N^g(\vec{\delta}_0^g) + F_S^i(\vec{\delta}_+^i) - F_S^i(\vec{\delta}_-^i) && (5.4)\\ I\ddot{\theta}_j &= R\left(-F_S^g(\vec{\delta}^g) + F_S^i(\vec{\delta}_+^i) + F_S^i(\vec{\delta}_-^i)\right), && (5.5) \end{aligned}$$

where

$$\begin{aligned} \vec{\delta}^g &= (z_j,\ q_j + R\theta_j) && (5.6)\\ \vec{\delta}_+^i &= (q_{j+1} - q_j,\ z_{j+1} - z_j - R(\theta_{j+1} + \theta_j)) && (5.7)\\ \vec{\delta}_-^i &= (q_j - q_{j-1},\ z_j - z_{j-1} - R(\theta_j + \theta_{j-1}))\,. && (5.8) \end{aligned}$$

5.3.1 Nondimensionalization

We normalize the translational displacements by the interparticle static overlap as $Z_j = z_j/\delta_0^i$ and $Q_j = q_j/\delta_0^i$, and the angular displacement as $\Phi_j = R\theta_j/(\delta_0^i mR^2/I)$. We normalize the time variable as $\tau = \omega_N t$, where $\omega_N = \sqrt{(3/2)A_G\sqrt{\delta_0^g}/m}$ is the frequency of the normal contact resonance in the linear limit.

5.3.2 Expansion of Nonlinear Forces

Since we are concerned with only weak nonlinearity, we expand the forces $F_N^{(\cdot)}(\vec{\delta})$ and $F_S^{(\cdot)}(\vec{\delta})$ in Taylor Series to the third order:

$$\begin{aligned} F_N^{(\cdot)}(\bar{\delta}) &\simeq A^{(\cdot)}{\delta_0^{(\cdot)}}^{3/2} - \frac{3}{2}A^{(\cdot)}{\delta_0^{(\cdot)}}^{1/2}\delta_N + \frac{3}{8}A^{(\cdot)}{\delta_0^{(\cdot)}}^{-1/2}{\delta_N}^2 + \frac{1}{16}A^{(\cdot)}{\delta_0^{(\cdot)}}^{-3/2}{\delta_N}^3 + \mathcal{O}({\delta_N}^4) \quad (5.9) \\ F_S^{(\cdot)}(\bar{\delta}) &\simeq B^{(\cdot)}{\delta_0^{(\cdot)}}^{1/2}\delta_S - \frac{1}{2}B^{(\cdot)}{\delta_0^{(\cdot)}}^{-1/2}\delta_N\delta_S - \frac{1}{8}B^{(\cdot)}{\delta_0^{(\cdot)}}^{-3/2}{\delta_N}^2\delta_S + \mathcal{O}({\delta_N}^3\delta_S). \quad (5.10) \end{aligned}$$

5.3.3 Dimensionless Equations of Motion

Substituting (5.1) - (5.2) and (5.6) - (5.8) into (5.3) - (5.5) and switching to the normalized variables, we find the dimensionless equations of motion given in Appendix C.

5.4 Dispersion Relation

In the linear (small amplitude) limit, the nonlinear terms in (C.1) - (C.3) can be neglected. By assuming solutions of the form $Q_j(\tau) = \hat{Q}\mathrm{e}^{\mathrm{i}(kjD-\omega\tau)}$ (with similar expressions for Z_j and Φ_j), where k is the wave number and ω is the angular frequency, we derive the dispersion relation $\det(M_1(k,\omega)) = 0$, where

$$M_1 = \begin{pmatrix} -\omega^2 + K_s - 2G_n(\varphi_1 - 1) & 0 & \mu K_s \\ 0 & -\omega^2 + K_n - 2G_s(\varphi_1 - 1) & 2\mathrm{i}\mu G_s\psi_1 \\ K_s & -2\mathrm{i}G_s\psi_1 & -\omega^2 + \mu K_s + 2\mu G_s(\varphi_1 + 1) \end{pmatrix}, \quad (5.11)$$

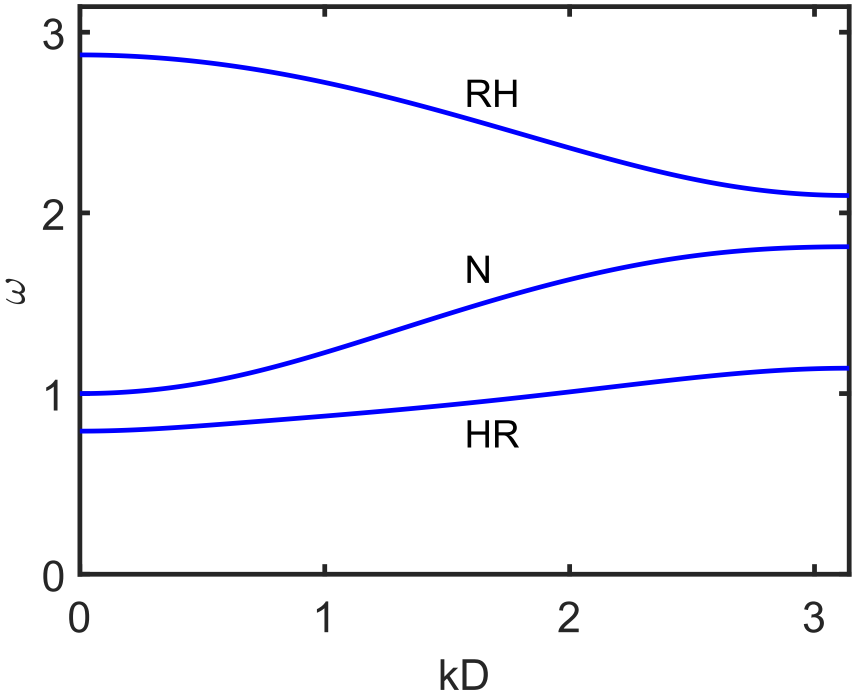

Figure 5.2: Dispersion relation of the monolayer in the linear limit.

$\varphi_1 = \cos(kD)$, and $\psi_1 = \sin(kD)$. This dispersion relation has three branches: the “N” mode, which consists primarily of displacements in the direction normal to the substrate (i.e. Z_j), the “HR” mode, which is predominantly horizontal translational motion (but with some rotation), and the “RH” mode, which is composed of mostly rotational motion, but with some horizontal translation [137].

5.5 *Derivation of the Nonlinear Schrodinger Equation*

5.5.1 Slow Modulation of an Envelope

In the weakly nonlinear regime, the waves can be described as a slow modulation of a carrier wave. To find the NLS equation, we seek an approximate solution of Eqs. (C.1) - (C.3) in the form $Q_j = S(X,T)\mathrm{e}^{\mathrm{i}(kjD-\omega\tau)} + h.o.t.$ [128], where the envelope S is described by the "slow" variables

$$\begin{aligned} X &= \varepsilon(jD - v\tau) && (5.12) \\ T &= \varepsilon^2\tau. && (5.13) \end{aligned}$$

Here, ε is a small, dimensionless parameter, and v is a speed to be determined. The higher order terms ($h.o.t.$) are chosen to eliminate the error of the approximation to a desired order of ε.

5.5.2 Quasi-Discreteness Approximation

Since the rescaled displacement X varies slowly relative to the sphere spacing D (e.g. an increment in j causes a very small change εjD in X), the envelope function at an adjacent lattice site can be approximated via Taylor series as

$$S(X \pm \varepsilon D, T) = S(\varepsilon((j\pm 1)D - v\tau), T) \approx S(X,T) \pm (\varepsilon D)S_X + \frac{(\varepsilon D)^2}{2}S_{XX} + \mathcal{O}(\varepsilon^3). \quad (5.14)$$

Thus, we consider the envelope to vary continuously in the slow spatial variable X, while the carrier wave depends on the discrete variable j.

5.5.3 Ansatz

For ease of notation, we abbreviate the carrier wave as $E = \mathrm{e}^{\mathrm{i}(kjD-\omega\tau)}$. To derive approximate the system using the NLS equation, we will need several higher order terms. The complete ansatz is

$$\begin{aligned} Q_{an} &= \varepsilon\left[a_1SE + c.c.\right] + \varepsilon^2\left[a_2S^2E^2 + a_5S_XE + c.c. + a_3S\bar{S}\right] \\ &\quad + \varepsilon^3\left[a_4S^3E^3 + a_6SS_XE^2 + a_7S\bar{S}_X + a_8S_TE + a_9S_{XX}E + a_{10}|S|^2SE + c.c.\right] \end{aligned} \tag{5.15}$$

$$\begin{aligned} Z_{an} &= \varepsilon\left[b_1SE + c.c.\right] + \varepsilon^2\left[b_2S^2E^2 + b_5S_XE + c.c. + b_3S\bar{S}\right] \\ &\quad + \varepsilon^3\left[b_4S^3E^3 + b_6SS_XE^2 + b_7S\bar{S}_X + b_8S_TE + b_9S_{XX}E + b_{10}|S|^2SE + c.c.\right] \end{aligned} \tag{5.16}$$

$$\begin{aligned} \Phi_{an} &= \varepsilon\left[c_1SE + c.c.\right] + \varepsilon^2\left[c_2S^2E^2 + c_5S_XE + c.c. + c_3S\bar{S}\right] \\ &\quad + \varepsilon^3\left[c_4S^3E^3 + c_6SS_XE^2 + c_7S\bar{S}_X + c_8S_TE + c_9S_{XX}E + c_{10}|S|^2SE + c.c.\right], \end{aligned} \tag{5.17}$$

where (a_n, b_n, c_n) are frequency-dependent constants that must be determined.

5.5.4 Solvability Conditions

To avoid cluttered notation in the following derivation, we define the following constants as the dimensionless Taylor series coefficients:

$$\alpha_1 = K_n \quad \alpha_2 = -K_n/4 \quad \alpha_3 = -K_n/24 \tag{5.18}$$

$$\beta_1 = K_s \quad \beta_2 = -K_s/2 \quad \beta_3 = -K_s/8 \tag{5.19}$$

$$\gamma_1 = G_n \quad \gamma_2 = -G_n/4 \quad \gamma_3 = -G_n/24 \tag{5.20}$$

$$\eta_1 = G_s \quad \eta_2 = -G_s/2 \quad \eta_3 = -G_s/8, \tag{5.21}$$

and the following periodic functions of the wave number k:

$$\varphi_m = \cos(mkD) \tag{5.22}$$

$$\psi_m = \sin(mkD), \tag{5.23}$$

where m may take the value 1 or 2. By substituting the ansatz (5.15) - (5.17) into (C.1) - (C.3) and applying the continuum approximation (5.14), and after moving all terms to the left-hand side of each equation, we obtain three residuals, which must be eliminated to achieve error on the order of ε^4. This results in a hierarchy of solvability conditions at each order of ε, which are used to find the unknown coefficients a_1, a_2, etc. The results are highlighted in Appendix C. By satisfying the solvability conditions, we arrive at a single NLS equation to describe the modulation of the envelope:

$$\mathrm{i}\lambda_8 S_T + \lambda_9 S_{XX} + \lambda_{10}|S|^2 S = 0, \tag{5.24}$$

where λ_8, λ_9, and λ_{10} are functions of wave number and frequency, and are generally complex. Equation (5.24) can be put into a form in which λ_8, λ_9, and λ_{10} are all real by uniformly shifting the complex phase of all terms (for example, by multiplying Eq. (5.24) by $\exp(-\mathrm{i}\angle(\lambda_9))$. In the following sections, without loss of generality, we assume that λ_8, λ_9, and λ_{10} are all real.

5.5.5 Focusing and Defocusing Behavior

The NLS equation is considered “focusing” or “defocusing,” depending on the ratio of the dispersive and nonlinear terms. Let $\sigma = \mathrm{sign}(\lambda_{10}/\lambda_9)$. If $\sigma = (+1, -1)$, the NLS is (focusing, defocusing). The ratio σ usually corresponds to the concavity of the dispersion curves, i.e. $\mathrm{sign}(\frac{\partial^2\omega(k)}{\partial k^2})$. The focusing NLS equation has so-called “bright” soliton solutions, for which energy is localized in space. Conversely, the defocusing NLS equation has “dark” soliton solutions, for which a localized, low-energy “dark spot” appears against a bright background carrier wave.

For this system, the NLS equation for a carrier wave in the N mode is focusing when $k = 0$, and transitions to defocusing behavior near the middle of the Brillouin zone. The (HR/RH) modes are (focusing/defocusing) at low k, and (defocusing/focusing) for $k = \pi$. A special case occurs for the HR and RH modes in the limit $k \to 0$: the nonlinearity coefficient λ_{10} vanishes. No nonlinear effects are present in this limit because the carrier wave has no vertical displacement and no relative horizontal displacement between spheres. Physically speaking, the contact areas do not change in these modes of deformation, so the effective stiffness is constant.

5.5.6 Breather Solutions

Some well-known solutions of Equation (5.24) are the so-called *breather* solutions, which are spatially localized and oscillate in time, and are known in analytical form [128]. In particular, the *bright* and *dark* breather solutions, which are solutions of the focusing and defocusing NLS equations, respectively, are given by

$$S_b(X,T) = \sqrt{A}\xi_1 \operatorname{sech}(\sqrt{A}\xi_2 X)\mathrm{e}^{\mathrm{i}\nu AT} \tag{5.25}$$

and

$$S_d(X,T) = \sqrt{A}\zeta_1 \tanh(\sqrt{A}\zeta_2 X)\mathrm{e}^{\mathrm{i}\nu AT}, \tag{5.26}$$

where $\nu = \sigma \operatorname{sign}(\lambda_8/\lambda_9)$, $\xi_1 = \sqrt{2\nu\lambda_8/\lambda_{10}}$, $\xi_2 = \sqrt{\nu\lambda_8/\lambda_9}$, $\zeta_1 = \sqrt{\nu\lambda_8/\lambda_{10}}$, and $\zeta_2 = \sqrt{-(\nu/2)\lambda_8/\lambda_9}$. Plots of the lattice profile resulting from a few example breather solutions are shown below in Fig. 5.3. From these profiles, we observe that the envelopes are not all symmetric about the central lattice site; this asymmetry is due to the presence of both even- and odd-power nonlinearities in the equations of motion [163].

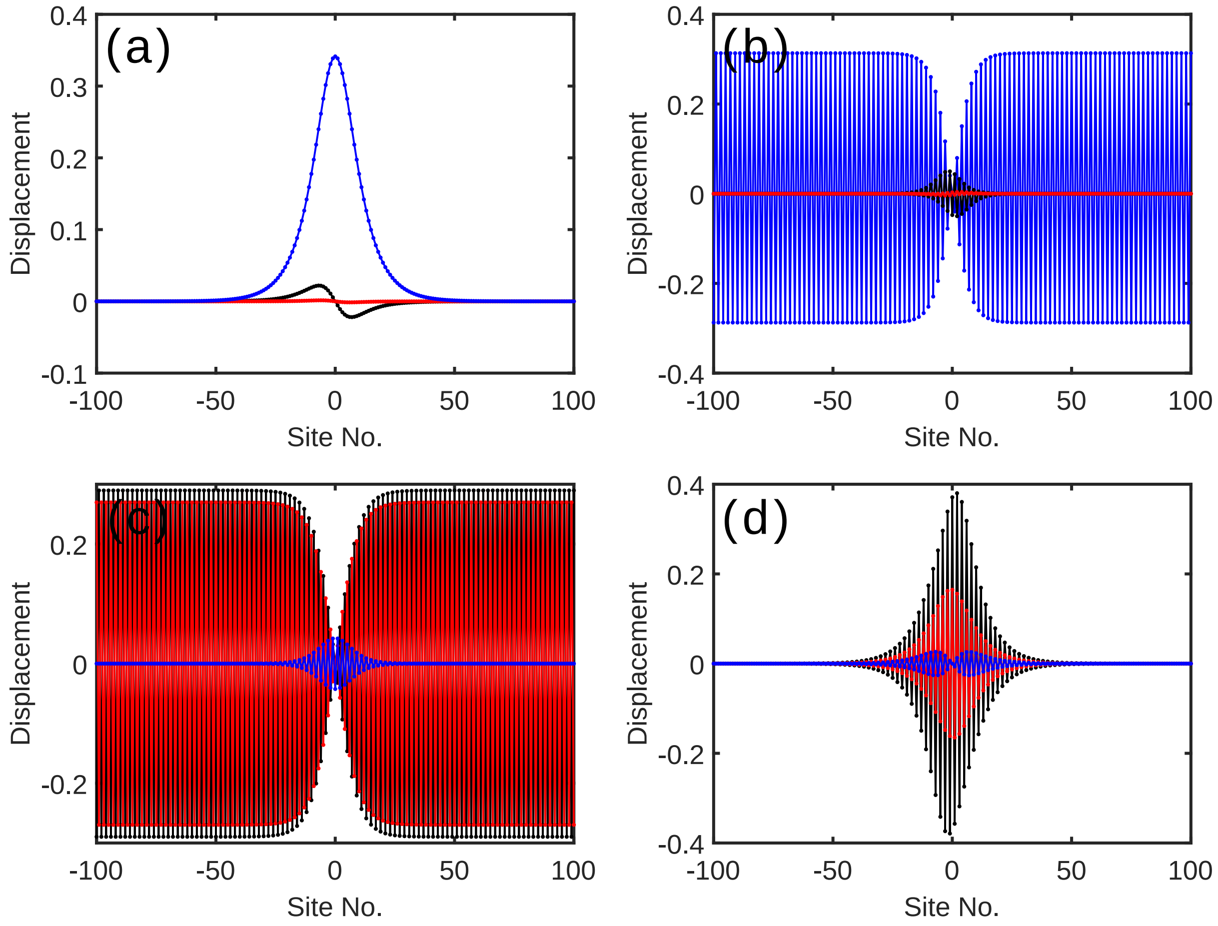

Figure 5.3: Spatial profiles of breather solutions of the monolayer for the cases (a) N mode, $kD = 0$ (focusing); (b) N mode, $kD = \pi$ (defocusing); (c) HR mode, $kD = \pi$ (defocusing); (d) RH mode, $k = \pi$ (focusing). In all panels, the black, blue, and red dots correspond the the displacements Q_j, Z_j, and Φ_j. Connecting lines in the corresponding colors are shown as a visual aid. For all cases, we use the parameters $\varepsilon = 0.01$ and $A = 36$.

5.6 Numerical Results

The validity of the NLS approximation is tested by comparing breather solutions with the direct numerical solution of the equations of motion (5.3) - (5.5), with periodic boundary conditions. Spatiotemporal plots of the dimensionless kinetic energy $KE = (1/2)\dot{Q}_j^2 + (1/2)\dot{Z}_j^2 + (1/2)\dot{\Phi}_j^2$ are shown in Fig. 5.4. We find that the breather profiles result in very little radiation or shape change over hundreds of oscillations, indicating that the fully nonlinear dynamics of the discrete chain are well described by the NLS. However, the accuracy of the approximation could be better quantified via analysis of the stability of intrinsic localized modes of the fully nonlinear lattice, which we leave for future work.

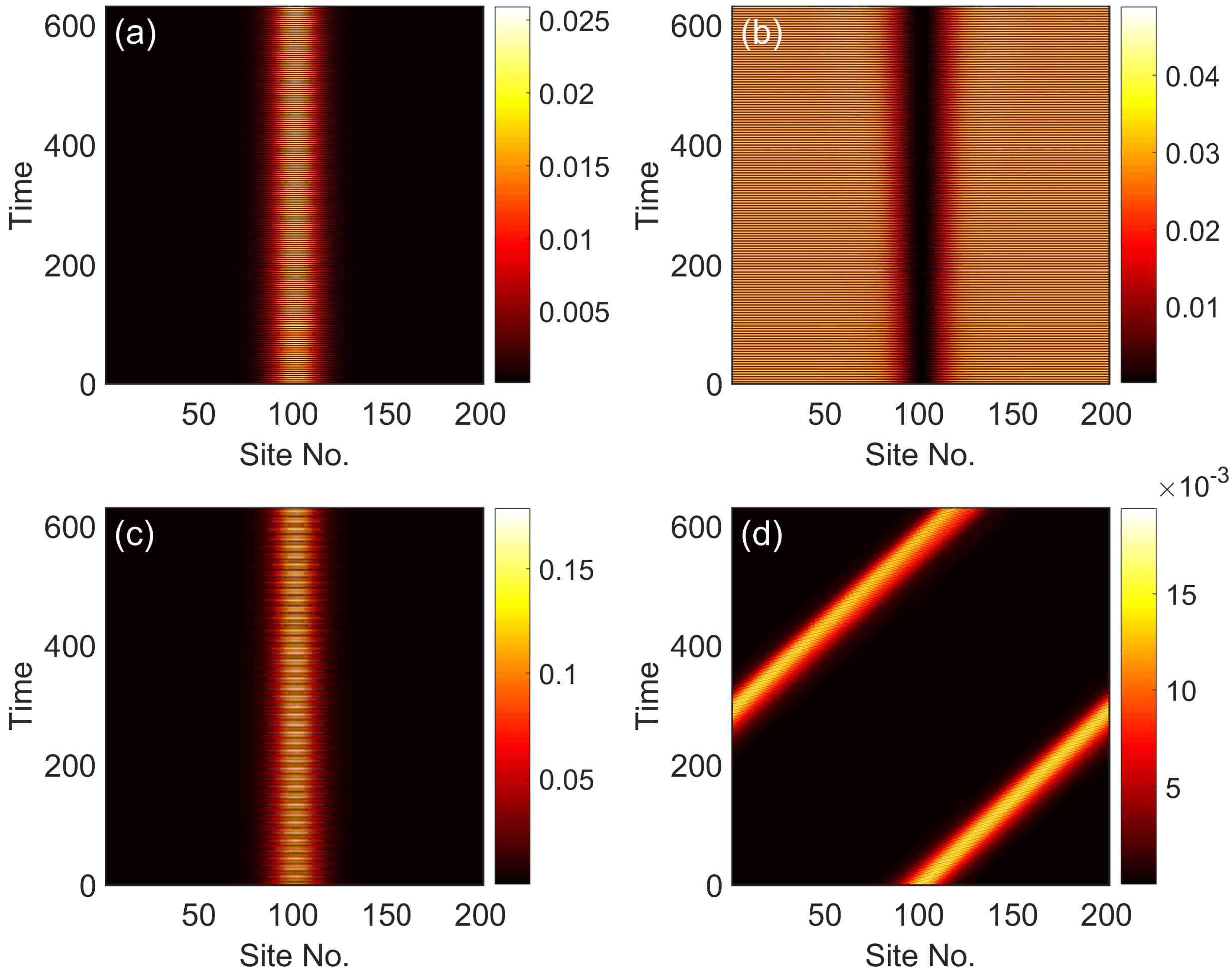

Figure 5.4: Spatiotemporal plots of breather kinetic energy for the following cases: (a) N mode, $kD = 0$; (b) HR mode, $kD = \pi$; RH mode, $kD = \pi$; (d) N mode, $kD = \pi/4$. For all cases, we use the parameters $\varepsilon = 0.04$ and $A = 1$.

5.7 Conclusions

In this chapter, we have extended the monolayer/rigid substrate model to include weak contact nonlinearity. This model differs from past analyses of weakly-nonlinear wave propagation in granular chains in that it includes shear interactions and rotations, which introduce more propagation modes, as well as a substrate, which causes coupling between longitudinal and transverse motions. Slow modulations of a carrier wave in any of the three modes can be modeled using the NLS equation, which can be of either focusing or defocusing type, depending on the mode of the carrier wave. Finally, we have simulated breather solutions from the NLS model using the full nonlinear equations of motion, and shown that the theoretical approximation works well for small and large wave numbers.

Our analysis opens up several opportunities for future studies. First, the model applies to existing experimental setups, such as a monolayer of microspheres adhered to a substrate, in regimes where interactions with surface acoustic waves in the substrate are minimal. It would also be very interesting to model the interaction between two or three envelopes, as the current NLS model only accounts for one at a time, and it may be difficult to excite only a single mode in experiments. A closely-related setup would be a damped-driven variation of our model, which would be more experimentally relevant in a macroscale setup with a shorter chain (i.e. tens of spheres instead of hundreds or thousands). Finally, the stability of the intrinsic localized modes of our monolayer should be analyzed, which could be done using a continuation method (e.g. in the spirit of Ch. 3).

Chapter 6

SHEAR TO LONGITUDINAL MODE CONVERSION VIA SECOND HARMONIC GENERATION IN A 2D MICROSCALE GRANULAR CRYSTAL[1]

This chapter builds upon the prior chapters, which considered wave propagation in 2D microscale granular crystals adhered to elastic substrates having motion in the saggital plane, to consider plane wave propagation in a 2D microscale model without a substrate (accounting for nonlinearity, normal and shear interactions, and particle rotation). In contrast to the previous chapters, this type of model considers 2D particle translations within the monolayer plane, and particle rotations with the axis of rotation out of plane. This type of model is a step closer towards describing plane wave propagation in 3D microscale granular crystals. Here, the specific phenomena of shear to longitudinal mode conversion via second harmonic generation is studied theoretically and computationally for plane waves in a two-dimensional, adhesive, hexagonally close-packed microscale granular medium. We consider fundamental frequency plane waves in all three linear modes, which have infinite spatial extent and travel in one of the high-symmetry crystal directions. The generated second harmonic waves are longitudinal for all cases. For the lower transverse-rotational mode, an analytical expression for the second harmonic amplitude, which is derived using a successive approximations approach, reveals the presence of particular resonant and antiresonant wave numbers, the latter of which is prohibited if rotations are not included in the model. By simulating a lattice with adhesive contact force laws, we study the effectiveness of the theoretical analysis for non-resonant, resonant, and antiresonant cases. This work is applicable to the analysis of microscale and statically compressed macroscale granular media, and should inspire future

---

[1] The work in this chapter is adapted from Ref. [164].

studies on nonlinear two- and three-dimensional granular systems in which interparticle shear coupling and particle rotations play a significant role.

6.1 Introduction

As described in Ch. 1, models involving Hertzian normal contact (i.e. not having shear contact interactions) have been used to explore highly nonlinear mechanical wave propagation in uncompressed 2D granular crystals [4, 22, 23, 24, 25, 165]. While this type of model works well for uncompressed granular media, for statically compressed granular systems it is important to consider interparticle shear interactions and particle rotations. Several recent theoretical works, based on earlier discrete lattice models of elastic media [34], have introduced linear models of 2D [28, 29, 31] and 3D [30] granular crystals that account for interparticle shear interactions and particle rotations. These studies demonstrated how the additional degrees of freedom and modes of particle coupling can drastically influence the granular crystal dynamics, and yield unique effects such as the rotational waves experimentally observed in statically compressed macroscale granular systems [27]. Shear interactions and particle rotations also play a similarly important role in the emerging field of microscale granular crystals, as has been demonstrated theoretically in Chapters 4 - 5 and experimentally in another recent study [56], for quasi-1D microgranular systems in linear dynamical regimes.

In this work, we explore the nonlinear phenomena of second harmonic generation for plane waves traveling in a model of a 2D hexagonally-close packed lattice of microspheres, which includes interparticle adhesive effects, particle rotations, and elastic shear interactions.The spheres undergo 2D translations within the monolayer plane and rotations about an axis out of the plane. Second harmonic generation is a well-known phenomenon that has been studied extensively in nonlinear optics [166] and acoustics [167]. Past works have also examined second harmonic generation in 1D discrete granular chains [168, 169] and fluid-saturated granular media [170]. Using a successive approximations approach in the manner of Refs. [168, 169], we theoretically analyze the second harmonic generation for cases where the fundamental frequency (FF) wave is purely longitudinal or transverse-rotational in character, and find that the generated second harmonic waves are longitudinal in both scenarios. Such shear-to-longitudinal mode conversion via second harmonic generation has been previously studied in nonlinear elastic solids [171], observed experimentally in 3D granular packings [172, 173], and modeled in quasi-1D nonlinear phononic crystals [174]. We show that the second harmonic generated by a FF wave in the lower transverse-rotational mode may resonate or vanish for particular wavelengths, but the latter phenomenon is not predicted if rotations are excluded from the model. Finally, we compare our theoretical predictions with dynamic discrete element simulations of a microscale granular crystal. We find that the theoretical predictions are quantitatively accurate for non-resonant wavelengths, and provide qualitative understanding of the behavior at resonance. This paper extends the already rich body of work on nonlinear waves in 2- and 3D ordered granular media by exploring the interplay of multiple degrees of freedom and nonlinear particulate interactions.

6.2 Theory

6.2.1 Model

We consider a 2D, hexagonally close-packed lattice of spheres, as shown in Fig. 6.1(a). The interactions between spheres follow the Derjaguin-Muller-Toporov (DMT) adhesion model [3, 47], which includes Hertzian normal contact forces [11, 13], and a static adhesive force $F_{DMT} = 2\pi w R_c$ due to van der Waals interactions, where w is the work of adhesion [3], $R_c = R/2$ is the effective radius for two spheres in contact, and R is the microsphere radius. To describe the shear contact interactions, we use the Hertz-Mindlin model [12, 13], assuming no slip occurs in the contact surface. Because the characteristic sound speeds of waves in the lattice are much slower than those of the bulk material of the spheres, we treat the spheres as rigid bodies with radius R, mass m, and moment of inertia $I = (2/5)mR^2$, interacting via nonlinear spring elements [4]. In terms of the displacements $u_{j,k}$, $v_{j,k}$, and $\theta_{j,k}$, which represent horizontal, vertical, and angular displacements from equilibrium, respectively, the equations of motion of the sphere with index (j, k) are given by

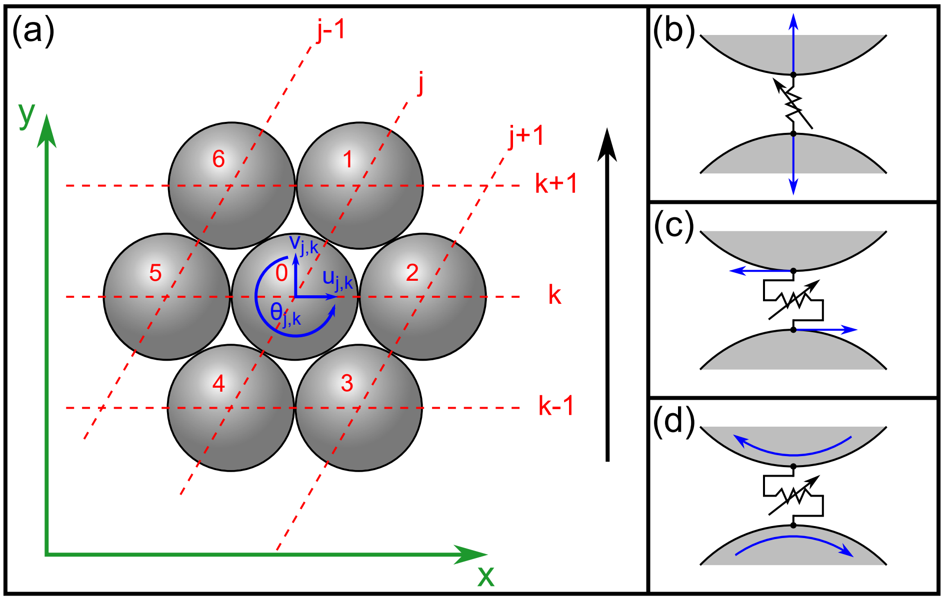

Figure 6.1: (a) Schematic of the model of a 2D, hexagonally close-packed granular membrane. The black arrow indicates the direction of wave propagation. (b-d) Illustrations of longitudinal, shear, and rotational motions activating normal and shear nonlinear contact springs.

$$\begin{aligned}
m\ddot{u}_{j,k} &= f_N(\bar{\delta}_2) - f_N(\bar{\delta}_5) + \frac{1}{2}(f_N(\bar{\delta}_1) - f_N(\bar{\delta}_4) + f_N(\bar{\delta}_3) - f_N(\bar{\delta}_6)) \\
&+ \frac{\sqrt{3}}{2}(f_S(\bar{\delta}_3) - f_S(\bar{\delta}_6) - f_S(\bar{\delta}_1) + f_S(\bar{\delta}_4)) \qquad (6.1) \\
m\ddot{v}_{j,k} &= f_S(\bar{\delta}_2) - f_S(\bar{\delta}_5) + \frac{1}{2}(f_S(\bar{\delta}_1) - f_S(\bar{\delta}_4) + f_S(\bar{\delta}_3) - f_S(\bar{\delta}_6)) \\
&+ \frac{\sqrt{3}}{2}(f_N(\bar{\delta}_1) - f_N(\bar{\delta}_4) - f_N(\bar{\delta}_3) + f_N(\bar{\delta}_6)) \qquad (6.2) \\
I\ddot{\theta}_{j,k} &= R\sum_l f_S(\bar{\delta}_l), \qquad (6.3)
\end{aligned}$$

where $\bar{\delta}_l = (\delta_{l,N}, \delta_{l,S})$ is the vector of relative normal and tangential displacements between particles labeled l and 0, as is defined in Sec. 6.5. The normal spring force (positive away from particle 0) and shear spring force (positive when inducing a counter-clockwise moment about particle 0) are given by

$$f_N(\bar{\delta}_l) = -\frac{4}{3}E^* R_c^{1/2} \left[\Delta_0 - \delta_{l,N}\right]_+^{3/2} \quad (6.4)$$

$$f_S(\bar{\delta}_l) = 8G^* R_c^{1/2} \delta_{l,S} \left[\Delta_0 - \delta_{l,N}\right]_+^{1/2}, \quad (6.5)$$

respectively. Here, $\Delta_0 = [3F_{DMT}/(4E^* R_c^{1/2})]^{2/3}$ is the static overlap due to adhesion, and $E^* = E/(2(1-\nu^2))$ and $G^* = G/(2(2-\nu))$ are the effective elastic and shear moduli, respectively, of a solid with elastic modulus E, shear modulus G, and Poisson's ratio ν. As shown in Fig. 6.1(b-d), the normal springs are activated by axial sphere displacements, while the shear springs can be activated by both transverse displacements and rotations.

We expand the nonlinear spring forces given by Eqs. (6.4) and (6.5) in Taylor series up to quadratic order as

$$f_N(\bar{\delta}_l) \simeq -A\Delta_0^{3/2} + \frac{3}{2}A\Delta_0^{1/2}\delta_{l,N} - \frac{3}{8}A\Delta_0^{-1/2}\delta_{l,N}^2 + \mathcal{O}(\delta_{l,N}^3) \quad (6.6)$$

$$f_S(\bar{\delta}_l) \simeq B\Delta_0^{1/2}\delta_{l,S} - \frac{1}{2}B\Delta_0^{-1/2}\delta_{l,S}\delta_{l,N} + \mathcal{O}(\delta_{l,S}\delta_{l,N}^2), \quad (6.7)$$

where $A = (4/3)E^* R_c^{1/2}$ and $B = 8G^* R_c^{1/2}$. We name the linear and quadratic stiffnesses $k_1 = (3/2)A\Delta_0^{1/2}$, $g_1 = B\Delta_0^{1/2}$, $k_2 = -(3/8)A\Delta_0^{-1/2}$, and $g_2 = -(1/2)B\Delta_0^{-1/2}$, and define the nonlinearity parameter $\epsilon = (3/2)D_0(g_2 + 3k_2)/(g1 + 3k_1)$.

We restrict our analysis to plane waves traveling in the positive y direction; hence, the equations of motion take the form of an effective 1D lattice with three degrees of freedom, and we adopt the single index n, where $n = k$. We also transform the system to dimensionless variables $p = v/D_0$, $q = -u/D_0$, $\phi = R\theta/D_0$, where D_0 is a characteristic displacement amplitude, and $\tau = t\omega_L$, where $\omega_L = 2\sqrt{(g_1 + 3k_1)/(2m)}$ is the cutoff frequency for longitudinal waves in the linearized system. Finally, the equations of motion are reduced to a simpler form, which is valid for small nonlinearity ($\epsilon << 1$):

$$\begin{aligned} p_n'' &= \frac{1}{4}\mathcal{D}_2 p_n + \epsilon[\frac{1}{8}(\mathcal{D}_2 p_n)(\mathcal{D}_1 p_n) - \frac{1}{6}\alpha(\mathcal{D}_2 q_n)(\mathcal{D}_1 q_n) \\ &+ \frac{1}{3\sqrt{3}}\beta(\phi_n \mathcal{D}_2 q_n - q_n \mathcal{D}_3 \phi_n + \mathcal{D}_3(q_n \phi_n))] \end{aligned} \tag{6.8}$$

$$\begin{aligned} q_n'' &= \frac{\mu_1}{4}\mathcal{D}_2 q_n - \frac{\sqrt{3}\mu_2}{2}\mathcal{D}_1 \phi_n - \frac{\epsilon}{4}[\gamma(p_n \mathcal{D}_1 q_n + q_n \mathcal{D}_1 p_n - \mathcal{D}_1(q_n p_n)) \\ &+ \sqrt{3}\beta(-p_n \mathcal{D}_4 \phi_n + \phi_n \mathcal{D}_3 p_n + \mathcal{D}_3(\phi_n p_n))] \end{aligned} \tag{6.9}$$

$$\begin{aligned} \phi_n'' &= \frac{\mu_2}{2\tilde{I}}[-2(\mathcal{D}_4 \phi_n + 2\phi_n) + \sqrt{3}\mathcal{D}_1 q_n] \\ &+ \epsilon\frac{\beta}{2\tilde{I}}[\frac{1}{\sqrt{3}}(-q_n \mathcal{D}_2 p_n - p_n \mathcal{D}_3 q_n + \mathcal{D}_3(q_n p_n)) + (p_n \mathcal{D}_1 \phi_n - \phi_n \mathcal{D}_1 p_n - \mathcal{D}_1(\phi_n p_n))], \end{aligned} \tag{6.10}$$

where the $(\cdot)''$ notation denotes the second derivative with respect to τ, the parameters $\mu_1 = (3g_1 + k_1)/(g_1 + 3k_1)$, $\mu_2 = g_1/(g_1 + 3k_1)$, $\alpha = (g_2 - k_2)/(g_2 + 3k_2)$, $\beta = g_2/(g_2 + 3k_2)$, $\gamma = (g_2 + k_2)/(g_2 + 3k_2)$, and $\tilde{I} = I/(mR^2)$, and the operators $\mathcal{D}_1(\cdot)_n = (\cdot)_{n+1} - (\cdot)_{n-1}$, $\mathcal{D}_2(\cdot)_n = (\cdot)_{n+1} - 2(\cdot)_n + (\cdot)_{n-1}$, $\mathcal{D}_3(\cdot)_n = (\cdot)_{n+1} + (\cdot)_{n-1}$, and $\mathcal{D}_4(\cdot)_n = (\cdot)_{n+1} + 2(\cdot)_n + (\cdot)_{n-1}$. We note that the rescaled variables p_n and q_n represent displacements parallel and transverse to the direction of propagation, respectively.

In all numerical results that follow, we use, as a case study, the geometric and material properties of 1 μm silica spheres: elastic constants $E = 73$ GPa and $\nu = 0.17$ [154], and work of adhesion $w = 0.063$ J/m^2 [3].

6.2.2 Quasi-linear Regime

In the limit of vanishing amplitude, the dynamics are linear, and the medium behaves as the 2D hexagonal lattice studied in [34] (neglecting rotational springs). Using Eqs. (6.8) - (6.10) with $\epsilon = 0$, we derive the dispersion relation, and find three modes, as shown in Fig. 6.2(a): one that involves only longitudinal motion, and two involving coupled transverse and rotational motions [31, 34]. The dispersion equations are:

$$\Omega = \sin\left(\frac{\xi}{2}\right) \tag{6.11}$$

$$\det(M) = 0, \tag{6.12}$$

where ξ and Ω are the dimensionless wave number and angular frequency (normalized to the lattice spacing in the y direction and longitudinal mode cutoff frequency [17], respectively), and the transverse-rotational dispersion matrix M is given by

$$M = \begin{bmatrix} \frac{\mu_1}{2}[1-\cos(\xi)] - \Omega^2 & \sqrt{3}i\mu_2 \sin(\xi) \\ -\sqrt{3}i\mu_2 \sin(\xi) & 2\mu_2[2+\cos(\xi)] - \tilde{I}\Omega^2 \end{bmatrix}. \tag{6.13}$$

Following conventions used in previous works [27, 30], we denote the longitudinal mode "L," and the lower and upper transverse-rotational modes as "TR" and "RT," respectively, where the first letter corresponds to the predominant displacement of each mode. While models for 3D hexagonally close-packed granular crystals [30], which include shear interactions and particle rotations, predict faster wave speeds, due to additional interparticle coupling terms, and additional plane wave modes due to periodically alternating layers (including purely rotational modes), we suggest that our model may also be utilized to gain qualitative understanding of certain 3D scenarios. This is due to the similarity of acoustic-type L and TR modes, as well as one of the optical-type RT modes, present in both 2D and 3D systems.

6.2.3 Weakly-nonlinear Regime: Second Harmonic Generation and Nonlinear Mode Conversion

For $|\epsilon| << 1$, the nonlinear response can be predicted using a successive-approximations approach, in the manner of Refs. [168, 169], where we represent the displacements as power series[2] in ϵ:

---

[2] Here we use *regular* perturbation theory, which is sufficient for the behavior we wish to model.

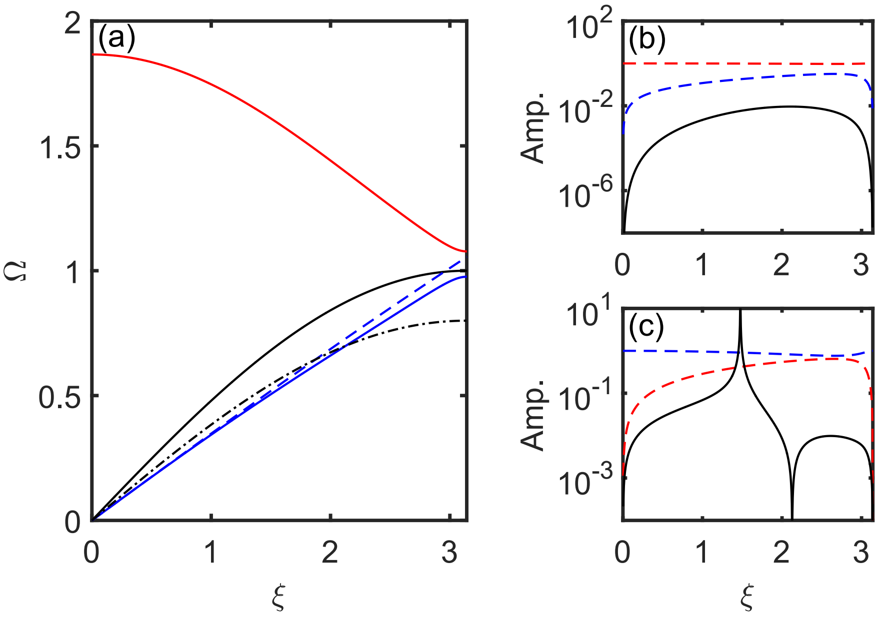

Figure 6.2: (a) Dispersion of plane waves traveling in the direction indicated in Fig. 1(a). Longitudinal (black), TR (blue), and RT (red) modes are denoted by the solid lines. The blue dashed curve is a frequency- and wave number-doubled representation of the TR mode, which is shown to intersect with the L mode. The black dash-dotted curve defines the antiresonance condition, wherein its intersection with the TR branch denotes the antiresonance frequency and wavenumber. (b,c) Amplitudes of second harmonic longitudinal waves (black solid curves) generated from fundamental waves in the RT and TR modes, respectively. Blue and red dashed curves show the transverse and rotational displacements, normalized such that the sum of squares is unity. The second harmonic amplitudes are normalized by the small parameter ϵ.

$$p_n(\tau) = P_{0,n}(\tau) + \epsilon P_{1,n}(\tau) + \epsilon^2 P_{2,n}(\tau) + \ldots \tag{6.14}$$

$$q_n(\tau) = Q_{0,n}(\tau) + \epsilon Q_{1,n}(\tau) + \epsilon^2 Q_{2,n}(\tau) + \ldots \tag{6.15}$$

$$\phi_n(\tau) = \Phi_{0,n}(\tau) + \epsilon \Phi_{1,n}(\tau) + \epsilon^2 \Phi_{2,n}(\tau) + \ldots, \tag{6.16}$$

and explore second harmonic generation in the granular medium, separately considering the cases of TR/RT and L modes as FF waves. While previous works employing this approach have focused on finite-length and semi-infinite lattices [168, 169] with a harmonic boundary condition, we consider an infinite lattice, and use a single plane wave of infinite extent that travels in the positive-n direction as the initial condition; that is,

$$\begin{aligned} p_n(0) &= P_{0,n}(0) = \tilde{P}_0 e^{i(\xi n)}, && (6.17) \\ p'_n(0) &= P'_{0,n}(0) = -i\Omega \tilde{P}_0 e^{i(\xi n)}, && (6.18) \end{aligned}$$

where $\tilde{P}_0$ is a constant amplitude, with similar expressions for the other displacements. Thus, the second harmonic response is a function of wave number. This configuration closely resembles the conditions of several recent experiments on microscale granular crystals [8, 9, 55] that utilize the laser-induced transient grating spectroscopy technique [10], which excite waves with specific, defined wavelengths via the projection of a spatially periodic optical interference pattern.

We note that, for the expansions given by Eqs. (6.14) - (6.16) to be valid, each function P_0, P_1, etc. should be of order $\mathcal{O}(1)$; this imposes limits on the range of wave numbers for which the analysis is valid, as will be discussed later.

TR and RT Modes as Fundamental Waves

We first consider TR and RT modes as FF waves, i.e.

$$\begin{aligned} p_n(0) &= p'_n(0) = 0 && (6.19) \\ q_n(0) &= Q_{0,n}(0) = \tilde{Q}_0 e^{i(\xi n - \Omega\tau)}|_{\tau=0}, q'_n(0) = -i\Omega q_n(0) && (6.20) \\ \phi_n(0) &= \Phi_{0,n}(0) = \tilde{\Phi}_0 e^{i(\xi n - \Omega\tau)}|_{\tau=0}, \phi'_n(0) = -i\Omega \phi_n(0). && (6.21) \end{aligned}$$

We proceed by substituting the power series given by Eqs. (6.14) - (6.16) into Eqs. (6.8) - (6.10). At order $\mathcal{O}(\epsilon^0)$, we find that $P_{0,n}$, $Q_{0,n}$, and $\Phi_{0,n}$ must be plane waves satisfying the linear dispersion relations given by Eqs. (6.11) and (6.12). To satisfy the initial condition given by Eq. (6.19), it follows that $P_{0,n}(\tau) = 0$. Furthermore, the ratio of amplitudes of the $Q_{0,n}$ and $\Phi_{0,n}$ plane waves is constrained; in particular, a vector composed of these two amplitudes must be an eigenvector of the dispersion matrix M corresponding to the eigenvalues ξ and Ω. Because we have chosen a plane wave in the TR or RT mode as the initial condition, this constraint is trivially satisfied.

At order $\mathcal{O}(\epsilon^1)$, we find

$$\begin{aligned}P''_{1,n} - &\frac{1}{4}(P_{1,n+1} - 2P_{1,n} + P_{1,n-1}) = \\ &\frac{1}{8}(\mathcal{D}_2 P_{0,n})(\mathcal{D}_1 P_{0,n}) - \frac{1}{6}\alpha(\mathcal{D}_2 Q_{0,n})(\mathcal{D}_1 Q_{0,n}) \\ &+\frac{1}{3\sqrt{3}}\beta(\Phi_{0,n}\mathcal{D}_2 Q_{0,n} - Q_{0,n}\mathcal{D}_3\Phi_{0,n} + \mathcal{D}_3(Q_{0,n}\Phi_{0,n}))\end{aligned} \tag{6.22}$$

$$\begin{aligned}Q''_{1,n} - &\frac{\mu_1}{4}\mathcal{D}_2 Q_{1,n} + \frac{\sqrt{3}\mu_2}{2}\mathcal{D}_1\Phi_{1,n} = \\ &-\frac{1}{4}[\gamma\,(P_{0,n}\mathcal{D}_1 Q_{0,n} + Q_{0,n}\mathcal{D}_1 P_{0,n} - \mathcal{D}_1(Q_{0,n}P_{0,n})) \\ &+\sqrt{3}\beta(-P_{0,n}\mathcal{D}_4\Phi_{0,n} + \Phi_{0,n}\mathcal{D}_3 P_{0,n} + \mathcal{D}_3(\Phi_{0,n}P_{0,n}))]\end{aligned} \tag{6.23}$$

$$\begin{aligned}\Phi''_{1,n} - &\frac{\mu_2}{2\tilde{I}}[-2(\mathcal{D}_4\Phi_{1,n} + 2\Phi_{1,n}) + \sqrt{3}\mathcal{D}_1 Q_{1,n}] = \\ &\frac{\beta}{2\tilde{I}}[\frac{1}{\sqrt{3}}(-Q_{0,n}\mathcal{D}_2 P_{0,n} - P_{0,n}\mathcal{D}_3 Q_{0,n} + \mathcal{D}_3(Q_{0,n}P_{0,n})) \\ &+(P_{0,n}\mathcal{D}_1\Phi_{0,n} - \Phi_{0,n}\mathcal{D}_1 P_{0,n} - \mathcal{D}_1(\Phi_{0,n}P_{0,n}))].\end{aligned} \tag{6.24}$$

Since $P_{0,n} = 0$, the right-hand side of Eq. (6.22) is composed of quadratic products of $Q_{0,n}$ and $\Phi_{0,n}$, while the right-hand sides of Eqs. (6.23) and (6.24) vanish. Thus, the second harmonics at order $\mathcal{O}(\epsilon^1)$ generated by fundamental plane waves in the TR and RT modes are purely longitudinal in character. Furthermore, from the initial conditions given by Eqs. (6.20) and (6.21), it follows that $Q_{1,n}(\tau) = \Phi_{1,n}(\tau) = 0$.

We derive an expression for $P_{1,n}(\tau)$ by seeking a solution of the form

$$P_{1,n}(\tau) = \tilde{P}_{1,n}^{(+)} e^{i(2\xi n - \Omega(2\xi)\tau)} + \tilde{P}_{1,n}^{(-)} e^{i(2\xi n + \Omega(2\xi)\tau)} + \tilde{P}_{1,n}^{(TR)} e^{i(2\xi n - 2\Omega\tau)}, \tag{6.25}$$

where $\Omega(2\xi)$ is found using Eq. (6.11). The first two terms of ansatz given by Eq. (6.25) are the homogeneous part of the solution, with the $(+)$ and $(-)$ superscripts corresponding to positive- and negative-n traveling waves, respectively. The third term is generated by the FF wave terms on the right-hand side of Eq. (6.22), and the superscript (TR) signifies that the generating FF wave is in either transverse-rotational mode. To derive an expression for the amplitude of the generated second harmonic wave, we substitute into Eq. (6.22) the expressions $P_{1,n} = \tilde{P}_{1,n}^{(TR)} e^{i(2\xi n - 2\Omega\tau)}$, $Q_{0,n} = \tilde{Q}_0 e^{i(\xi n - \Omega\tau)}$ and $\Phi_{0,n} = \tilde{\Phi}_0 e^{i(\xi n - \Omega\tau)}$, and adopt the convention that the FF amplitudes $\tilde{Q}_0$ and $\tilde{\Phi}_0$ have been normalized, such that the sum of their squares is unity. After simplification, we find an expression for the amplitude of the longitudinal second harmonic wave that depends on the amplitudes of the FF waves (either TR or RT), as well as the wave number:

$$\tilde{P}_{1,n}^{(TR)}(\xi) = \frac{\frac{4}{3}\sin(\xi)\tilde{Q}_0 \left[-\frac{\beta}{\sqrt{3}} \sin(\xi)\tilde{\Phi}_0 + i\alpha \sin^2(\xi/2)\tilde{Q}_0 \right]}{\sin^2(\xi) - (2\Omega)^2}, \tag{6.26}$$

where the ratio $\tilde{Q}_0/\tilde{\Phi}_0$ is a function of ξ. This expression is applicable for FF waves in both the TR and RT modes, and is plotted for each case in Fig. 6.2(b-c).

In Fig. 6.2(c), we observe a resonance near $\xi \simeq \pi/2$; this arises because the generated second harmonic wave of the TR mode (i.e. the third term of Eq. (6.25)) has a wave number and frequency that intersect the L mode, as shown in Fig. 6.2(a). Such resonances indicate perfect phase matching [166, 167] between the generated and homogeneous second harmonic waves, and the conversion of energy from the TR mode to L the mode is most efficient at this wave number. Since the value of $\tilde{P}_{1,n}^{(TR)}$ near the resonance is larger than $\mathcal{O}(1)$, the expansion given by Eq. (6.14) is no longer valid, as the generated harmonics would grow to the same order of magnitude as the FF wave[3]. The wave number at which this resonance occurs depends on the mass and stiffness properties of the lattice, but the resonance must exist in

---

[3] Multi-scale perturbation theory is required for an accurate solution in this case.

our model, because the generated second harmonic wave will always possess an intersection with the L mode, though it may occur outside the first Brillouin zone. In the limiting case of infinitely large rotational inertia or vanishing shear contact stiffness (i.e. neglecting rotations or shear interactions), the resonance still exists, albeit at a different wave number.

We also note the presence of an antiresonance in Fig. 6.2(c); this implies that the quadratic nonlinearities vanish at order $\mathcal{O}(\epsilon^1)$, for a particular wavelength. Near the antiresonance, the harmonics generated by higher-order nonlinearities can be of the same order of magnitude as the second harmonic waves; thus, these nonlinearities would need to be included in Eqs. (6.8) - (6.10), and additional terms of the expansions given by Eqs. (6.14) - (6.16) should be included, to obtain accurate results. The wave number of this antiresonance is dependent on mass and stiffness properties, but is not guaranteed to exist for arbitrary parameter values; indeed, the numerator of Eq. (6.26) is not guaranteed to vanish, except for values of ξ that are integer multiples of π (corresponding to the edges of the Brillouin zones). We note that the antiresonance cannot exist in the limit of infinitely large rotational inertia, i.e. $\tilde{\Phi}_0 = 0$, which highlights the importance of particle rotations in our model.

Considering finite rotational inertia, we derive a condition on the wave number ξ and frequency ω that must be satisfied at the antiresonance. The dispersion relation given by Eq. (6.12) is a solvability condition of the matrix equation

$$M \begin{bmatrix} \tilde{Q}_0 \\ \tilde{\Phi}_0 \end{bmatrix} = \begin{bmatrix} 0 \\ 0 \end{bmatrix}. \tag{6.27}$$

Thus, by manipulating either of the two scalar equations in this system, the ratio $\tilde{\Phi}_0/\tilde{Q}_0$ can be written in terms of ξ, Ω, and lattice stiffness and mass parameters. We find

$$\frac{\tilde{\Phi}_0}{\tilde{Q}_0} = -\frac{(\mu_1/2)(1-\cos(\xi)) - \Omega^2}{\sqrt{3}i\mu_2 \sin(\xi)}. \tag{6.28}$$

By substituting Eq. (6.28) into the bracketed term in the numerator of Eq. (6.26), equating this expression to zero, and rearranging, we derive the expression

$$\Omega = \sin\left(\frac{\xi}{2}\right)\sqrt{\mu_1 - 3\mu_2\frac{\alpha}{\beta}}, \tag{6.29}$$

which defines a condition for the antiresonance. Thus, if the TR dispersion branch intersects the curve defined by Eq. (6.29), the antiresonance exists at the corresponding wave number and frequency, as shown in Fig. 6.2(a). Furthermore, when the Hertz-Mindlin contact model is assumed, the stiffness parameters contained in Eq. (6.29) are all related by Poisson's ratio ν [13]. By manipulating Eqs. (6.12) and (6.29), it can be shown that the TR mode has a higher cutoff frequency at $\xi = \pi$ than the curve defined by Eq. (6.29), but has a lesser slope at the origin. It follows that the intersection is guaranteed to exist for physically realizable materials (i.e. $-1 \leq \nu \leq 0.5$).

From these resonance and antiresonance conditions, it follows that when the FF wave is in the RT mode, neither is permitted because the frequency of the generated second harmonic wave is always above the cutoff frequency of the L mode. The effect of the cutoff frequency can also be seen by comparing the generated second harmonic amplitudes for the TR and RT modes. As shown in Fig. 6.2(b,c), for wave numbers below the resonance, the generated second harmonic amplitude $\tilde{P}_{1,n}^{(TR)}$ of FF waves in the RT mode is generally lower than that of the TR mode, while for wave numbers above the resonance, the amplitudes are generally of similar order (excepting the effects of the antiresonance). This is due to the relative proximities of the generated second harmonic waves to the propagation band of the L mode: as shown in Fig. 6.2(a), at low wave numbers, the generated second harmonic waves from the RT mode are far above the cutoff frequency of the L mode, while those of the TR mode are in the propagation band. Above the resonance, both the TR and RT modes generate second harmonic waves above the cutoff, but have similar proximity to the pass band.

Enforcing the initial condition given by Eq. (6.19), which implies that there is no second harmonic at time $\tau = 0$ (i.e. $P_{1,n}(0) = P'_{1,n}(0) = 0$), we derive the amplitudes of the homogeneous terms as a function of the generated second harmonic amplitude:

$$\tilde{P}_{1,n}^{(+)} = -\frac{\Omega(2\xi)+2\Omega}{2\Omega(2\xi)}\tilde{P}_{1,n}^{(TR)} \tag{6.30}$$

$$\tilde{P}_{1,n}^{(-)} = -\frac{\Omega(2\xi)-2\Omega}{2\Omega(2\xi)}\tilde{P}_{1,n}^{(TR)}. \tag{6.31}$$

We note that, for an experimental setup, the FF wave would contain components traveling in both the positive and negative directions. In a region where these two components interact, two additional longitudinal second harmonic waves would be present: a negative-n traveling wave analogous to the third term of Eq. (6.25), which also has the same dependence on ξ, and a standing wave with wave number 2ξ and vanishing frequency, which arises due to the interaction between FF waves.

L Mode as Fundamental Wave

We now conduct a similar analysis using a plane wave in the L mode as the FF wave, i.e.

$$p_n(0) = P_{0,n}(0) = \tilde{P}_0 e^{i(\xi n - \Omega\tau)}|_{\tau=0}, \quad p_n'(0) = -i\Omega p_n(0) \tag{6.32}$$

$$q_n(0) = \phi_n(0) = 0, \quad q_n'(0) = \phi_n'(0) = 0. \tag{6.33}$$

By inspecting the quadratic terms in Eqs. (6.9) - (6.10), we observe that no motion in the transverse and rotational displacements can be generated via nonlinearity, because these terms are all products containing q_n and ϕ_n. Thus, the remaining equation of motion given by Eq. (6.8) reduces to a form that is mathematically equivalent to that in [169], while the boundary conditions differ.

After substituting the power series of Eq. (6.14) into Eq. (6.8), we equate the coefficients of order $\mathcal{O}(\epsilon^0)$, seek solutions of the form $P_{0,n}(\tau) = \tilde{P}_0 e^{i(\xi n - \Omega\tau)}$, and find that $P_{0,n}(\tau)$ satisfies Eq. (6.11), the dispersion relation of the L mode. At order $\mathcal{O}(\epsilon^1)$, we find

$$P_{1,n}'' - \frac{1}{4}(P_{1,n+1} - 2P_{1,n} + P_{1,n-1}) = \frac{1}{8}(P_{0,n+1} - 2P_{0,n} + P_{0,n-1})(P_{0,n+1} - P_{0,n-1}). \tag{6.34}$$

This is a linear equation for $P_{1,n}$ with a generation term that is quadratic in $P_{0,n}$. Thus, we seek a solution as the sum of homogeneous and generated second harmonic waves in the form

$$P_{1,n}(\tau) = \tilde{P}^{(+)}_{1,n} e^{i(2\xi n - \Omega(2\xi)\tau)} + \tilde{P}^{(-)}_{1,n} e^{i(2\xi n + \Omega(2\xi)\tau)} + \tilde{P}^{(L)}_{1,n} e^{i(2\xi n - 2\Omega\tau)}, \tag{6.35}$$

where each term is analogous to the corresponding term in Eq. (6.25). Here, the superscript (L) signifies that the generating FF wave belongs to the L mode. The amplitude of the generated term $\tilde{P}^{(L)}_{1,n}$, which is analogous to Eq. (6.26), can be derived as in [169], where a detailed analysis has been performed. While the system considered in [169] is 1D and clearly not identical to our own, the calculation of $\tilde{P}^{(L)}_{1,n}$ is mathematically equivalent.

Because this solution must satisfy the initial conditions given by Eqs. (6.17) and (6.18), the amplitudes of the homogeneous terms may by derived in the same way as for FF waves in the TR and RT modes, and appear in the same form as Eqs. (6.30) and (6.31), with the exception that the superscript (TR) must be replaced by (L).

6.3 Simulations

6.3.1 Numerical Setup

To examine the validity of our theoretical analysis with a complete Hertzian nonlinearity, we simulate second harmonic generation from an FF wave in the TR mode by numerically solving Eqs. (6.1) - (6.3) for $1 < n < 201$. We use initial conditions of the form given in Eqs. (6.20) - (6.21), with fixed boundaries. For each case, we probe the response of the central lattice site ($n = 101$), and end the simulation before disturbances caused by the boundaries reach this site. We present the results in terms of the normalized variables $p_{101}(\tau)$, $q_{101}(\tau)$, and $\phi_{101}(\tau)$.

6.3.2 Numerical Results

As shown in Fig. (6.3), we simulate the lattice using three wave numbers, each representing a qualitatively different case: 1) $\xi_1 = 0.802$, which is far from the resonance and antiresonance;

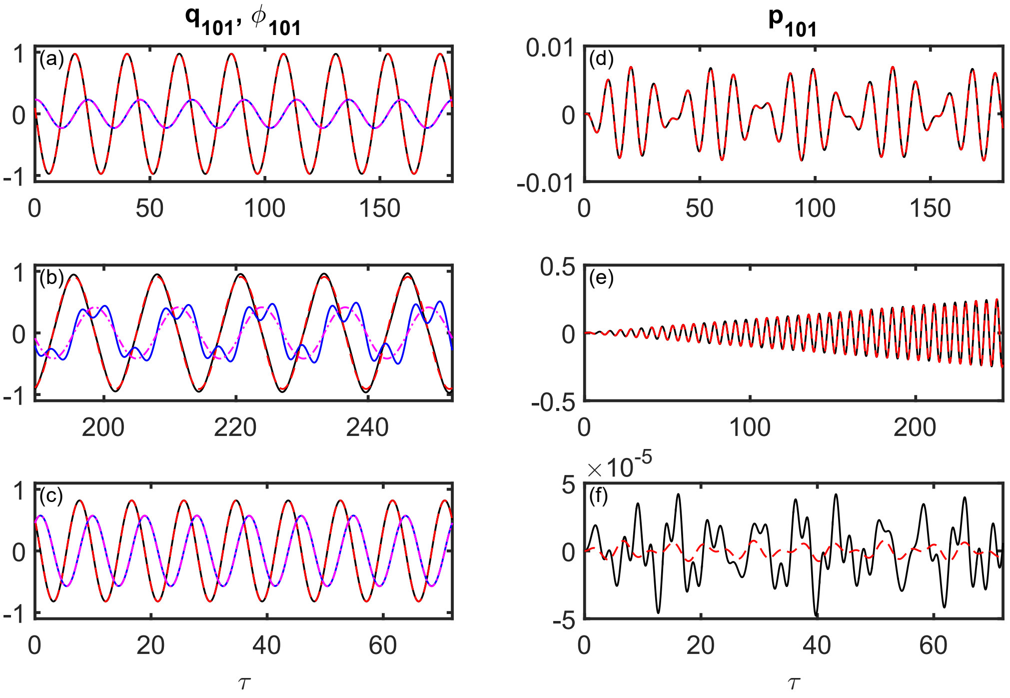

Figure 6.3: (a-c) Transverse and rotational displacements for $\xi_1 = 0.80$, $\xi_2 = 1.475$, and $\xi_3 = 2.127$. Black and blue solid lines correspond to simulated transverse and rotational displacements, while red dashed and magenta dash-dotted lines show the corresponding theoretical predictions. (d-f) Simulated (black solid) and theoretical (red dashed) curves showing longitudinal displacements for the wave numbers of (a-c).

2) $\xi_2 = 1.475$, which is approximately the resonant wave number; and 3) $\xi_3 = 2.127$, which is approximately the antiresonant wave number. We have chosen the characteristic amplitude $D_0 = 0.2\Delta_0$, which results in the nonlinearity parameter $\epsilon_{sim} \approx -0.1$.

For case 1), the perturbation analysis is valid (note from Fig. 6.2(c) that $\tilde{P}_{1,n}^{(TR)} \simeq \mathcal{O}(1)$), and the simulated time histories are well-approximated by the theoretical predictions, as shown in Fig. 6.3(a,d). In Fig. 6.3(d), it can be seen that the second harmonic amplitude exhibits "beating" at a frequency $\Omega_{beat} = \Omega(2\xi) - 2\Omega$; this phenomenon is a well-known characteristic of second harmonic generation [166, 169]. For case 2), the oscillations of p_{101} grow linearly in τ, as shown in Fig. 6.3(e). While the theoretical prediction for p_{101}

appears to match the simulation reasonably well, it is evident from Fig. 6.3(b) that there is significant error in q_{101} and ϕ_{101}; in fact, the second harmonic is visibly present in the simulated signals. This is because, while the approximation works well for small τ, the generated second harmonic longitudinal wave eventually reaches the same order of magnitude as the FF wave, thereby violating the assumption of weak nonlinearity. While even-order harmonics are not common for transverse waves in elastic media [171], they are supported in our model, because the normal springs (and therefore the even-order nonlinearity necessary for second harmonic generation) are activated by transverse motion in a hexagonally close-packed granular crystal. For case 3), the predictions for q_{101} and ϕ_{101} are accurate, as shown in Fig. 6.3(b). However, as shown in Fig. 6.3(f), there is significant error in p_{101} generated by higher-order nonlinearities, which have larger contributions than order $\mathcal{O}(\epsilon^1)$.

6.4 Conclusion

In this work, we have analyzed shear to longitudinal mode conversion via second harmonic generation for plane waves in a 2D, adhesive, hexagonally close-packed microscale granular crystal, accounting for translational and rotational degrees of freedom, as well as normal and shear contact interactions. In the case of a FF wave in the L mode, we show that the generated second harmonic is also longitudinal, and can be described using the same equations as for a 1D chain studied in earlier works. For the case where the lowest TR mode is treated as the FF wave, the generated second harmonic wave is longitudinal, and an analytical expression for the second harmonic amplitude reveals the presence of resonant and antiresonant wave numbers. This antiresonance is not predicted if rotations are excluded from the model, which demonstrates that, while the TR mode is predominantly transverse for most wavelengths, particle rotations produce a qualitative change in the nonlinear lattice dynamics. By simulating a lattice with DMT and Hertz-Mindlin particle interactions, we verify the accuracy of the theoretical analysis for a non-resonant case, and find that it effectively predicts the qualitative behavior of the resonant and antiresonant cases. Future generalizations of this work to off-symmetry directions of propagation and extension to strongly nonlinear dynamical regimes may yield particularly interesting phenomena. This work is particularly suitable for the analysis of both microscale granular crystals, which are naturally precompressed by adhesive forces, and statically compressed granular crystals with macroscale particles. We expect that future studies of such 2- and 3D granular media will yield unique dynamics stemming from the interplay of interparticle shear coupling and particle rotations with highly nonlinear phenomena such as solitary waves [4] or hysteretic contact mechanics [175].

6.5 Contact Spring Displacements[4]

The normal component of the relative displacement between the particles labeled 0 and l (see Fig. 6.1), denoted $\delta_{l,N}$, is considered positive with increasing distance between the particle centers. The normal relative displacements are given by

$$\begin{aligned}
\delta_{1,N} &= \frac{u_1-u_0}{2}+\frac{\sqrt{3}(v_1-v_0)}{2} \\
\delta_{2,N} &= u_2-u_0 \\
\delta_{3,N} &= \frac{u_3-u_0}{2}-\frac{\sqrt{3}(v_3-v_0)}{2} \\
\delta_{4,N} &= -\frac{u_4-u_0}{2}-\frac{\sqrt{3}(v_4-v_0)}{2} \\
\delta_{5,N} &= -(u_5-u_0) \\
\delta_{6,N} &= -\frac{u_6-u_0}{2}+\frac{\sqrt{3}(v_6-v_0)}{2}.
\end{aligned}$$

---

[4] This section is adapted from the appendix of Ref. [164].

The tangential component of the relative displacement, denoted $\delta_{l,S}$, is considered positive if the shear force $f_S(\bar{\delta})$ (which is proportional to $\delta_{l,S}$) induces a counterclockwise moment about particle 0. The tangential displacements are given by

$$\begin{aligned}
\delta_{1,S} &= \frac{-\sqrt{3}(u_1 - u_0)}{2} + \frac{v_1 - v_0}{2} - R(\theta_1 + \theta_0) \\
\delta_{2,S} &= v_2 - v_0 - R(\theta_2 + \theta_0) \\
\delta_{3,S} &= \frac{\sqrt{3}(u_3 - u_0)}{2} + \frac{v_3 - v_0}{2} - R(\theta_3 + \theta_0) \\
\delta_{4,S} &= \frac{\sqrt{3}(u_4 - u_0)}{2} - \frac{v_4 - v_0}{2} - R(\theta_4 + \theta_0) \\
\delta_{5,S} &= -(v_5 - v_0) - R(\theta_5 + \theta_0) \\
\delta_{6,S} &= -\frac{\sqrt{3}(u_6 - u_0)}{2} - \frac{v_6 - v_0}{2} - R(\theta_6 + \theta_0).
\end{aligned}$$

Chapter 7

ENERGY PARTITION IN A 2D MICROSCALE GRANULAR CRYSTAL SUBJECT TO AN IMPULSIVE POINT LOAD: MULTIBODY DYNAMICS SIMULATION

7.1 Introduction

Much like classical elastic solids, 2- and 3D granular media support bulk longitudinal and shear waves [28, 29, 34, 176, 177], as well as Rayleigh-like SAWs [32, 178, 179]. A recent theoretical work analyzed the dispersion of SAWs in a semi-infinite, 2D, precompressed GC with square packing [32]. Given an excitation in the form of an impulsive point source at the surface of an elastic halfspace, all bulk and surface acoustic modes can be excited. In past works, analytical solutions to this problem have been found via a Green's function approach for linear elastic, isotropic [180] and anisotropic [181, 182] halfspaces. For the isotropic case, the fraction of the total energy partitioned into each mode was also found analytically [180].

In this chapter, the amplitude dependence of energy partition and wave speed in a 2D, microscale GC with hexagonal close-packing is investigated via multibody dynamics simulations. In contrast to Ch. 6, where we studied bulk plane waves in a 2D GC with infinite spatial extent, the GC studied here has a free interface subjected to an impulsive point source. Point loading of 2D GCs has been studied previously [24, 25]; however, the GCs in these works differs from ours in that they were uncompressed, so they always operated in the strongly nonlinear regime, and had negligible shear interactions. We note that a point source in a 2D medium approximately corresponds to the behavior of a line source in a 3D medium. We analyze the partition of energy by observing the components of kinetic energy in longitudinal, transverse, and rotational motions throughout the spatial domain, and find qualitative changes as a function of impulse amplitude. We observe an increase in longitudinal bulk wave speed with increasing excitation amplitude, which agrees qualitatively with existing theory, as well as a non-monotonic dependence of longitudinal surface wave speed on amplitude. Finally, we observe non-smooth variations of particle velocity at high excitation amplitudes, which we attribute to severed contacts near the excitation point. This work gives insight into the behavior of waves in GCs with localized excitation sources, which should be applicable to future experiments on microscale GC multilayers, and also extends the growing body of work on energy partition in nonlinear lattices.

7.2 Multibody Dynamics Simulation

For the simulations in this chapter, we use CHRONO, an open-source physics engine for multibody dynamics simulation (MDS) [183]. The Hertz, Hertz-Mindlin, and DMT models have been implemented in the CHRONO framework for normal contact, shear contact, and adhesion, respectively. CHRONO was chosen over the MATLAB-based methods used in Chapters 3-6 because it is accurate for a more general simulation setting, in which the deformation is large enough for contacts to be broken.

The numerical simulations of GCs in Chapters 3-6 were all performed on quasi-1D systems and did not involve any loss of contact (i.e. it was assumed that the relative interparticle displacements did not exceed the static overlap). Based on these assumptions, the geometric nonlinearity associated with large particle displacements could be neglected. However, when simulating GCs at amplitudes that may cause loss and initiation of contact, these assumptions are no longer valid.

To see this, consider two contacting spheres, as shown in position I of Fig. 7.1. After some time, suppose these two spheres have undergone some relative tangential displacement (with or without rotation), as shown in position II of Fig. 7.1, and are then pulled apart, resulting in loss of contact, as shown in position III. If the spheres are placed back in contact, with their centers in the same positions as in position III, there will be no tangential displacement, as shown in position IV. If the numerical implementation treated the contact forces as functions of only the relative displacements between nearest neighbors (with respect to the undeformed lattice), then there would be a non-zero shear contact force in position IV, which is non-physical: the tangential displacement should have been reset when contact was re-initiated. As another example, consider a scenario where the spheres in position I simply underwent a large rigid body rotation, as shown in position V. Then, the orientation of the contact plane would change significantly. However, in the numerical implementation mentioned above, the action of the contact forces would be orthogonal to (for normal contact forces), or within (for shear contact forces) the *original* contact plane, whose orientation now deviates from the true contact plane by large angles. These simple thought experiments illustrate that the contact forces generally depend on the entire *contact history*, rather than on the current state only. In addition, effects causing hysteresis, such as microslip and plasticity, may depend on the entire contact history (even without particle separation or large rotations), though we do not consider them here.

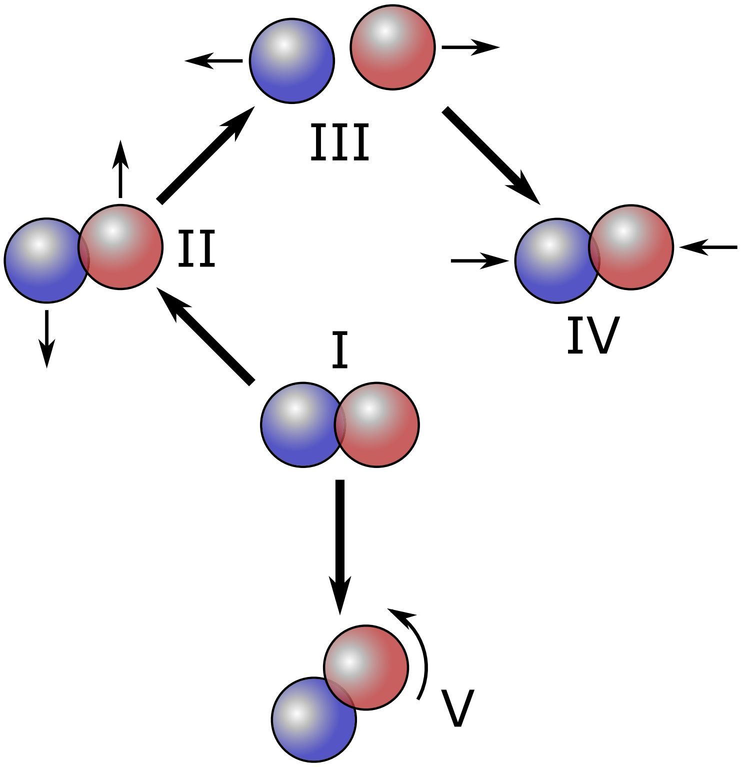

Figure 7.1: Illustration of loss and subsequent re-initiation of contact between two spheres.

7.3 Numerical Setup

The simulation domain for the results of this chapter is a 2D, HCP multilayer with one free and three fixed boundaries, as shown in Fig. 7.2. The domain has 51 rows of 101 spheres. The silica microspheres have diameter $D = 1$ μm, Young's Modulus $E = 73$ GPa, Poisson's ratio $\nu = 0.17$, and mass density $\rho = 2.0$ g/cm^3. We model an impulsive point source as an initial velocity imparted to the middle sphere of the top row.

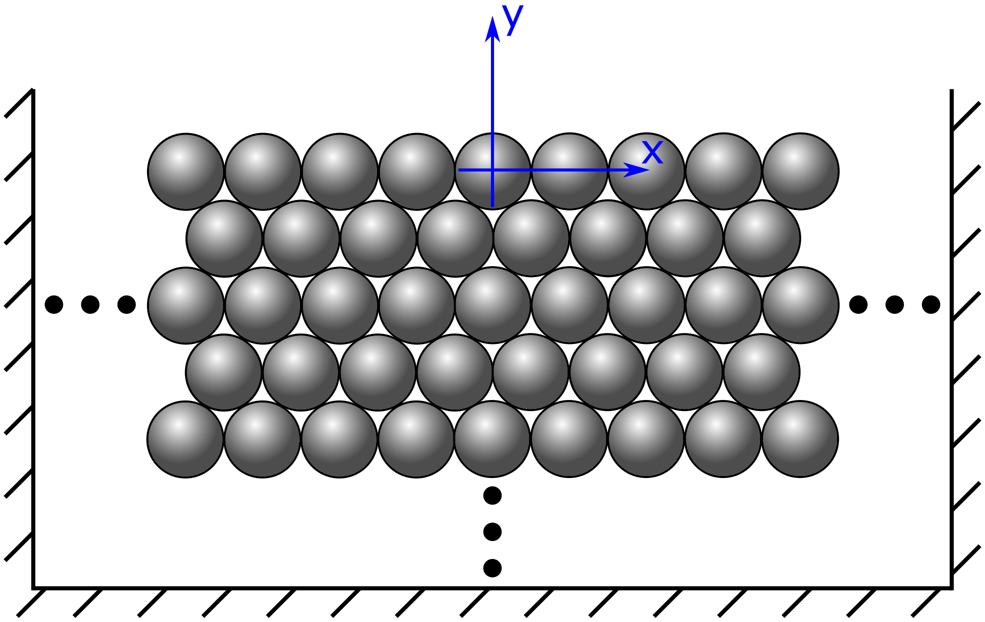

Figure 7.2: Schematic of the simulation setup for a 2D, HCP multilayer of microspheres.

We transform the cartesian velocity components v_x and v_y from the simulation output into polar form, with the origin placed at the site of the excited sphere, as shown below in Fig. 7.3. We define the longitudinal velocity v_L as the radial component, and the transverse velocity v_T as the tangential component. Also, we define the rotational velocity $v_R = R\omega_z$, where ω_z is the angular velocity of the sphere from the simulation output. This velocity is the tangential velocity of a point on the surface of the sphere, in the xy plane, and has the same scaling as the tangential velocity in terms of the relative motion of contacting sphere surfaces; thus, it holds greater physical relevance than the angular velocity ω_z itself. The transformation from the simulation output velocities to the quantities used here is given by

$$\begin{pmatrix} v_L \\ v_T \\ v_R \end{pmatrix} = \begin{pmatrix} \sin(\theta) & -\cos(\theta) & 0 \\ \cos(\theta) & \sin(\theta) & 0 \\ 0 & 0 & R \end{pmatrix} \begin{pmatrix} v_x \\ v_y \\ \omega_z \end{pmatrix}. \tag{7.1}$$

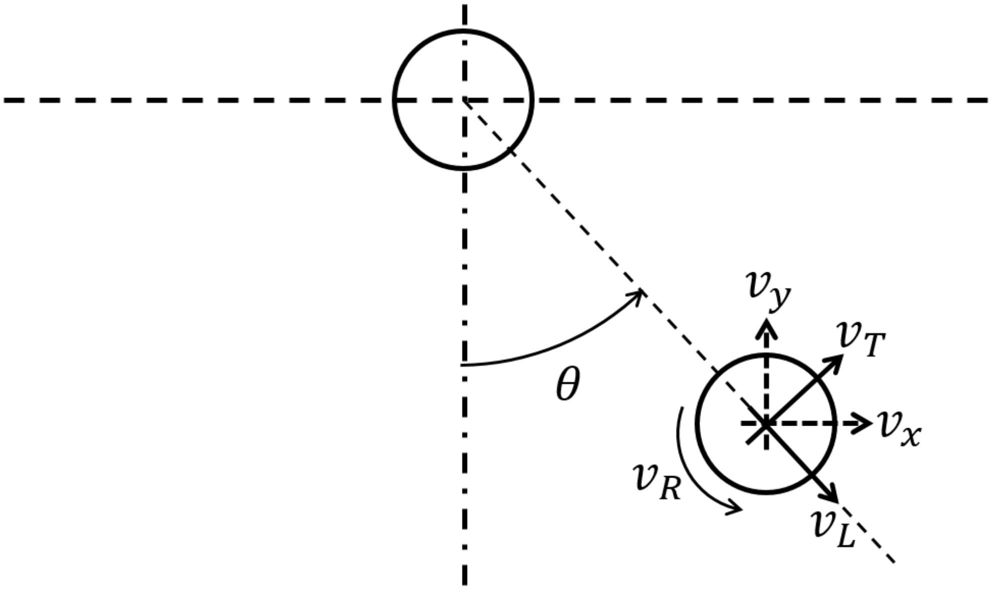

Figure 7.3: Diagram depicting the transformation from cartesian velocity components (simulation output) to longitudinal, transverse, and rotational velocity components.

7.4 Results and Discussion

The results presented here were obtained from simulations with a time step of 1.4 ps. This time step satisfies the convergence criterion[1]

$$\max\left(|E_n - T_0|/T_0\right) < 1e^{-5},$$

---

[1] See Appendix B for an explanation of this convergence criterion.

where E_n is the total energy at the n^{th} time step and $T_0 = (1/2)mv_0^2$ is the kinetic energy of the excited sphere at the initial time step. That is, the largest variation in total energy over all time steps should be greater than five orders of magnitude less than the energy input by the excitation.

7.4.1 Spatial Distribution of Kinetic Energy

We observe qualitative differences in the distribution of kinetic energy for different excitation amplitudes. We normalize each part of the kinetic energy by the input kinetic energy T_0, such that the normalized longitudinal, transverse, and rotational parts are defined as $\tilde{T}_L = (1/2)mv_L^2/T_0$, $\tilde{T}_T = (1/2)mv_T^2/T_0$, and $\tilde{T}_R = (1/2)(I/m)v_R^2/T_0$, respectively. The spatial distribution of normalized kinetic energy after 50 ns of simulation time (just before the fastest-moving waves first reach the lower boundary) is shown below for the initial velocities $v_{0,\ low} = 0.355$ m/s and $v_{0,\ high} = 10\ v_{0,\ low}$ in Fig. 7.4 and Fig. 7.5, respectively. Since the excitation and domain are symmetric about the line $X = 0$, only the right half of the domain is shown.

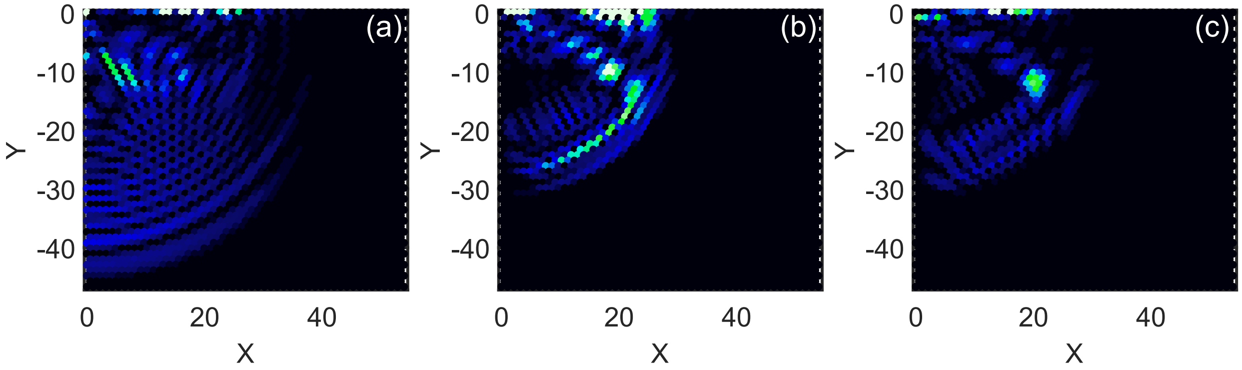

Figure 7.4: Spatial distributions of normalized kinetic energy for the case $v_0 = 1$. Panels (a), (b), and (c) correspond to longitudinal, transverse, and rotational parts of the kinetic energy.

In the distributions of longitudinal kinetic energy, shown in panels (a) of Fig. 7.4 and Fig. 7.5, we observe a longitudinal wave front that travels primarily downward in the low

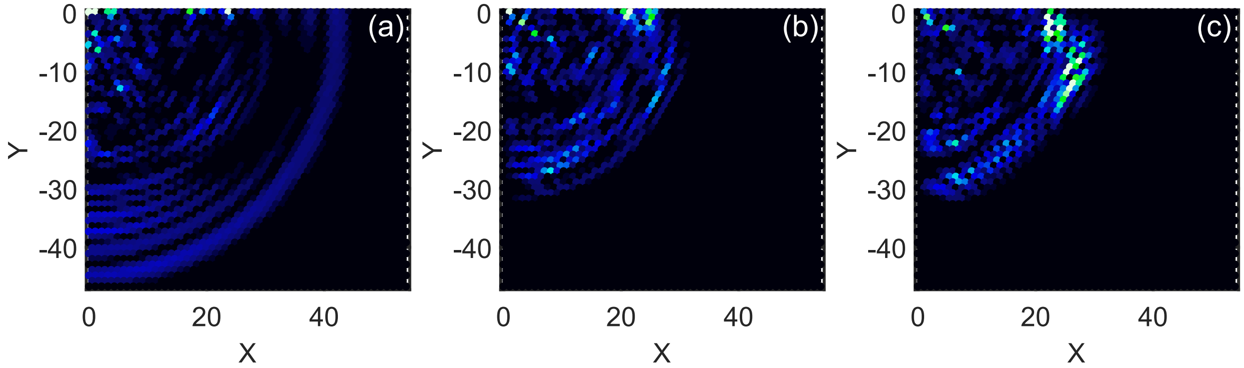

Figure 7.5: Spatial distributions of normalized kinetic energy for the case $v_0 = 10$. Panels (a), (b), and (c) correspond to longitudinal, transverse, and rotational parts of the kinetic energy.

amplitude case, but extends upward to the surface in the high amplitude case. The front also travels slightly faster in the high amplitude case, which is in agreement with established theory of granular crystals [4, 5]. For the transverse kinetic energy, as shown in panels (b), the low amplitude case shows a strong concentration along the lattice symmetry direction 30^o below the surface, and also in surface-localized waves. These regions are less prevalent in the high amplitude case, where the surface waves show less transverse kinetic energy, and the concentrated region along the 30^o symmetry direction has disappeared. Finally, the rotational parts of the kinetic energy, shown in panels (c) of Fig. 7.4 and Fig. 7.5, exist in the same general region as the transverse parts, but the amplitude dependence is different: in the high amplitude case, there is more rotational kinetic energy near the surface, and also along the 30^o symmetry direction. While it is known that the transverse and rotational motions are coupled along the symmetry directions (and decoupled from the longitudinal motion) [34], nonlinear effects that may govern energy transfer between these motions have been much less explored.

7.4.2 Amplitude Dependence of Propagation and Particle Velocity

To obtain more detailed information about the amplitude dependence, we probe the maximum particle velocity and the arrival time of the first peak at two sites: the *vertical* site (sphere on the line $X = 0$, at the 30^{th} layer from the free surface), and the *surface* site (sphere in the surface layer, at the 15^{th} site from from the point source). Due to symmetry, in the *vertical* case, only the longitudinal velocity will be non-zero. Sample time histories of the velocities at these two sites, for the case $v_0 = v_{0,\ high}$, are shown in Fig. 7.6 and Fig. 7.7 for the vertical and surface sites, respectively. We vary the initial velocity of the source sphere from $0.2v_{low}$ to $12v_{low}$, in increments of $0.2v_{low}$. The normalized maximum particle velocities and peak arrival times are shown for the vertical and surface sites in Fig. 7.8 and Fig. 7.9, respectively.

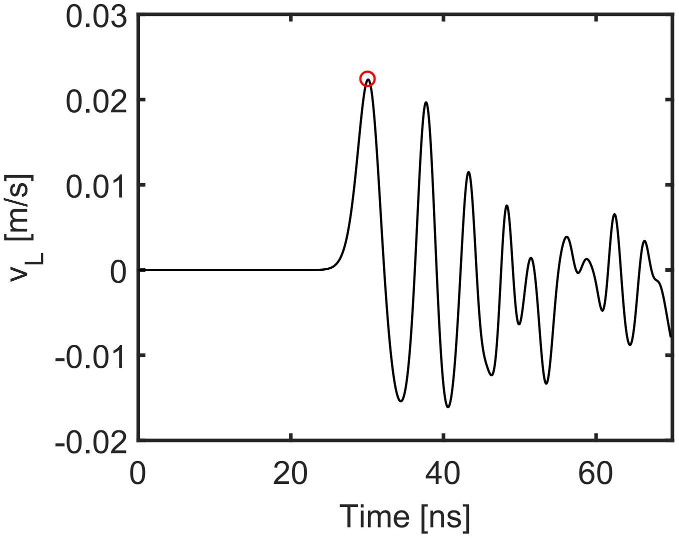

Figure 7.6: Time history of the longitudinal velocity of the sphere along the line $X = 0$, at the 30^{th} layer. The red circle indicates the first local maximum.

At the vertical site, we find an increasing peak particle velocity and decreasing arrival time with increasing source amplitude. This agrees qualitatively with established theory of 1D, precompressed GCs [4, 5]. We note that along this line, the velocity decays as the wave propagates, because the energy is radiating outward, in a manner similar to Ref. [25].

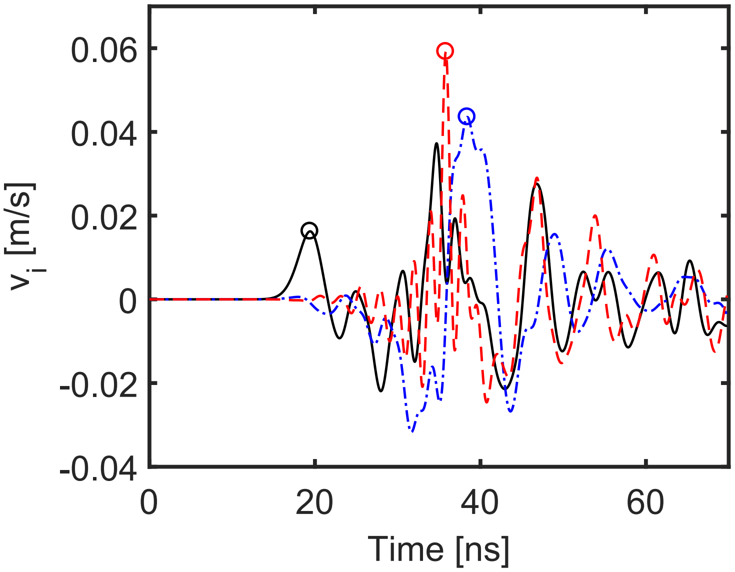

Figure 7.7: Time history of the longitudinal (black solid curves), transverse (blue dash-dotted curves), and rotational (red dashed curves) velocities of the sphere in the surface layer, at the 15^{th} sphere from the point source. The circle markers of corresponding colors indicate the first local maximum (longitudinal velocity) and global maxima (transverse and rotational velocities).

However, while the uncompressed GC of Ref. [25] would have vanishing sound speed at infinite distance from the source, the sound speed in our precompressed GC approaches the linear sound speed instead.

At the surface site, we observe an increase in the maximum longitudinal velocity with increasing source amplitude, while the maximum transverse and rotational velocities decrease initially, and then undergo rapid fluctuations, as shown in Fig. 7.9(a). The peak arrival time is shown in Fig. 7.9(b) for the longitudinal velocity only, because it has a distinct first local maximum, while the transverse and rotational velocity histories travel as wave packets, with no unique peaks to compare across many amplitudes. The longitudinal peak arrival time first increases with source amplitude, then levels off and eventually begins to decrease. The qualitatively different characteristics of the three velocity components are not unexpected, as multiple linear SAW modes have been shown to exist in GCs with square packing [32] and in Cosserat media [176, 177], in contrast to classical Rayleigh waves in a linear elastic, isotropic solid, for which only one mode exists [93]. It is intuitive that different linear modes could depend differently on amplitude in the nonlinear regime. Theories of nonlinear SAWs in isotropic and anisotropic elastic solids have existed for some time, but they typically describe either non-dispersive media or media with dispersion induced by an adhered layer [184, 185, 186], and do not consider particle rotations. An erratic amplitude dependence of the maximum particle velocities, though most obvious for the transverse and rotational components in Fig. 7.9(a), can be seen for all components, and at both sites, for source amplitudes above 1 m/s. Specifically, noticeable fluctuations can be seen near $v_0 \approx 1$ m/s and $v_0 \approx 3$ m/s in Fig. 7.8(a) and in both panels of Fig. 7.9. We speculate that these fluctuations are caused by broken contacts, which create defects in the lattice, and happen with greater frequency at higher amplitudes.

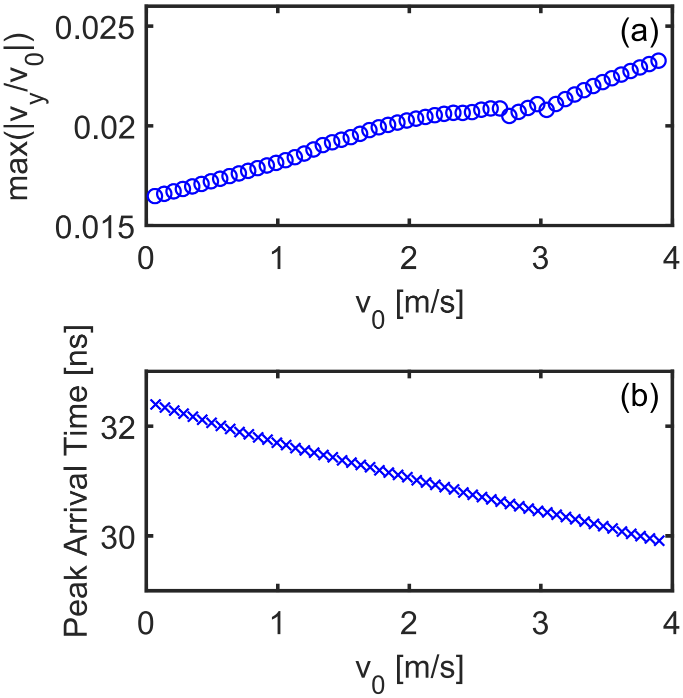

Figure 7.8: Amplitude dependence of (a) maximum particle velocity and (b) first peak arrival time for longitudinal waves along the vertical line below the excited sphere, at the 30^{th} layer.

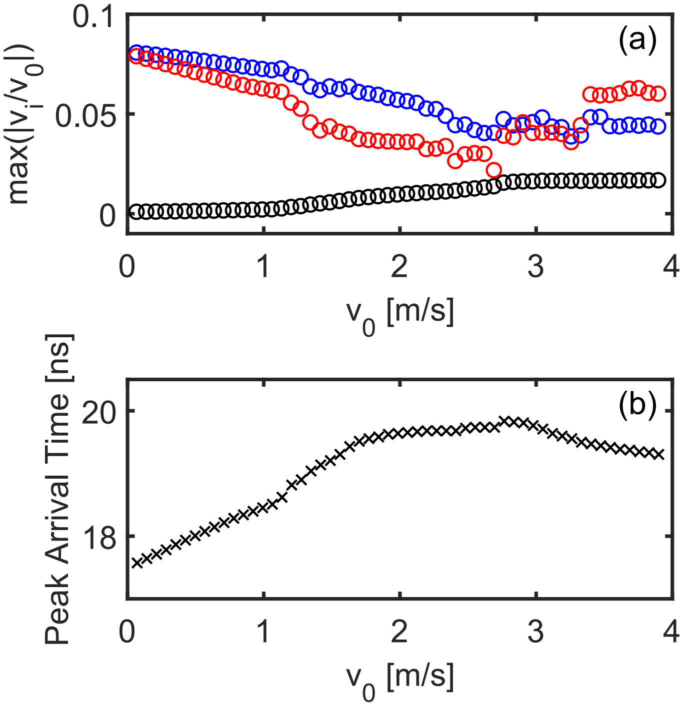

Figure 7.9: (a) Amplitude dependence of maximum particle velocity at the surface layer, at the 15^{th} sphere. Black, blue, and red circles correspond to longitudinal, transverse, and rotational velocities. (b) Amplitude dependence of first peak arrival time for longitudinal velocity, for the same sphere as (a).

7.5 Conclusion

In this chapter, we used multibody dynamics simulations to investigate amplitude dependence of wave propagation in a 2D, HCP multilayer of microspheres subjected to an impulsive point load. Varying the source amplitude over two orders of magnitude, we observed drastic qualitative changes in the spatial distribution of kinetic energy, as well as the partition of energy into longitudinal, transverse, and rotational motions. We found that the amplitude dependences of maximum particle velocity and arrival time for bulk longitudinal waves agree qualitatively with existing theory for precompressed GCs, while the results for surface waves could only be compared loosely to applicable linear theories. Finally, we observed an erratic amplitude dependence for the higher source amplitudes, which we attribute to broken contacts. In future studies, a more detailed analysis of the broken contacts, as well as a more careful comparison between this system and past works (for example, varying the strength of adhesion and the shear stiffness slowly from zero to the theoretical value), would be highly insightful. It would also be useful to develop theories for nonlinear, dispersive surface waves in GCs, where the dispersion is induced by structural periodicity and particle rotation. This work opens the door for future investigations of wave propagation in 3D microscale granular media. We expect this work to be applicable to future experiments on microscale GC multilayers, particularly those including localized sources and surface waves.

BIBLIOGRAPHY

[1] J. Duran, *Sand, powders, and grains: an introduction to the physics of granular materials*, (Springer-Verlag, New York, 2000).

[2] H. Hinrichsen and D. E. Wolf, *The Physics of Granular Media* (WILEY-VCH Verlag GmbH & Co. KGaA, Weinheim, 2004).

[3] J. Israelachvili, *Intermolecular and Surface Forces* (Elsevier, Inc., Burlington, MA, 2011).

[4] V. F. Nesterenko, *Dynamics of Heterogeneous Materials* (Springer-Verlag, New York, 2001).

[5] G. Theocharis, N. Boechler, and C. Daraio, Nonlinear Periodic Phononic Structures and Granular Crystals, *Acoustic Metamaterials and Phononic Crystals* (Springer Berlin Heidelberg, 2013), pp. 217-251.

[6] J. Sun, C.-J. Tang, P. Zhan, Z.-L. Han, Z.-S. Cao, and Z.-L. Wang, *Langmuir* **26**, 7859 (2010);

[7] V. Canalejas-Tejero, M. Ibisate, D. Golmayo, A. Blanco, and C. López, *Langmuir* **28**, 161 (2012).

[8] N. Boechler, J. Eliason, A. Kumar, A. A. Maznev, K. A. Nelson, and N. Fang, *Phys. Rev. Lett.* **111**, 036103 (2013).

[9] A. Vega-Flick, J. K. Eliason, A. A. Maznev, A. Khanolkar, M. Abi Ghanem, N. Boechler, J. J. Alvarado-Gil, and K. A. Nelson, *Rev. Sci. Instrum.* **86**, 123101 (2015).

[10] J. A. Rogers, A. A. Maznev, M. J. Banet, and K. A. Nelson, *Annu. Rev. Mater. Sci.* **30**, 117-157 (2000).

[11] H. Hertz, *J. Reine Angew. Math.* **92**, 156 (1882).

[12] R. D. Mindlin, *J. Appl. Mech.* **16** 3 (1949).

[13] K. L. Johnson, *Contact Mechanics* (Cambridge University Press, Cambridge, 1985).

[14] N. Boechler, G. Theocharis, and C. Daraio, *Nat. Mater.* **10**, 9 (2011).

[15] A. Spadoni and C. Daraio, *Proc. Natl. Acad. Sci. USA* **107**, 7230 (2010).

[16] J. Yang and C. Daraio, *Nonlinear Acoustic Metamaterials for Sound Attenuation Applications*, Darpa Report, Accession Number: ADA539264 (2011).

[17] L. Brillouin, *Wave propagation in periodic structures*, (Dover, New York, 1953).

[18] J. Ford, *Phys. Rep.* **213**, 271-310 (1992).

[19] M. J. Ablowitz and P. A. Clarkson, *Solitons, Nonlinear Evolution Equations and Inverse Scattering* (Cambridge University Press, Cambridge, 1991).

[20] J. M. English and R. L. Pego, *Proc. Am. Math. Soc.* **133**, 1763 (2005).

[21] A. Stefanov and P. G. Kevrekidis, *J. Nonlinear Sci.* **22**, 327 (2012).

[22] A. P. Awasthi, K. J. Smith, and P. H. Geubelle, *Mech. Mater.* **54**, 100-112 (2012).

[23] M. Manjunath, A. P. Awasthi, and P. H. Geubelle, *Granul. Matter* **16**, 141-150 (2014).

[24] A. Leonard and C. Daraio, *Phys. Rev. Lett.* **108**, 214301 (2012).

[25] A. Leonard, C. Chong, P. G. Kevrekidis, and C. Daraio, *Granul. Matter* **16** (4), 531-542 (2014).

[26] B. Gilles and C. Coste, *Phys. Rev. Lett.* **90**, 174302 (2003)

[27] A. Merkel, V. Tournat, and V. Gusev, *Phys. Rev. Lett.* **107**, 225502 (2011).

[28] V. Tournat, I. Pèrez-Arjona, A. Merkel, V. Sanchez-Morchillo, and V. Gusev, *New J. Phys.* **13**, 073042 (2011);

[29] H. Pichard, A. Duclos, J-P. Groby, and V. Tournat, *Phys. Rev. B* **86**, 134307 (2012).

[30] A. Merkel, V. Tournat, and V. Gusev, *Phys. Rev. E* **82**, 031305 (2010).

[31] L. Zheng, H. Pichard, V. Tournat, G. Theocharis, and V. Gusev, *Ultrasonics* **69**, 201-214 (2016).

[32] H. Pichard, A. Duclos, J.-P. Groby, V. Tournat, L. Zheng, and V. E. Gusev, *Phys. Rev. E* **93**, 023008 (2016).

[33] L. Zheng, V. Tournat, and V. Gusev, *Extreme Mech. Lett.* **(In Press)**, (2016).

[34] A. S. J. Suiker, A. V. Metrikine, and R. de Borst, *Int. J. Solids Struct.* **38** (9), 1563-1583 (2001).

[35] C. Cattaneo, *Rend. Accad. Naz. Lincei* **27**, 342 (1938).

[36] L. M. Schwartz, D. L. Johnson, and S. Feng, *Phys. Rev. Lett.* **52**, 831 (1984).

[37] F. Allein, V. Tournat, V. E. Gusev, and G. Theocharis, *Appl. Phys. Lett.* **108**, 161903 (2016).

[38] F. Allein, V. Tournat, V. E. Gusev, and G. Theocharis, *Extreme Mech. Lett.* **Accepted**, Available at http://dx.doi.org/10.1016/j.eml.2016.08.001 (2016).

[39] G. A. Maugin and A. V. Metrikine, *Mechanics of Generalized Continua: 100 Years After the Cosserats* (Springer, New York, 2010).

[40] E. Cosserat and F. Cosserat, *Théorie des corps déformables*, (Hermann, Paris, 1909). Reprint, Gabay, Paris, 2008.

[41] R. S. Lakes, *J. Mech. Mater. Struct.* **11**, 3 (2016).

[42] A. Merkel and S. Luding, *Int. J. Solids Struct.* **106**, 91-105 (2017).

[43] T. Kraus, D. Brodoceanu, N. Pazos-Perez, and A. Fery, Adv. Funct. Mater., **23**, 4529 (2013).

[44] O. D. Velev and S. Gupta, Advanced Mater., **21**, 1897 (2009).

[45] F. Li, D. P. Josephson, and A. Stein, Angew. Chem. Int. Ed. **50**, 360 (2011).

[46] N. Vogel, M. Retsch, C. A. Fustin, A. del Campo, and U. Jonas, Chem. Rev., **115**, 6265 (2015).

[47] V. M. Muller, B. V. Derjaguin, and Y. P. Toporov, *Colloids and Surfaces* **7**, 251-259 (1983).

[48] M. D. Pashley, *Colloids and Surfaces* **12**, 69-77 (1984).

[49] K. L. Johnson, K. Kendall, and A. D. Roberts, *Proc. R. Soc.* **324**, 301 (1971).

[50] D. Maugis, *J. Colloid Interface Sci.* **150**, 243 (1992).

[51] D. Tabor, *J. Colloid Interface Sci.* **58**, 2 (1977).

[52] D. Maugis and H. M. Pollock, *Acta Metall.* **32**, 1323 (1984).

[53] L. Kogut and I. Etsion, *Tribology T.* **46**, 383 (2008).

[54] C. Thornton and Z. Ning, *Powder Technol.* **99**, 154 (1998).

[55] A. Khanolkar, S. Wallen, M. Abi Ghanem, J. Jenks, N. Vogel, and N. Boechler, *Appl. Phys. Lett.* **107**, 071903 (2015);

[56] M. Hiraiwa, M. Abi Ghanem, S. P. Wallen, A. Khanolkar, A. A. Maznev, and N. Boechler, *Phys. Rev. Lett.* **116**, 198001 (2016).

[57] J. K. Eliason, A. Vega-Flick, M. Hiraiwa, A. Khanolkar, T. Gan, N. Boechler, N. Fang, K. A. Nelson, and A. A. Maznev, *Appl. Phys. Lett.* **108**, 061907 (2016).

[58] C. B. Scruby and L. E. Drain, *Laser Ultrasonics: Techniques and Applications*, (Taylor & Francis, New York, 1990).

[59] C. Glorieux, J. D. Beers, E. H. Bentefour, K. Van de Rostyne, and K. A. Nelson, *Rev. Sci. Instrum.* **75**, 2906 (2004).

[60] M. I. Hussein, M. J. Leamy, and M. Ruzzene, *Appl. Mech. Rev.* **66**, 040802-1 (2014).

[61] F. Lemoult, N. Kaina, M. Fink, and G. Lerosey, Nature Phys. **9**, 55 (2012).

[62] Y. Lai, Y. Wu, P. Sheng, Z. Q. Zhang, Nature Mater. **10**, 620 (2011).

[63] Z. Y. Liu, X. X. Zhang, Y. W. Mao, Y. Y. Zhu, Z. Y. Yang, C. T. Chan, and P. Sheng, Science **289**, 1734 (2000).

[64] N. Fang, D. J. Xi, J. Y. Xu, M. Ambati, W. Srituravanich, C. Sun, and X. Zhang, Nature Mater. **5**, 452 (2006).

[65] S. Zhang, L. L. Yin, and N. Fang, Phys. Rev. Lett. **102**, 194301 (2009).

[66] J. Mei, G. Ma, M. Yang, Z. Yang, W. Wen, and P. Sheng, Nature Commun. **3** 756 (2012).

[67] S. Zhang, C. G. Xia, and N. Fang, Phys. Rev. Lett. **106**, 024301 (2011).

[68] Related phenomena are also observed when the metamaterial unit cell is of suprawavelength dimension [69].

[69] M. Rupin, F. Lemoult, G. Lerosey, and P. Roux, Phys. Rev. Lett. **112**, 234301 (2014).

[70] J. H. Lee, C. Y. Koh, J. P. Singer, S. J Jeon, M. Maldovan, O. Stein, and E. L. Thomas, Adv. Mater. **26**, 532 (2014).

[71] W. Cheng, J. J. Wang, U. Jonas, G. Fytas, and N. Stefanou, Nature Mater **5**, 830 (2006).

[72] J. F. Galisteo-López, M. Ibisate, R. Sapienza, L. S. Froufe-Pérez, Álvaro Blanco, and Cefe López, Adv. Mater. **23**, 30 (2011).

[73] G. von Freymann, V. Kitaev, B. V. Lotsch, G. A. Ozin, Chem. Soc. Rev. **42**, 2528 (2013).

[74] B. Sepúlveda, P. C. Angelome, L. M., Lechuga, and L. M. Liz-Marzán, Nano Today **4**, 244 (2009).

[75] M. Grzelczak, J. Vermant, E. M. Furst, and L. M. Liz-Marzan, ACS Nano. **4**, 3591 (2010).

[76] A. Klinkova, R. M. Choueiri, E. Kumacheva, Chem. Soc. Rev. **43**, 3976 (2014).

[77] W. L. Min, B. Jiang, and P. Jiang, Adv. Mater. **20**, 3914 (2008).

[78] T. Still, W. Cheng, M. Retsch, R. Sainidou, J. Wang, U. Jonas, N. Stefanou, and G. Fytas, Phys. Rev. Lett. **100**, 194301 (2008).

[79] M. Caleap, and B. Drinkwater, Proc. Natl. Acad. Sci. U. S. A. **111**, 6226 (2014).

[80] T. Brunet, A. Merlin, B. Mascaro, K. Zimny, J. Leng, O. Poncelet, C. Aristégui, and O. Mondain-Monval., Nature Mater. **14**, 384 (2014).

[81] P. J. Beltramo, D. Schneider, G. Fytas, and E. M. Furst, Phys. Rev. Lett. **113**, 205503 (2014).

[82] H. Lamb, Proc. Roy. Soc. London, Ser. A **93**, 114 (1917).

[83] T. T Wu, J. C Hsu, and J. H. Sun, IEEE Trans. Ultrason. Ferroelectr. Freq. Control, **58**, 2146 (2011).

[84] V. Yantchev, and I. Katardjiev, J. Micromech. Microeng., **23**, 043001 (2013).

[85] J. Cuffe, O. Ristow, E. Chávez, A. Shchepetov, P. O. Chapuis, F. Alzina, M. Hettich, M. Prunilla, J. Ahopelto, T. Dekorsy, and C. M. Sotomayor Torres, Phys. Rev. Lett. **110**, 095503 (2013).

[86] Y. Pennec, B. Djafari-Rouhani, H. Larabi, J. O. Vasseur, and A. C. Hladky-Hennion, Phys. Rev. B., **78**, 104105 (2008).

[87] B. L. Davis, and M. I. Hussein, Phys. Rev. Lett. **112**, 055505 (2014).

[88] V. E. Gusev, O. B. Wright, New J. Phys. **16**, 123053 (2014).

[89] T. C. Wu, T. T. Wu, and J. C. Hsu, Phys. Rev. B. **79**, 104306 (2009).

[90] M. Oudich, M. Senesi, M. Badreddine Assouar, M. Ruzenne, J. H. Sun, B. Vincent, Z. Hou, and T. T. Wu, Phys. Rev. B, **84**, 165136 (2011).

[91] R. Zhu, X. N. Liu, G. K. Hu, C. T. Sun, and G. L. Huang, Nature Commun., **5**, 5510 (2014).

[92] B. Bonello, R. Marchal, R. Moiseyenko, Y. Pennec, B. Djafari-Rouhani, J. Zhao, and O. Boyko, Proc. ASME 2014 International Mechanical Engineering Congress and Exposition, Montreal, Quebec, Canada, 2014, pp. V013T16A019.

[93] W. M. Ewing, W. S. Jardetzky, and F. Press, *Elastic Waves in Layered Media* (McGraw-Hill Book Company, Inc., New York, 1957).

[94] S. P. Wallen, J. Lee, D. Mei, C. Chong, P. G. Kevrekidis, and N. Boechler, *Phys. Rev. E***95**, 022904 (2017).

[95] L. Solymar and E. Shamonina, *Waves in Metamaterials* (Oxford University Press, New York, 2009).

[96] H. Huang, C. Sun, and G. Huang, *Int. J. Eng. Sci.* **47**, 4 (2009).

[97] M. Lapine, I.V. Shadrivov, and Y.S. Kivshar, *Rev. Mod. Phys.* **86**, (2014).

[98] S. Sen, J. Hong, J. Bang, E. Avalos, and R. Doney, *Phys. Rep.* **462**, 21 (2008).

[99] P.G. Kevrekidis, *IMA J. Appl. Math.* **76**, 389 (2011).

[100] L. Bonanomi, G. Theocharis, and C. Daraio, *Phys. Rev. E* **91**, 033208 (2015).

[101] H. Xu, P. G. Kevrekidis, and A. Stefanov, *J. Phys. A: Math. Theor.* **48** (2015).

[102] E. Kim, F. Li, C. Chong, G. Theocharis, J. Yang, and P.G. Kevrekidis, *Phys. Rev. Lett.* **114**, 118002 (2015)

[103] P.G. Kevrekidis, A. Vainchtein, M. Serra Garcia, and C. Daraio, *Phys. Rev. E* **87**, 042911 (2013).

[104] J. Lydon, M. Serra-Garcia, and C. Daraio, *Phys. Rev. Lett.* **113**, 185503 (2014).

[105] L. Liu, G. James, P. G. Kevrekidis, and A. Vainchtein, *Under Review*, available at arXiv:1506.02827 (2015).

[106] L. Liu, G. James, P. Kevrekidis and A. Vainchtein, *Under Review*, available at arXiv:1603.06033 (2016).

[107] B. S. Lazarov and J. S. Jensen, *Int. J. Nonlinear Mech.* **42**, (2007).

[108] A. F. Vakakis, M. E. King, and A. J. Pearlstein, *Int. J. Nonlinear Mech.* **29**, 3 (1994).

[109] A. F. Vakakis, L. I. Manevitch, O. Gendelman, and L. Bergman, *J. Vib. Acoust* **123**, 3 (2001).

[110] S. Aubry, *Physica D* **103**, 201 (1997).

[111] S. Flach and C.R. Willis, *Phys. Rep.* **295**, 181 (1998).

[112] D. K. Campbell, S. Flach, and Y. S. Kivshar, *Physics Today* **57**, 1 (2004).

[113] S. Flach and A.V. Gorbach, Phys. Rep. **467**, 1 (2008).

[114] G. Theocharis, N. Boechler, P. G. Kevrekidis, S. Job, M. A. Porter, and C. Daraio, *Phys. Rev. E* **82**, 056604 (2010).

[115] Y. Starosvetsky, M. A. Hasan, A. F. Vakakis, and L. I. Manevitch, *SIAM J. Appl. Math* **72**, 1 (2012).

[116] N. Boechler, G. Theocharis, S. Job, P. G. Kevrekidis, M. A. Porter, and C. Daraio, *Phys. Rev. Lett.* **104**, 244302 (2010).

[117] C. Chong, F. Li, J. Yang, M. O. Williams, I. G. Kevrekidis, P. G. Kevrekidis, and C. Daraio, *Phys. Rev. E* **89**, 032924 (2014).

[118] M. A. Hasan, S. Cho, K. Remick, A. F. Vakakis, D. M. McFarland, and W. M. Kriven, *Granul. Matter* **17**, 1 (2015).

[119] N. Lazarides, M. Eleftheriou, and G. Tsironis, *Phys. Rev. Lett.* **97**, 157406 (2006).

[120] M. Eleftheriou, N. Lazarides, G. P. Tsironis, and Yu. S. Kivshar, *Phys. Rev. E* **80**, 017601 (2009).

[121] N. Lazarides and G. P. Tsironis, *Phys. Rev. Lett.* **110**, 053901 (2013).

[122] M. Syafwan, H. Susanto, and S. M. Cox, Phys. Rev. E **81**, 026207 (2010).

[123] M. D. Murthy Peri and C. Cetinkaya, *J. Colloid Interface Sci.* **288**, 432 (2005).

[124] Y. Sato and T. Usami, *Geophys. Mag.* **31**, 15 (1962).

[125] A. R. Baghai-Wadji, V. P. Plessky, and A. W. Simonian, *Akust. Zh.* **38**, 806-821 (1992).

[126] E. A. Garova, A. A. Maradudin, and A. P. Mayer, *Phys. Rev. B* **59**, 13291 (1999).

[127] R.S. MacKay and S. Aubry, *Nonlinearity* **7**, 1623 (1994).

[128] M. J. Ablowitz, *Nonlinear Dispersive Waves Asymptotic Analysis and Solitons* (Cambridge University Press, Cambridge, 2011).

[129] G. Kerschen, M. Peeters, J. C. Golinval, and A. F.Vakakis, *Mech. Syst. Signal Pr.* **23**, 1 (2009).

[130] M. Peeters, R. Vigui, G. Srandour, G.Kerschen, and J. C.Golinval, *Mech. Syst. Signal Pr.* **23**, 1 (2009).

[131] P.G. Kevrekidis, J. Cuevas-Maraver, and D. Pelinovsky, arXiv:1604.06956.

[132] A. Couairon and A. Mysyrowicz, *Phys. Rep.* **441**, 47 (2007).

[133] A. Rosas, A. H. Romero, V. F. Nesterenko, and Katja Lindenberg, *Phys. Rev. Lett.* **98**,164301 (2007).

[134] E. B. Herbold and V. F. Nesterenko, *Phys. Rev. E* **75**, 021304 (2007).

[135] R. Vacher, J. Pelous, F. Plicque, and A. Zarembowitch, *J. Non-Cryst. Solids* **45**, (1981).

[136] G. K. Batcher, *An Introduction to Fluid Dynamics* (Cambridge University Press, Cambridge, 2000).

[137] S. P. Wallen, A. A. Maznev, and N. Boechler, *Phys. Rev. B* **92**, 174303 (2015).

[138] L. Bonanomi, G. Theocharis, and C. Daraio, *Phys. Rev. E* **91**, 033208 (2015).

[139] A. N. Lazaridi and V. F. Nesterenko, *Prikl. Mekh. Tekh. Fiz.* **26**, 115 (1985); C. Coste, E. Falcon, and S. Fauve, *Phys. Rev. E* **56**, 6104 (1997); S. Job, F. Melo, A. Sokolow, and S. Sen, *Phys. Rev. Lett.* **94**, 178002 (2005); C. Daraio, V. F. Nesterenko, E. B. Herbold, S. Jin, *Phys. Rev. E* **73**, 026610 (2006);

[140] N. Boechler and C. Daraio, in *Proceedings of the ASME 2009 Design Engineering Technical Conferences, San Diego, 2009*, pp. 271-276;

[141] N. Boechler, G. Theocharis, S. Job, P.G. Kevrekidis, M.A. Porter, and C. Daraio, *Phys. Rev. Lett.* **104**, 244302 (2010);

[142] N. Boechler, J. Yang, G. Theocharis, P. G. Kevrekidis, and C. Daraio, *J. Appl. Phys.* **109**, 074906 (2011).

[143] H. P. Rossmanith and A. Shukla, *Acta Mech.* **42**, 221 (1982).

[144] C. Daraio, D. Ngo, V. F. Nesterenko, and F. Fraternali, *Phys. Rev. E* **82**, 036603 (2010).

[145] J. Yang, S. Dunatunga, C. Daraio, *Acta Mech.* **223**, 549 (2012).

[146] B. Gilles and C. Coste, *Phys. Rev. Lett.* **90**, 174302 (2003).

[147] A. Leonard, F. Fraternali, and C. Daraio, *Exp. Mech.* **53**, 327 (2011).

[148] Y. A. Kosevich and E. S. Syrkin, Phys. Lett. A **135**, 298 (1989).

[149] B. Bhushan, *Handbook of Micro/Nano Tribology*, (CRC Press, Boca Raton, FL, 1999).

[150] R. Fuchs, T. Weinhart, J. Meyer, H. Zhuang, T. Staedler, X. Jiang, and S. Luding, *Granular matter* **16**, 3 (2014).

[151] The quantity c_N is the long-wavelength longitudinal acoustic velocity in a suspended monolayer (or a 3D simple cubic lattice of spheres). The quantity c_S is the corresponding transverse velocity for the model case when rotations are disallowed. In a cubic crystal, in contrast to an isotropic solid, there are no restrictions on the ratio of transverse-to-longitudinal velocities in the [100] direction. While c_N and c_S can take any values if G_N and G_S are varied arbitrarily, within the Hertz-Mindlin theory c_S is just slightly below c_N.

[152] C. Dominik and A. G. G. M. Tielens, *Phil. Mag. A*, **72**, 783 (1995).

[153] M. D. Murthy Peri, C. Cetinkaya, *J. Colloid and Interface Sci.* **288**, 432 (2005).

[154] N. P. Bansat and R. H. Doremus, *Handbook of Glass Properties* (Academic Press, Orlando, FL, 1986).

[155] J. von Neumann and E. Wigner, "On the behavior of eigenvalues in adiabatic processes," *Phys. Z* **30**, 467 (1929).

[156] Y. Guillet, B. Audoin, M. Ferrie, and S. Ravaine, Phys. Rev. B **86**, 035456 (2012).

[157] S. Wallen, C. Chong, P. G. Kevrekidis, and N. Boechler, in *Proc. International Symposium on Optomechatronic Technologies, Seattle, 2014*, pp. 15-17.

[158] A. Vega-Flick, R. Duncan, S. P. Wallen, N. Boechler, C. Stelling, M. Retsch, J. J. Alvarado-Gil, K. A. Nelson, and A. A. Maznev, *"Vibrational dynamics of a two-dimensional micro-granular crystal studied with laser-induced transient gratings"*, **under review**, (2017).

[159] A. Vega-Flick, R. Duncan, S. P. Wallen, N. Boechler, C. Stelling, M. Retsch, J. J. Alvarado-Gil, K. A. Nelson, and A. A. Maznev, *"Contact-based and spheroidal dynamics of a hexagonally arranged monolayer of microspheres on a substrate"*, in preparation (preprint available at arXiv:1703.04784), (2017).

[160] G. Huang and B. Hu, *Phys. Rev. B* **57**, 5746 (1998).

[161] A. V. Gorbach and M. Johansson, *Phys. Rev. E* **67**, 066608 (2003).

[162] G. James, P. G. Kevrekidis, and J. Cuevas, *Physica D* **251**, 39 (2013).

[163] G. Huang, Z. Shi, and Z. Xu, *Phys. Rev. B* **47**, 14561 (1993).

[164] S. P. Wallen and N. Boechler, *Wave Motion* **68**, 22 (2016).

[165] M. Sadd, Q. Tai, and A. Shukla, *Int. J. Nonlinear Mech.* **28**, 2 (1993).

[166] R. W. Boyd, *Nonlinear Optics*, (Academic Press, 2003).

[167] M. F. Hamilton and D. T. Blackstock, *Nonlinear Acoustics*, (Acoustical Society of America, NY, 2008).

[168] J. Cabaret, V. Tournat, and P. Bequin, *Phys. Rev. E* **86**, 041305 (2012).

[169] V. J. Sànchez-Morcillo, I. Pèrez-Arjona, and V. Romèro-Garcia, V. Tournat, and V. E. Gusev, *Phys. Rev. E* **88**, 043203 (2013).

[170] O. Dazel and V. Tournat, *J. Acoust. Soc. Am.* **127**, 2 (2010).

[171] L. K. Zarembo and V. A. Krasilnikov, *Sov. Phys. Usp.* **13**, 778 (1971).

[172] V. Tournat, V. E. Gusev, V. Yu. Zaitsev, and B. Castagnede, *Europhys. Lett.* **66** (6), 798-804 (2004).

[173] A. Merkel, V. Tournat, and V.Gusev, *Phys. Rev. E* **90**, 023206 (2014).

[174] R. Ganesh and S. Gonella, *Phys. Rev. Lett.* **114**, 054302 (2015).

[175] J. Bunyan, A. F. Vakakis, and S. Tawfick, *Phys. Rev. E* **92**, 062206 (2015).

[176] M. Kulesh, *Bull. Seismol. Soc. Am.* **99**, 1416-1422 (2009)

[177] E. Grekova, M. Kulesh, and G. Herman, *Bull. Seismol. Soc. Am.* **99**, 1423-1428 (2009).

[178] V. E. Gusev, V. Aleshin, and V. Tournat, *Phys. Rev. Lett.* **96**, 214301 (2006).

[179] L. Bonneau, B. Andreotti, and E. Clément, *Phys. Rev. E* **75**, 016602 (2007).

[180] G. F. Miller and H. Pursey, *Proc. R. Soc.* **A233**, 55-69 (1955).

[181] A. Mourad and M. Deschamps, *J. Acoust. Soc. Am.* **97**, 3194-3197 (1995).

[182] A. G. Every, K. Y. Kim, and A. A. Maznev, *J. Acoust. Soc. Am.* **102**, 1346-1355 (1997).

[183] A. Tasora, R. Serban, H. Mazhar, A. Pazouki, D. Melanz, J. Fleischmann, M. Taylor, H. Sugiyama, and D. Negrut, in *High Performance Computing in Science and Engineering - Lecture Notes in Computer Science* (T. Kozubek, ed. Springer, 2016), pp. 19-49.

[184] A. P. Mayer, *Phys. Rep.* **256**, 237-366 (1995).

[185] A. P. Mayer, *Ultrasonics* **48**, 478-481 (2008).

[186] G. A. Maugin, *Mech. Res. Comm.* **38**, 341-349 2011.

[187] W. H. Press, S. A. Teukolsky, W. T. Vetterling, and B. P. Flannery, *Numerical Recipes in C++, Second Edition*, (Cambridge University Press, Cambridge, 2002).

Appendix A

ACKNOWLEDGMENTS FOR TECHNICAL CONTENT

Chapter 2: A Self-Assembled Metamaterial for Lamb Waves

S.P.W. greatly appreciates contributions from the coauthors of Ref. [55] (Amey Khanolkar, Maround Abi Ghanem, Jennifer Jenks, Nicolas Vogel, and Nicholas Boechler). The authors of Ref. [55] thank J. Eliason, A. Maznev, and K. Nelson for guidance with the optical setup and for useful discussions. This work was supported by NSF grant no. CMMI-1333858 and the University of Washington (UW) Royalty Research Foundation. Part of this work was conducted at the UW NanoTech User Facility and the Washington Nanofabrication Facility, members of the NSF National Nanotechnology Infrastructure Network.

Chapter 3: Discrete Breathers in a Mass-in-mass chain with Hertzian Local Resonators

S.P.W. greatly appreciates contributions from the coauthors of Ref. [94] (John Lee, Domonic Mei, Chris Chong, Panos G. Kevrekidis, and Nicholas Boechler), as well as useful discussions with Alexei A. Maznev. N.B. and S.P.W. acknowledge support from the National Science Foundation (grant no. CMMI-1333858) and the Army Research Office (grant no. W911NF-15-1-0030). P.G.K. acknowledges support from the Army Research Office (grant no. W911NF-15-1-0604) and the Air Force Office of Scientific Research (Grant No. FA9550-12-10332).

Chapter 4: Dynamics of a Monolayer of Microspheres on an Elastic Substrate

S.P.W. greatly appreciates contributions from the coauthors of Ref. [137] (Alexei A. Maznev and Nicholas Boechler), as well as useful discussions with Vitaly Gusev. S.P.W. and N.B. gratefully acknowledge support from the US National Science Foundation (grant no. CMMI-

1333858) and the US Army Research Office (grant no. W911NF-15-1-0030). The contribution by A.A.M. was supported by the National Science Foundation Grant No. CHE-1111557.

Chapter 5: Nonlinear Dynamics of a 1D Granular Crystal Adhered to a Substrate

S.P.W. and N.B. greatly appreciate useful discussions with Alexei Maznev and Georgios Theocharis, and gratefully acknowledge support from the US National Science Foundation (grant no. CMMI-1333858).

Chapter 6: Shear to Longitudinal Mode Conversion via Second Harmonic Generation in a 2D Microscale Granular Crystal

S.P.W. greatly appreciates contributions from the coauthor of Ref. [164] (Nicholas Boechler), as well as useful discussions with Alexei A. Maznev. S.P.W. and N.B. acknowledge support from the Army Research Office through grant no. W911NF-15-1-0030.

Chapter 7: Energy Partition in a 2D Microscale Granular Crystal Subject to an Impulsive Point Load: Multibody Dynamics Simulation

S.P.W. greatly appreciates assistance from Arman Pazouki, Michal Kwarta, and Dan Negrut, who implemented adhesive forces in the CHRONO simulation package, and also provided guidance in setting up and running the simulations. S.P.W. and N.B. acknowledge support from the Army Research Office through grant no. W911NF-15-1-0030.

Appendix B

COMPUTATIONAL METHODS

B.1 Solution of Ordinary Differential Equations

The numerical simulations of ordinary differential equations (ODEs) shown in Chapters 3, 5, and 6 were performed using a fourth-order accurate Runge-Kutta method [187]. The method was implemented in MATLAB. While MATLAB has a built-in integrator with the same accuracy (the *ode45()* function), direct control of the step size is not allowed; thus, we chose to use an in-house implementation.

B.1.1 Fourth-Order Explicit Runge-Kutta Method

Consider the system of first-order ODEs

$$\dot{\mathbf{y}} = \mathbf{f}(t, \mathbf{y}), \tag{B.1}$$

where $\mathbf{y}$ is a vector of states, t is the time, and $\mathbf{f}(t, \mathbf{y})$ is the time derivative of $\mathbf{y}$. For the systems simulated in this thesis, the equations of motion are second-order in time; thus, they must be converted into first-order form as

$$\mathbf{y} = \begin{pmatrix} \mathbf{x} \\ \mathbf{v} \end{pmatrix} \tag{B.2}$$

$$\dot{\mathbf{y}} = \begin{pmatrix} \mathbf{v} \\ \dot{\mathbf{v}} \end{pmatrix} \quad , \tag{B.3}$$

where $\mathbf{x}$ is a vector of positions and $\mathbf{v}$ is a vector containing the associated velocities. The accelerations $\dot{\mathbf{v}}$ are generally a sum of forces or moments on a body, and depend on the system.

For the numerical solution of Eq. (B.1), let the state vector at the i^{th} time step be denoted $\mathbf{y}_i$. The solution at the next time step $i+1$ is approximated as

$$\mathbf{y}_{i+1} = \mathbf{y}_i + h\tilde{\mathbf{f}}(t_i, \mathbf{y}_i), \tag{B.4}$$

where h is the step size and $\tilde{\mathbf{f}}(t_i, \mathbf{y}_i)$ is an approximation to the average derivative over the interval $[t_i, t_i + h]$.

The error of the scheme (for some h) is determined by the choice of $\tilde{\mathbf{f}}(t, \mathbf{y}_n)$. For the fourth-order Runge-Kutta method (RK4), this is given by

$$\begin{aligned}
\tilde{\mathbf{f}}(t, \mathbf{y}_n) &= \frac{h}{6}(\mathbf{k_1} + 2\mathbf{k_2} + 2\mathbf{k_3} + \mathbf{k_4}) + \mathcal{O}(h^5) \\
\mathbf{k_1} &= \mathbf{f}(t_n, \mathbf{y}_n) \\
\mathbf{k_2} &= \mathbf{f}(t_n + h/2, \mathbf{y}_n + h/2\mathbf{k_1}) \\
\mathbf{k_3} &= \mathbf{f}(t_n + h/2, \mathbf{y}_n + h/2\mathbf{k_2}) \\
\mathbf{k_4} &= \mathbf{f}(t_n + h, \mathbf{y}_n + h\mathbf{k_3}).
\end{aligned}$$

The local truncation error is proportional to h^5, and the global truncation error (accumulated over the entire solution interval) is proportional to h^4. We use an explicit scheme, i.e. the left-hand side of Eq. (B.4) is entirely known based on the state of the systems at the previous step. While the use of an implicit scheme would guarantee stability of the integrator, this would involve the solution of a system of nonlinear algrebraic equations (often involving hundreds of unknowns) at each time step, which would drastically increase computational costs.

B.1.2 Step Size Selection

To ensure that our numerical integrations have been carried out with acceptable accuracy, we choose step sizes sufficiently small for the following energy balance criterion to be satisfied:

$$\max\left(\left|\frac{1}{2}\left(\mathbf{m}\odot\mathbf{v}_i\right)\bullet\mathbf{v}_i-\sum_{0}^{i}\left[\left(\mathbf{m}\odot\dot{\mathbf{v}}_i\right)\bullet\Delta\mathbf{y}_i\right]\right|/E_0\right)<1e^{-5}, \tag{B.5}$$

where $\tilde{\mathbf{m}}$ is a vector containing the masses of the bodies with corresponding velocities $\tilde{\mathbf{v}}_\mathbf{i}$ (or moments of inertia for angular velocities), the symbol $\odot$ denotes element-wise multiplication, and E_0 is a reference value, which is usually taken to be the initial total energy of the system. In Eq. (B.5), the first term in the numerator on the left-hand side is the kinetic energy at step i, and the summation represents the total work done by all forces leading up to step i. Thus, the criterion states that the largest deviation of the total energy from the ideal balance must be at least five orders of magnitude smaller than the reference energy. While most conventional methods of step size selection involve some numerical estimate of the truncation error, either by using a higher-order step during the integration (e.g. for an adaptive step size) [187] or simply reducing the step size until the results converge, our method relies on direct observation of the simulated physics. Thus, by simply examining a plot of the kinetic energy and total work as function of time, we can easily (almost immediately, in most cases) discern issues with simulation time steps and errors in the code for the equations of motion.

The criterion of Eq. (B.5) can be evaluated using either of two methods. In the first method, the energy terms can be evaluated in post-processing, using the time history output from the simulation. This method requires that both the kinetic energy and total work be known in closed form, at any time step. While the calculation of the kinetic energy is trivial, the work term is usually known only for conservation systems, in which it is simply the potential energy. In the second method, the energy terms are evaluated during the integration itself; this allows the work term to be computed directly, using the accelerations $\dot{\mathbf{v}}_i$ and incremental displacements $\mathbf{y}_i$, at each time step. This method is valid for both conservative and nonconservative systems, but requires significant modifications to the integrator code.

B.2 Solution of Dispersion Equations

Dispersion equations having the form

$$\det\left(M(k,\omega)\right) = 0, \tag{B.6}$$

where M is a matrix whose elements are functions of the wave number k and frequency ω, can be solved using the built-in MATLAB function *fzero()*. This is accomplished by first choosing a fixed value of k, then using the *fzero()* function to solve for the corresponding value of ω. A complete curve can be computed by incrementally increasing the fixed value of k, using the previous solution as the initial guess in the *fzero()* function. To determine the first initial guess, it is often possible to find an analytical solution of Eq. (B.6) for some special cases (usually $k = 0$ or at the Brillouin edge). More generally, an initial guess can be made by plotting the contours[1] of $\det\left(M(k,\omega)\right)$ and choosing a (k,ω) pair close to a zero-contour[2].

It is possible for the left-hand side of Eq. (B.6) to be complex-valued. In this case, the equation can be solved by applying this procedure to the squared magnitude of the determinant, $|\det\left(M(k,\omega)\right)|^2$.

B.3 On the Use of Mathematica, etc. for Algebraic Manipulation

For the perturbation analysis in Chapter 6 and the derivation of the Nonlinear Schrodinger Equation in Chapter 5, the program *Mathematica* was used to manipulate the long equations. This was done because the perturbation expansions have many terms, and can be quite cumbersome to work with. Furthermore, if an error is made early on in a derivation, *Mathematica* can simply re-evaluate the script, whereas in a hand-written derivation, it would take hours to re-derive many pages of work.

Another situation that requires cumbersome algebra is the derivation of dispersion relations, when expanding determinants of the dispersion matrices. In this thesis, some of the dispersion

---

[1] This can be done using the built-in MATLAB *contour()*, for example.

[2] Alternatively, one can visualize the magnitude of $\det\left(M(k,\omega)\right)$ using a surface plot instead of locating a zero-contour.

matrices are as large as fifth-order (as in Chapters 2 and 4); thus, the expansion of these determinants, as was needed in Chapter 2 to obtain Eq. (2.6) from Eq. (2.5), can be quite time consuming. However, Eq. (2.6) was *not* derived using *Mathematica*; this is because the software, which is not programmed to recognize physically-relevant terms, expands the determinant without using sensible simplifications along the way. Using a hand-written derivation, the physically-relevant terms (such as the sub-determinants D_1 and D_2 in Eq. (2.6)) can be retained in the process, resulting in a much more elegant result than the *Mathematica* expansion.

Appendix C

DETAILS FOR CHAPTER 5: NONLINEAR DYNAMICS OF A 1D GRANULAR CRYSTAL ADHERED TO A SUBSTRATE

C.1 Dimensionless Equations of Motion

Substituting (5.1) - (5.2) and (5.6) - (5.8) into (5.3) - (5.5) and switching to the normalized variables, we find the dimensionless equations of motion

$$\begin{aligned}
\ddot{Q}_j = & - K_s(Q_j + \mu\Phi_j) + G_n(Q_{j+1} - 2Q_j + Q_{j-1}) \\
& + \frac{1}{4}G_n(Q_{j-1} - Q_{j+1})(Q_{j+1} - 2Q_j + Q_{j-1}) + \frac{1}{2}\delta_{ig}^2 K_s Z_j(Q_j + \mu\Phi_j) \\
& + \frac{1}{24}G_n\left[3Q_j(Q_{j+1}^2 + Q_{j-1}^2) - 3Q_j^2(Q_{j+1} + Q_{j-1}) - (Q_{j+1}^3 - 2Q_j^3 + Q_{j-1}^3)\right] \\
& + \frac{1}{8}\delta_{ig}^4 K_s Z_j^2(Q_j + \mu\Phi_j)
\end{aligned} \tag{C.1}$$

$$\begin{aligned}
\ddot{Z}_j = & - K_n Z_j + G_s[Z_{j+1} - 2Z_j + Z_{j-1} + \mu(\Phi_{j-1} - \Phi_{j+1})] \\
& + \frac{1}{4}K_n\delta_{ig}^2 Z_j^2 - \frac{1}{2}G_s\,[Q_{j+1}Z_{j+1} - Q_{j-1}Z_{j-1} - Z_j(Q_{j+1} - Q_{j-1}) - Q_j(Z_{j+1} - Z_{j-1}) \\
& - \mu(Q_{j+1}\Phi_{j+1} + Q_{j-1}\Phi_{j-1} + \Phi_j(Q_{j+1} + Q_{j-1}) - Q_j(\Phi_{j+1} + 2\Phi_j + \Phi_{j-1}))] \\
& + \frac{1}{24}\delta_{ig}^4 K_n Z_j^3 - \frac{1}{8}G_s\,[Q_{j+1}^2 Z_{j+1} + Q_{j-1}^2 Z_{j-1} - Z_j(Q_{j+1}^2 + Q_{j-1}^2) - 2Q_j(Q_{j+1}Z_{j+1} + Q_{j-1}Z_{j-1}) \\
& + 2Q_j Z_j(Q_{j+1} + Q_{j-1}) + Q_j^2(Z_{j+1} - 2Z_j + Z_{j-1}) \\
& - \mu(Q_{j+1}^2\Phi_{j+1} - Q_{j-1}^2\Phi_{j-1} + \Phi_j(Q_{j+1}^2 - Q_{j-1}^2) - 2Q_j(Q_{j+1}\Phi_{j+1} - Q_{j-1}\Phi_{j-1}) \\
& - 2Q_j\Phi_j(Q_{j+1} - Q_{j-1}) + Q_j^2(\Phi_{j+1} - \Phi_{j-1}))]
\end{aligned} \tag{C.2}$$

$$\begin{aligned}
\ddot{\Phi}_j = & - K_s(Q_j + \mu\Phi_j) + G_s(Z_{j+1} - Z_{j-1} - \mu(\Phi_{j+1} + 2\Phi_j + \Phi_{j-1})) \\
& + \frac{1}{2}\delta_{ig}^2 K_s Z_j(Q_j + \mu\Phi_j) - \frac{1}{2}G_s\,[Q_{j+1}Z_{j+1} + Q_{j-1}Z_{j-1} - Q_j(Z_{j+1} - 2Z_j + Z_{j-1}) - Z_j(Q_{j+1} + Q_{j-1}) \\
& - \mu(Q_{j+1}\Phi_{j+1} - Q_{j-1}\Phi_{j-1} + \Phi_j(Q_{j+1} - Q_{j-1}) - Q_j(\Phi_{j+1} - \Phi_{j-1}))] \\
& + \frac{1}{8}\delta_{ig}^4 K_s Z_j^2(Q_j + \mu\Phi_j) - \frac{1}{8}G_s\,[Q_{j+1}^2 Z_{j+1} - Q_{j-1}^2 Z_{j-1} - Z_j(Q_{j+1}^2 - Q_{j-1}^2) \\
& - 2Q_j(Q_{j+1}Z_{j+1} - Q_{j-1}Z_{j-1}) + 2Q_j Z_j(Q_{j+1} - Q_{j-1}) + Q_j^2(Z_{j+1} - Z_{j-1}) \\
& - \mu(Q_{j+1}^2\Phi_{j+1} + Q_{j-1}^2\Phi_{j-1} + \Phi_j(Q_{j+1}^2 + Q_{j-1}^2) - 2Q_j(Q_{j+1}\Phi_{j+1} + Q_{j-1}\Phi_{j-1}) \\
& - 2Q_j\Phi_j(Q_{j+1} + Q_{j-1}) + Q_j^2(\Phi_{j+1} + 2\Phi_j + \Phi_{j-1}))]\,,
\end{aligned} \tag{C.3}$$

where the normalized stiffnesses are $K_n = 1$, $K_s = (2/3)B^g/A^g$, $G_n = \delta_{ig}A^i/A^g$, and $G_s = (2/3)\delta_{ig}B^i/A^g$, $\mu = mR^2/I$, and the double dot notation $\ddot{(\cdot)}$ is the second derivative in the normalized time, τ. The inertia ratio μ is a parameter that defines the coupling between translation and rotation: in the limit $\mu \to 0$ (corresponding to infinitely large rotational inertia), the rotational terms in Eqs. (C.1) - (C.2) vanish, and Eq. C.3 governs infinitessimal rotations that are essentially decoupled from translation.

C.2 Solvability Conditions for the NLS Derivation

C.2.1 Solution at $\mathcal{O}(\varepsilon^1)$

From the coefficients of εSE, we find

$$\begin{pmatrix} -\omega^2 + \beta_1 - 2\gamma_1(\varphi_1 - 1) & 0 & \mu\beta_1 \\ 0 & -\omega^2 + \alpha_1 - 2\eta_1(\varphi_1 - 1) & 2\mathrm{i}\mu\eta_1\psi_1 \\ \beta_1 & -2\mathrm{i}\eta_1\psi_1 & -\omega^2 + \mu\beta_1 + 2\mu\eta_1(\varphi_1 + 1) \end{pmatrix} \begin{pmatrix} a_1 \\ b_1 \\ c_1 \end{pmatrix} = \begin{pmatrix} 0 \\ 0 \\ 0 \end{pmatrix}. \tag{C.4}$$

The coefficient matrix on the left-hand side is the dispersion matrix M_1. From this, we recover the dispersion relation $\det(M_1(k, \omega)) = 0$, and the constants a_1, b_1, c_1 can be calculated for a particular pair (k, ω). Since the dispersion relation has three modes, for a single wave number k, we can find a different set of constants for each mode (and hence a different NLS equation).

C.2.2 Solution at $\mathcal{O}(\varepsilon^2)$

From the coefficients of $\varepsilon^2 S^2 E^2$, we find

$$\begin{pmatrix} -4\omega^2+\beta_1-2\gamma_1(\varphi_2-1) & 0 & \mu\beta_1 \\ 0 & -4\omega^2+\alpha_1-2\eta_1(\varphi_2-1) & 2\mathrm{i}\mu\eta_1\psi_2 \\ \beta_1 & -2\mathrm{i}\eta_1\psi_2 & -4\omega^2+\mu\beta_1+2\mu\eta_1(\varphi_2+1) \end{pmatrix} \begin{pmatrix} a_2 \\ b_2 \\ c_2 \end{pmatrix}$$

$$= -\begin{pmatrix} \delta_{ig}^2 b_1(a_1+\mu c_1)\beta_2 - 4\mathrm{i}a_1^2\gamma_2(\varphi_1-1)\psi_1 \\ \delta_{ig}^2 b_1^2\alpha_2 + 2a_1\eta_2(\mu c_1(\varphi_2-1)+\mathrm{i}b_1(2\psi_1-\psi_2)) \\ \delta_{ig}^2 b_1(a_1+\mu c_1)\beta_2 + 2a_1\eta_2(b_1(2\varphi_1-\varphi_2-1)+\mathrm{i}\mu c_1\psi_2) \end{pmatrix}. \tag{C.5}$$

From the coefficients of $\varepsilon^2 S_X E$, we find

$$\left(M_1, 2\mathrm{i}\omega\begin{pmatrix} a_1 \\ b_1 \\ c_1 \end{pmatrix}\right)\begin{pmatrix} a_5 \\ b_5 \\ c_5 \\ v \end{pmatrix} = 2D\begin{pmatrix} \mathrm{i}\gamma_1\psi_1 & 0 & 0 \\ 0 & \mathrm{i}\eta_1\psi_1 & -\mu\eta_1\varphi_1 \\ 0 & \eta_1\varphi_1 & -\mathrm{i}\mu\eta_1\psi_1 \end{pmatrix}\begin{pmatrix} a_1 \\ b_1 \\ c_1 \end{pmatrix}. \tag{C.6}$$

From the coefficients of $\varepsilon^2 S\bar{S}$, we find

$$\begin{pmatrix} \beta_1 & 0 & \mu\beta_1 \\ 0 & \alpha_1 & 0 \\ \beta_1 & 0 & \mu(\beta_1+4\eta_1) \end{pmatrix}\begin{pmatrix} a_3 \\ b_3 \\ c_3 \end{pmatrix} = -\begin{pmatrix} \delta_{ig}^2\bar{b}_1(a_1+\mu c_1)\beta_2 + c.c. \\ 2\delta_{ig}^2|b_1|^2\alpha_2 \\ \delta_{ig}^2\bar{b}_1(a_1+\mu c_1)\beta_2 + 4\eta_2(\bar{b}_1 a_1(\varphi_1-1)+\mathrm{i}\mu\bar{c}_1 a_1\psi_1) + c.c. \end{pmatrix}. \tag{C.7}$$

C.2.3 Solution at $\mathcal{O}(\varepsilon^3)$

From the coefficients of $\varepsilon^3 S^3 E^3$, we find

$$\begin{pmatrix} -9\omega^2 + \beta_1 - 2\gamma_1(\varphi_3 - 1) & 0 & \mu\beta_1 \\ 0 & -9\omega^2 + \alpha_1 - 2\eta_1(\varphi_3 - 1) & 2\mathrm{i}\mu\eta_1\psi_3 \\ \beta_1 & -2\mathrm{i}\eta_1\psi_3 & -9\omega^2 + \mu\beta_1 + 2\mu\eta_1(\varphi_3 + 1) \end{pmatrix} \begin{pmatrix} a_4 \\ b_4 \\ c_4 \end{pmatrix}$$

$$= - \begin{pmatrix} \delta_{ig}^2\beta_2[b_2(a_1 + \mu c_1) + b_1(a_2 + \mu c_2)] + \delta_{ig}^4\beta_3 b_1^2(a_1 + \mu c_1) \\ \qquad - 4\mathrm{i}\gamma_2 a_1 a_2[(\varphi_2 - 1)\psi_1 + (\varphi_1 - 1)\psi_2] - 2\gamma^3 a_1^3[3\varphi_1 - 3\varphi_2 + \varphi_3 - 1] \\ 2\delta_{ig}^2\alpha_2 b_1 b_2 + \delta_{ig}^4\alpha_3 b_1^3 + 2\eta_2[a_2(\mu c_1(-\varphi_1 + \varphi_2 + \varphi_3 - 1) + \mathrm{i}b_1(\psi_1 + \psi_2 - \psi_3)) \\ \qquad + a_1(\mu c_2(\varphi_1 - \varphi_2 + \varphi_3 - 1) + \mathrm{i}b_2(\psi_1 + \psi_2 - \psi_3))] \\ \qquad + 2\eta_3 a_1^2[-b_1(3\varphi_1 - 3\varphi_2 + \varphi_3 - 1) - \mathrm{i}\mu c_1(\psi_1 + \psi_2 - \psi_3)] \\ \delta_{ig}^2\beta_2[b_2(a_1 + \mu c_1) + b_1(a_2 + \mu c_2)] + \delta_{ig}^4\beta_3 b_1^2(a_1 + \mu c_1) \\ \qquad + 2\eta_2[a_2(b_1(\varphi_1 + \varphi_2 - \varphi_3 - 1) - \mathrm{i}\mu c_1(\psi_1 - \psi_2 - \psi_3)) \\ \qquad + a_1(b_2(\varphi_1 + \varphi_2 - \varphi_3 - 1) + \mathrm{i}\mu c_2(\psi_1 - \psi_2 + \psi_3))] \\ \qquad - 2\eta_3 a_1^2[\mu c_1(\varphi_1 + \varphi_2 - \varphi_3 - 1) + \mathrm{i}b_1(3\psi_1 - 3\psi_2 + \psi_3)] \end{pmatrix} . \tag{C.8}$$

From the coefficients of $\varepsilon^3 S S_X E^2$, we find

$$\begin{pmatrix} -4\omega^2+\beta_1-2\gamma_1(\varphi_2-1) & 0 & \mu\beta_1 \\ 0 & -4\omega^2+\alpha_1-2\eta_1(\varphi_2-1) & 2\mathrm{i}\mu\eta_1\psi_2 \\ \beta_1 & -2\mathrm{i}\eta_1\psi_2 & -4\omega^2+\mu\beta_1+2\mu\eta_1(\varphi_2+1) \end{pmatrix}\begin{pmatrix} a_6 \\ b_6 \\ c_6 \end{pmatrix}$$

$$= 4\begin{pmatrix} -2\mathrm{i}v\omega+\mathrm{i}D\gamma_1\psi_2 & 0 & 0 \\ 0 & -2\mathrm{i}v\omega+\mathrm{i}D\eta_1\psi_2 & -\mu D\eta_1\varphi_2 \\ 0 & D\eta_1\varphi_2 & -2\mathrm{i}v\omega-\mathrm{i}\mu D\eta_1\psi_2 \end{pmatrix}\begin{pmatrix} a_2 \\ b_2 \\ c_2 \end{pmatrix}$$
$$+\begin{pmatrix} -\delta_{ig}^2\beta_2[a_5b_1+a_1b_5+\mu(b_5c_1+b_1c_5)] \\ \qquad -4\gamma_2a_1[-2\mathrm{i}a_5(\varphi_1-1)\psi_1+Da_1(\varphi_1-\varphi_1^2+\psi_1^2)] \\ -2\delta_{ig}^2\alpha_2b_1b_5+\eta_2[a_1(4Db_1(-\varphi_1+\varphi_2)-2\mathrm{i}b_5(2\psi_1-\psi_2))-2\mathrm{i}a_5b_1(2\psi_1-\psi_2) \\ \qquad +\mu(-2a_5c_1(\varphi_2-1)+2a_1(-c_5(\varphi_2-1)-2\mathrm{i}Dc_1\psi_2))] \\ -\delta_{ig}^2\beta_2[a_5b_1+a_1b_5+\mu(b_5c_1+b_1c_5)]+\eta_2[2a_5b_1(-2\varphi_1+\varphi_2+1) \\ \qquad +2a_1(b_5(-2\varphi_1+\varphi_2+1)-2\mathrm{i}Db_1(\psi_1-\psi_2))-2\mathrm{i}\mu(a_5c_1\psi_2+a_1(-2\mathrm{i}Dc_1\varphi_2+c_5\psi_2))] \end{pmatrix}. \tag{C.9}$$

From the coefficients of $\varepsilon^3 S\bar{S}_X$, we find

$$\begin{pmatrix} \beta_1/2 & 0 & \mu\beta_1/2 \\ 0 & \alpha_1/2 & 0 \\ \beta_1/2 & 0 & \mu(\beta_1/2+2\eta_1) \end{pmatrix}\begin{pmatrix} a_7 \\ b_7 \\ c_7 \end{pmatrix}$$

$$= -\begin{pmatrix} \delta_{ig}^2\beta_2[b_1(\bar{a}_5+\mu\bar{c}_5)+\bar{b}_5(a_1+\mu c_1)]+4D\gamma_2|a_1|^2(\varphi_1-1) \\ 2\delta_{ig}^2\alpha_2\bar{b}_5b_1+(D/2)\eta_1\mu(c_3+\bar{c}_3)+2D\eta_2[\bar{b}_1a_1(\varphi_1-1)+\mathrm{i}\mu\bar{c}_1a_1\psi_1+\bar{a}_1(b_1(\varphi_1-1)-\mathrm{i}\mu c_1\psi_1)] \\ \delta_{ig}^2\beta_2[b_1(\bar{a}_5+\mu\bar{c}_5)+\bar{b}_5(a_1+\mu c_1)]-(D/2)\eta_1(b_3+\bar{b}_3)+2\eta_2[2\bar{a}_5b_1(\varphi_1-1)+2a_1\bar{b}_5(\varphi_1-1) \\ \qquad +D\mu\bar{a}_1c_1(\varphi_1+1)-D\mu a_1\bar{c}_1(\varphi_1-1)-\mathrm{i}D(a_1\bar{b}_1+\bar{a}_1b_1)\psi_1+2\mathrm{i}\mu(a_1\bar{c}_5-\bar{a}_5c_1)\psi_1] \end{pmatrix}. \tag{C.10}$$

Three NLS equations are found from the terms proportional to $\varepsilon^3 S_T$, $\varepsilon^3 S_{XX}$, and $\varepsilon^3|S|^2S$ as

$$\left[M_1\begin{pmatrix}a_8\\ b_8\\ c_8\end{pmatrix}-\vec{y}_8\right]S_T+\left[M_1\begin{pmatrix}a_9\\ b_9\\ c_9\end{pmatrix}-\vec{y}_9\right]S_{XX}+\left[M_1\begin{pmatrix}a_{10}\\ b_{10}\\ c_{10}\end{pmatrix}-\vec{y}_{10}\right]|S|^2S=0. \tag{C.11}$$

The vectors $\vec{y}_8$, $\vec{y}_9$, and $\vec{y}_{10}$ are given by

$$\vec{y}_8 = 2\mathrm{i}\omega\begin{pmatrix}a_1\\ b_1\\ c_1\end{pmatrix} \tag{C.12}$$

$$\begin{aligned}\vec{y}_9 = {}&\begin{pmatrix}-v^2+D^2\gamma_1\varphi_1 & 0 & 0\\ 0 & -v^2+D^2\eta_1\varphi_1 & -\mathrm{i}D^2\mu\eta_1\psi_1\\ 0 & \mathrm{i}D^2\eta_1\psi_1 & -v^2-D^2\mu\eta_1\varphi_1\end{pmatrix}\begin{pmatrix}a_1\\ b_1\\ c_1\end{pmatrix}\\ &+\begin{pmatrix}2\mathrm{i}(-v\omega+D\gamma_1\psi_1) & 0 & 0\\ 0 & 2\mathrm{i}(-v\omega+D\eta_1\psi_1) & -2D\mu\eta_1\varphi_1\\ 0 & 2D\eta_1\varphi_1 & -2\mathrm{i}(v\omega+D\mu\eta_1\psi_1)\end{pmatrix}\begin{pmatrix}a_5\\ b_5\\ c_5\end{pmatrix}\end{aligned} \tag{C.13}$$

$$\vec{y}_{10} = \left(\begin{array}{l} \delta_{ig}^2\beta_2[\,-\bar{b}_1(a_2+\mu c_2) - b_1(a_3+\mu c_3) - b_2(\bar{a}_1+\mu\bar{c}_1) - b_3(a_1+\mu c_1)] \\ \qquad -\,\delta_{ig}^4\beta_3 b_1[2\bar{b}_1(a_1+\mu c_1) + b_1(\bar{a}_1+\mu\bar{c}_1)] - 4\mathrm{i}\gamma_2\bar{a}_1 a_2[(\varphi_2-1)\psi_1 - (\varphi_1-1)\psi_2] \\ \qquad -\,6|a_1|^2 a_1\gamma_3(-4\varphi_1+\varphi_2+3) \\ -2\delta_{ig}^2\alpha_2(\bar{b}_1 b_2 + b_1 b_3) - 3\delta_{ig}^4\alpha_3|b_1|^2 b_1 \\ \qquad +\,\eta_2[-4\mu a_1 c_3(\varphi_1-1) + 2\mu\bar{a}_1 c_2(-2\varphi_1+\varphi_2+1) \\ \qquad +\,a_2(-2\mu\bar{c}_1(\varphi_2-1) + 2\mathrm{i}\bar{b}_1(2\psi_1-\psi_2)) + 2\mathrm{i}\bar{a}_1 b_2(2\psi_1-\psi_2)] \\ \qquad +\,2\eta_3 a_1[(\bar{b}_1 a_1 + 2\bar{a}_1 b_1)(4\varphi_1-\varphi_2-3) + \mathrm{i}\mu(a_1\bar{c}_1 - 2\bar{a}_1 c_1)(2\psi_1-\psi_2)] \\ \delta_{ig}^2\beta_2[\,-\bar{b}_1(a_2+\mu c_2) - b_1(a_3+\mu c_3) - b_2(\bar{a}_1+\mu\bar{c}_1) - b_3(a_1+\mu c_1)] \\ \qquad -\,\delta_{ig}^4\beta_3 b_1[2\bar{b}_1(a_1+\mu c_1) + b_1(\bar{a}_1+\mu\bar{c}_1)] \\ \qquad +\,\eta_2[-2\bar{a}_1 b_2(\varphi_2-1) - 4\mathrm{i}\mu a_1 c_3\psi_1 + 2\mathrm{i}\mu\bar{a}_1 c_2\psi_2 + a_2(-2\bar{b}_1(\varphi_2-1) - 2\mathrm{i}\mu\bar{c}_1(2\psi_1+\psi_2))] \\ \qquad +\,2\eta_3 a_1[-\mu(a_1\bar{c}_1 - 2\bar{a}_1 c_1)(\varphi_2-1) + \mathrm{i}(a_1\bar{b}_1 + 2\bar{a}_1 b_1)(2\psi_1-\psi_2)] \end{array} \right), \tag{C.14}$$

where we have used the fact that a_3, b_3, and c_3 are real (due to the fact that the matrix and right-hand side of Eq. (C.7) are real). Since we are modeling the modulation of a single carrier wave, these three NLS equations should be equivalent. Therefore, the unknown coefficients of Eq. (C.11) must be chosen to be of the form

$$\mathrm{i}\lambda_8\begin{pmatrix}1\\1\\1\end{pmatrix}S_T + \lambda_9\begin{pmatrix}1\\1\\1\end{pmatrix}S_{XX} + \lambda_{10}\begin{pmatrix}1\\1\\1\end{pmatrix}|S|^2S = 0. \tag{C.15}$$

This is accomplished by solving the appended systems

$$\left[M_1, -\mathrm{i}\begin{pmatrix}1\\1\\1\end{pmatrix}\right]\begin{pmatrix}a_8\\b_8\\c_8\\\lambda_8\end{pmatrix} = \vec{y}_8 \tag{C.16}$$

$$\left[M_1, -\begin{pmatrix}1\\1\\1\end{pmatrix}\right]\begin{pmatrix}a_9\\b_9\\c_9\\\lambda_9\end{pmatrix} = \vec{y}_9 \tag{C.17}$$

$$\left[M_1, -\begin{pmatrix}1\\1\\1\end{pmatrix}\right]\begin{pmatrix}a_{10}\\b_{10}\\c_{10}\\\lambda_{10}\end{pmatrix} = \vec{y}_{10}. \tag{C.18}$$

Finally, we arrive at a single NLS equation to describe the modulation of the envelope:

$$\mathrm{i}\lambda_8 S_T + \lambda_9 S_{XX} + \lambda_{10}|S|^2 S = 0, \tag{C.19}$$

where λ_8, λ_9, and λ_{10} are functions of wave number and frequency, and are generally complex.